Interferometric Beam Size Monitor for BESSY II

MASTER THESIS

in fulfillment of the requirements for the degree Master of Science (M. Sc.) in Physics

Humboldt-Universität zu Berlin
Faculty of Mathematics and Natural Sciences
Department of Physics

submitted by:	Marten Koopmans
born:	5th February 1992 in Emden
reviewer:	Prof. Dr. Andreas Jankowiak
	Prof. Dr. Gregor Schiwietz
submitted:	30th November 2017
corrected version:	12th February 2018

The upgrade of the BESSY II storage ring to BESSY VSR demands additional beam diagnostics for machine commissioning, development and ensuring long term quality and stability of user operation. In particular bunch resolved diagnostics are required because of the complex fill pattern to serve different user requests at the same time. Presently, transverse beam size measurements are performed with X-ray pinhole monitor systems, which do not provide bunch resolved information. Alternative methods to measure the transverse beam size using synchrotron radiation in the visible spectrum are interferometric techniques, which can also be upgraded efficiently to bunch resolved systems. Therefore a double slit interferometer has been designed. The system has been successfully commissioned and the experimental results are discussed and compared with existing pinhole systems.

Das Upgrade des BESSY II Speicherrings zu BESSY VSR erfordert zusätzliche Strahldiagnose, um sowohl für Inbetriebnahme und Entwicklung der Maschine bereitzustehen, als auch die langfristige Qualität und Stabilität des Nutzerbetrieb zu sichern. Insbesondere werden wegen des komplexen Füllmusters, das verschiedene Nutzeranforderungen zur gleichen Zeit erfüllt, Bunch aufgelöste Diagnosesysteme benötigt. Zur Zeit wird die transversale Strahlgröße mit Lochkamera Monitoren gemessen, die mit Röntgenstrahlung arbeiten und keine Bunch aufgelösten Informationen liefern. Alternative Methoden, die transversale Strahlgröße zu messen und dabei Licht im sichbaren Bereich zu nutzen, sind interferometrische Systeme, welche effizient zu einem Bunch aufgelösten Systemen erweitert werden könnten. Zu diesem Zweck wurde ein Doppelspaltinterferometer entworfen. Das System wurde in Betrieb genommen und die experimentellen Ergebnisse werden diskutiert und mit den bestehenden Pinhole-Systemen verglichen.

Contents

1. Introduction

When charged particles are accelerated perpendicular to their direction of movement, electromagnetic radiation is emitted. If the particles move at relativistic speed, this radiation is called synchrotron radiation (SR) and is usually produced in magnetic fields. Synchrotron radiation has plenty of attractive properties, such as a broad spectrum and a high photon flux. Depending on the source the produced SR has a high brilliance and arbitrary polarisation properties can be achieved. Observed first at synchrotrons [1], SR became an important tool for several scientific fields, e. g. material science, chemistry and medicine. Therefore SR is produced at dedicated light sources for experiments in these fields.

First experiments used SR only parasitically at accelerators designed for high energy particle physics. Those are called first generation light sources. Second generation light sources are storage rings build for the purpose of generating SR. The first one of these was Tantalus I starting operation in 1968 [2]. With third generation light sources the further increasing demand of SR with a brilliance was accomplished and the key difference to second generation light sources is the incorporation of insertion devices (IDs).

In operation since 1998 BESSY II [3] is a classical third generation light source located in Berlin Adlershof from the Helmholtz-Zentrum Berlin (HZB). The electron storage ring operates at an energy of 1.7 GeV and is optimized for the generation of soft X-rays. There is also a dedicated short bunch optics to provide shorter pulses, but due to reduced photon flux it is only offered a few weeks per year [4].

Alongside free electron lasers (FELs) [5] which are available complementary with the third generation light sources, research and development is ongoing for energy recovery linacs (ERLs) [6]. The main trend for new and upgrade projects of existing synchrotron facilities is however, to achieve so called diffraction limited source sizes. With multi bend achromats the beam emittance is reduced to a level that even in the medium X-ray range the brilliance is diffraction limited. The first facility utilizing this scheme is MAX IV [7, 8] and many others are following.

For BESSY II an intermediate upgrade step was chosen. Since the interest in shorter pulses is also growing, it is planned to upgrade BESSY II to the variable pulse length storage ring BESSY VSR [3, 9, 10]. Diffraction limited sources cannot provide shorter pulses, since the bunch length has to be increased significantly. BESSY VSR tries to satisfy the already existing and growing user demand for intense short pulses, while still providing high average photon flux.

With regard to BESSY VSR it is necessary to upgrade the machine diagnostics. Because different bunch types in terms of current, bunch length and transverse beam size are stored simultaneously, bunch resolved diagnostics are needed for the commissioning and development of BESSY VSR. Moreover non-invasive diagnostic techniques ensure long term quality and stability of user operation [3].

One important property of the beam is the transverse source size. At BESSY II two pinhole systems are in operation to image the source point directly [11]. Because of the diffraction limit X-ray radiation at a photon energy of 16 keV is used. Different

source sizes for simultaneously stored bunches are already present at BESSY II and are also expected for BESSY VSR. In addition effects like single bunch instabilities, beam movements or coupled bunch instabilities can affect the transverse beam sizes of particular bunches. For BESSY VSR further techniques are required to obtain bunch resolved information. Especially systems using visible light are of interest, because they could be upgraded efficiently to a bunch resolved systems applying fast gating techniques. However light in the visible region cannot be used for direct imaging due to the higher diffraction limit and thus interferometric methods are required. One well understood and efficient method is the double slit interferometry, which can measure small transverse sizes down to a few µm [12].

This work shows the implementation of a double slit interferometer at BESSY II [13]. An overview of the BESSY II storage ring and the upgrade to BESSY VSR is given in Chapter 2. Next, the theory for interferometric beam size measurement and the principle of a double slit interferometer are explained in Chapter 3. Chapter 4 describes the preparatory work and the implementation of the double slit interferometer, including the setup, the software, consideration of parameter constraints and the error estimation. Finally results for various beam size measurements are shown in Chapter 5 and improvements, further applications and an estimation of the upgrade to a bunch resolved system are given in Chapter 6.

2. Storage Ring BESSY II

This chapter gives an overview of the BESSY II electron storage ring and its present operation. Subsequently the BESSY VSR project as the running upgrade project of BESSY II is introduced.

2.1. BESSY II

BESSY II [3, 14] is a third generation light source located in Berlin Adlershof operated by the Helmholtz-Zentrum Berlin (HZB). The main parameters of the storage ring are listed in Tab. 2.1 and a detailed drawing including the linac, the booster synchrotron and the beamlines is shown in Fig. 2.1.

Table 2.1.: Most important machine parameters from BESSY II standard user operation [3].

Parameter	**Value**
Energy E	1.7 GeV
Horizontal emittance ε_x	5 nm rad
$\varepsilon_y/\varepsilon_x$	≈2 %
Circumference	240 m
Harmonic number h	400
Revolution frequency f_{rev}	1.25 MHz
Bending radius ρ	4.35 m
Fundamental RF frequency f_{rf}	500 MHz
Fundamental RF sum voltage U_{rf}	1.5 MV
Max. beam current I	300 mA
Momentum compaction factor α_c, nominal	7.3×10^{-4}
Relative natural energy spread, rms δ	7×10^{-4}
Transverse tunes Q_{hor}, Q_{ver}	17.85, 6.74
Longitudinal tune Q_s, nominal	0.0064

The acceleration process begins in the gun of the linac, where the electrons are delivered by a DC grid cathode. Here the electrons reach an energy of 90 keV. In the linac the electron beam is focused and accelerated to an energy of 50 MeV. The beam is then guided through the injection line into the booster [16].

In the booster synchrotron the electrons are accelerated to the storage ring energy of 1.7 GeV. The magnets are wired in three independent resonant circuits for the bending, the horizontal focusing and the horizontal defocusing magnets, respectively. This enables a 10 Hz oscillation of the synchrotron and the electrons are accelerated from an energy of 50 MeV to an energy of 1.7 GeV. At 1.7 GeV the electron beams can then be extracted and guided through the transfer line into the storage ring [17, 18].

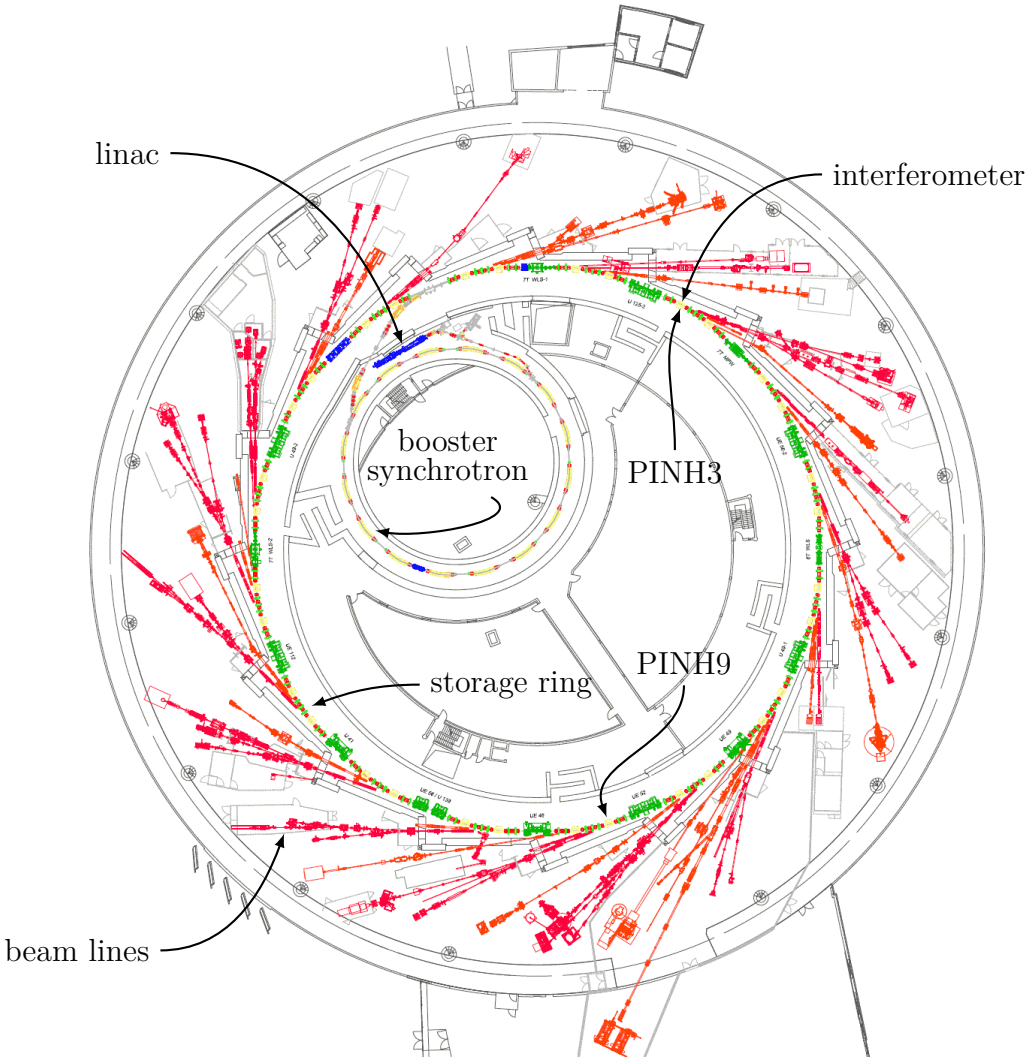

Figure 2.1.: Overview of the synchrotron light source BESSY II with linac, booster synchrotron, the electron storage ring and the beam lines (red) in the experimental hall. The bending magnets in the storage ring and the booster are colored yellow, quadrupole magnets red, sextupole magnets green, cavity structures blue and the insertion devices are dark green. In addition the source points of the transverse beam size measurement systems for the pinhole systems and the interferometer are shown [15].

The storage ring has a circumference of 240 m and consists of 32 bending magnets in 16 double bend achromats connected by 16 straights. Two straights are needed for injection and the cavities, so 14 can be equipped with IDs. Together with dipole beam lines synchrotron radiation is provided for roughly 50 beamlines.

To serve a variety of user demands at the same time the fill pattern of BESSY II is rather complex:

- A bunch train provides high average photon flux and brilliance.
- A single bunch in the 200 ns gap is used for pseudo single bunch operation and can be separated with a chopper. The chopper is a fast rotating wheel with gaps; this method needs a gap of ≈140 ns [19].

- Another pseudo single bunch produced by resonant excitation of a single bunch. The method is called pulse picking by resonant excitation (PPRE) and provides a bunch with a significantly larger emittance, which can be separated with an aperture by blocking the SR coming from the other bunches [20].
- The slicing bunches. A small slice of a beam is energy modulated with a laser pulse and the radiation of this part is separated from the radiation of rest of the beam yielding shorter pulses [21].

The fill pattern for standard user operation for a total current of 300 mA is shown in Fig. 2.2. The multi bunch train including the three slicing bunches consists of 300 bunches and in the gap the single bunch and the PPRE bunch are placed. Bunches in the bunch train have a current of about 0.95 mA each, where the special bunches have a higher current of 3 mA or 4 mA. Standard user operation is running in top up mode to retain the total beam current of 300 mA.

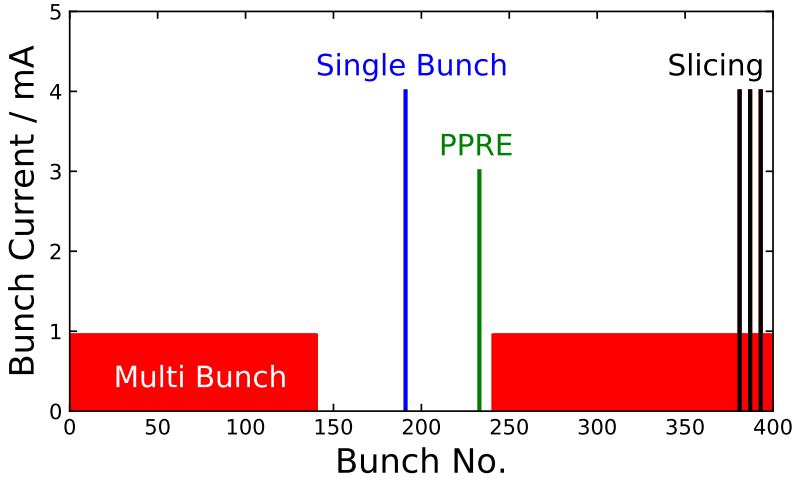

Figure 2.2.: BESSY II fill pattern in standard user mode featuring the multibunch train, the single bunch, the PPRE bunch and three slicing bunches.

For two weeks a year the machine is running in the so called low-α mode, were the magnet optics is changed to have a smaller momentum compaction factor α, to provide shorter pulses than in the standard user mode [4]. According to [22, Eq. 8.47] the zero current bunch length σ_0 is given by

$$\sigma_0 = \frac{c|\eta_c|}{2\pi f_s}\frac{\sigma_E}{E_0}, \tag{2.1}$$

where f_s is the synchrotron frequency, E_0 the electron energy, σ_E the rms energy spread and η_c the phase slip factor. The phase slip factor is defined as

$$\eta_c = \frac{1}{\gamma^2} - \alpha_c, \tag{2.2}$$

with the momentum compaction factor α_c. The synchrotron frequency is [22, Eq. 6.35]

$$f_s = f_{\mathrm{rev}}\sqrt{\frac{2\pi h\eta_c e U_0 \cos\psi_s}{\beta c p_0}}, \tag{2.3}$$

where f_{rev} is the revolution frequency, h the harmonic number, e the elementary charge, U_0 the total acceleration voltage per turn, ψ_s the synchronous phase and p_0 the particle momentum. Inserting this into Eq. 2.1, using the definition of the energy spread $\delta_0 = \frac{\sigma_E}{E_0}$ and the approximations $|\eta_c| \approx |\alpha_c|$, $\beta \approx 1$ and $\cos\psi_s \approx 1$ the zero current bunch length becomes

$$\sigma_0 = c\delta_0 \sqrt{\frac{E|\alpha_c|}{ef_{\mathrm{rev}}|U'|}}, \tag{2.4}$$

where $U' = 2\pi f_{\mathrm{rf}} U_0$ is the gradient of the net accelerating voltage. So with reducing the momentum compaction factor to $\alpha_c = 3.8 \times 10^{-5}$ the bunch length in the low-α operation is about 3 ps, which is about 5 times shorter than in standard user mode [3].

The drawback of low-α operation is however, that bunches can become unstable due to the emission of coherent synchrotron radiation (CSR). This effect is called microwave or bursting instability and occurs depending on the bunch length and a threshold current I_{thr}. For a constant bunch length the threshold current is proportional to the momentum compaction factor $I_{\mathrm{thr}} \propto \alpha_c$ [3]. In low-α weeks a third of the time the total current is reduced to 15 mA, which corresponds to single bunch current of about 40 µA and is below the bursting threshold. The remaining time the current is set to 100 mA but the SR is still not comparable to the standard user conditions in terms of brilliance and flux. Moreover, low-α operation is provided in decay mode, since the top up conditions cannot be fulfilled. Therefore the low-α operation and thus shorter pulses can only be offered for a limited time, because most users need higher photon flux or more stable beam conditions.

2.2. BESSY VSR Upgrade

The low-α mode cannot provide short pulses and high average photon flux simultaneously, as discussed in the previous section. Considering again Eq. 2.4 the only variable parameter to change bunch length for an already existing storage ring apart from the momentum compaction factor is the voltage gradient. Thus, the idea is to reduce the bunch length with a significantly higher voltage gradient U' without affecting the threshold current. The upgrade of BESSY II to the variable pulse length storage ring BESSY VSR [3, 10] tries to achieve short pulses while maintaining high average photon flux utilizing superconducting (SC) cavities.

With a single SC cavity for longitudinal focusing all bunches would have a short bunch length. For BESSY II this single cavity setup [3] seems to be difficult to realize, because of strong impedance and lifetime problems when storing up to 300 mA in those short bunches. The scheme was then modified with an additional SC cavity to store long and short bunches at the same time [9]. The two cavities generate a beat in the sum voltage leading to an alternation of long and short bunches.

For BESSY VSR it is planned to add two 1.5 GHz SC cavities (3$^{\mathrm{rd}}$ harmonic) and two 1.75 GHz SC cavities (3.5$^{\mathrm{th}}$ harmonic) to the existing normal conducting (NC) cavities. An overview for the BESSY VSR cavities is given in Tab. 2.2 and the voltage gradients and the resulting beat pattern for 2.5 periods of the NC cavities is shown in Fig. 2.3.

The 400 positions where bunches can be stored are then be divided into buckets where the gradients of the SC cavities add up or cancel out. For the buckets where

Table 2.2.: BESSY VSR cavity system parameters [3, Tab. 1.4].

Cavity	Frequency / GHz	Operating voltage / MV	Number
NC	0.5	1.5	4×1 cell
SC_1	1.5	20	2×5 cells
SC_2	1.75	17.14	2×5 cells

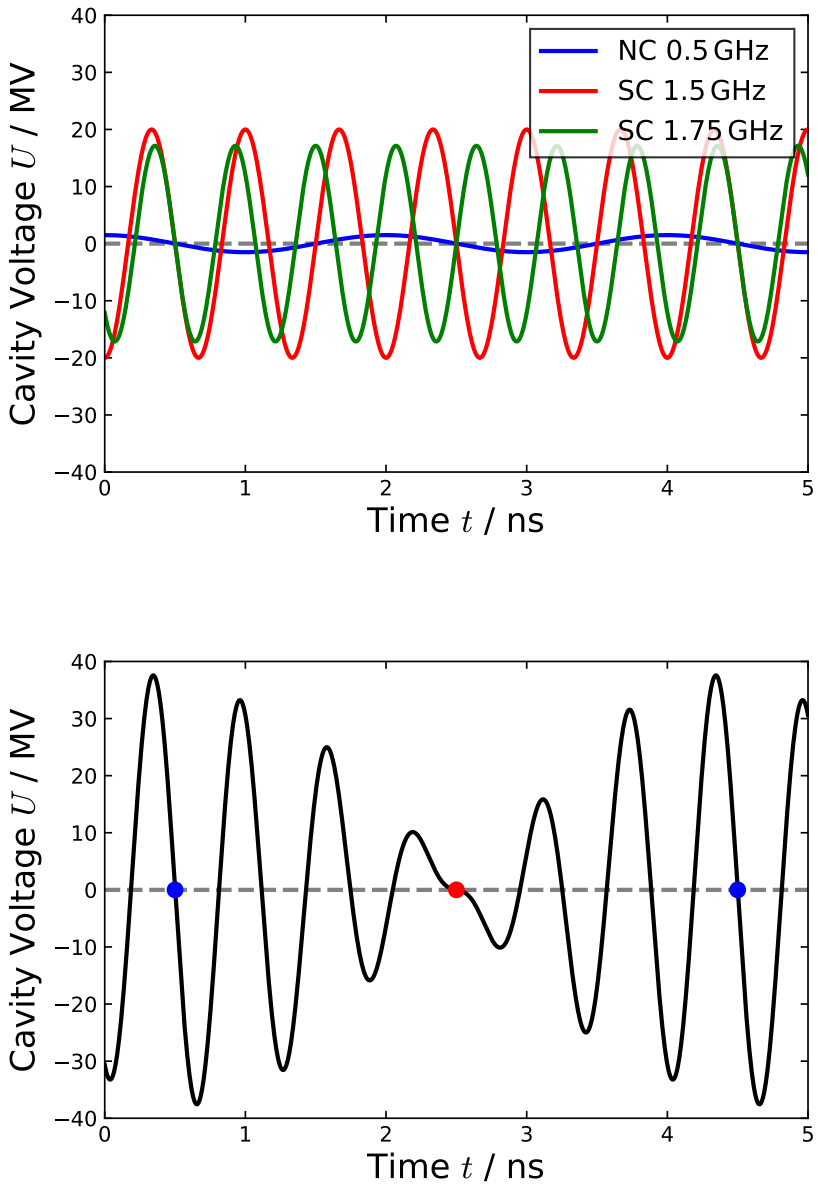

Figure 2.3.: BESSY VSR cavity voltages as a function of time for the three cavity systems from Tab. 2.2 (top) and the sum voltage (bottom). The blue dots at 0.5 ns and 4.5 ns denote positions where a short bunch can be stored and the red dot at 2.5 ns a position for a long bunch.

the gradients of the SC cavities cancel the bunch length is defined by the NC cavities and the properties stay approximately the same as for BESSY II. When the gradients add up however, the resulting gradient in the bucket is 80 times higher than the

gradient from the NC cavities leading to an about a factor 9 shorter bunch length at constant current and an 80 times higher threshold current. This bunch length and threshold current scaling for the short buckets compared to the present cavity systems are shown in Fig. 2.4. The plotted bunch lengths also include a simplified estimation of the effect from CSR and the potential well distortion by the beam current [3].

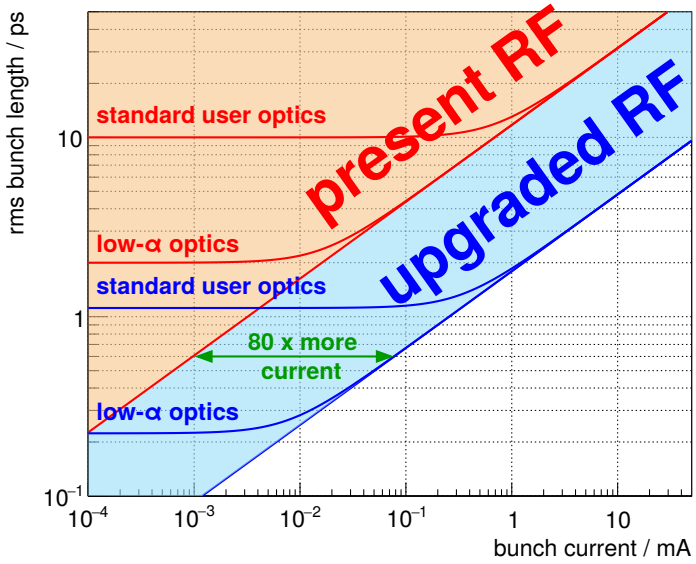

Figure 2.4.: Expected bunch length as a function of beam current for BESSY II with the existing cavity "RF" system (red) and BESSY VSR with the upgraded cavity system (blue). The lines show the threshold for the standard user and the low-α mode, respectively [3].

The baseline and a possible extended BESSY VSR fill pattern enabled by the alternating bucket scheme for a total current of 300 mA are depicted in Fig. 2.5. The baseline fill pattern includes two bunch trains consisting of 75 long buckets each where the major part of the current is stored. Since compared to BESSY II there are only half the number of long bunches available the beam current approximately has to be doubled. High current single bunches are stored in the two 100 ns gaps between the trains, one in a long and one in a short bucket. These bunches can be separated with a mechanical chopper. Additionally short bunches inside a train are filled for the slicing experiments. In a possible extension of this fill pattern all short buckets inside the bunch trains are populated.

With the complex fill patterns in Fig. 2.5 it is planned to store very different bunches at the same time. The parameters of those bunches are summarized in Tab. 2.3 and differ in beam current, peak current as well as in bunch length up to one order of magnitude. Hence, collective effects make it necessary to have bunch resolved diagnostics for BESSY VSR.

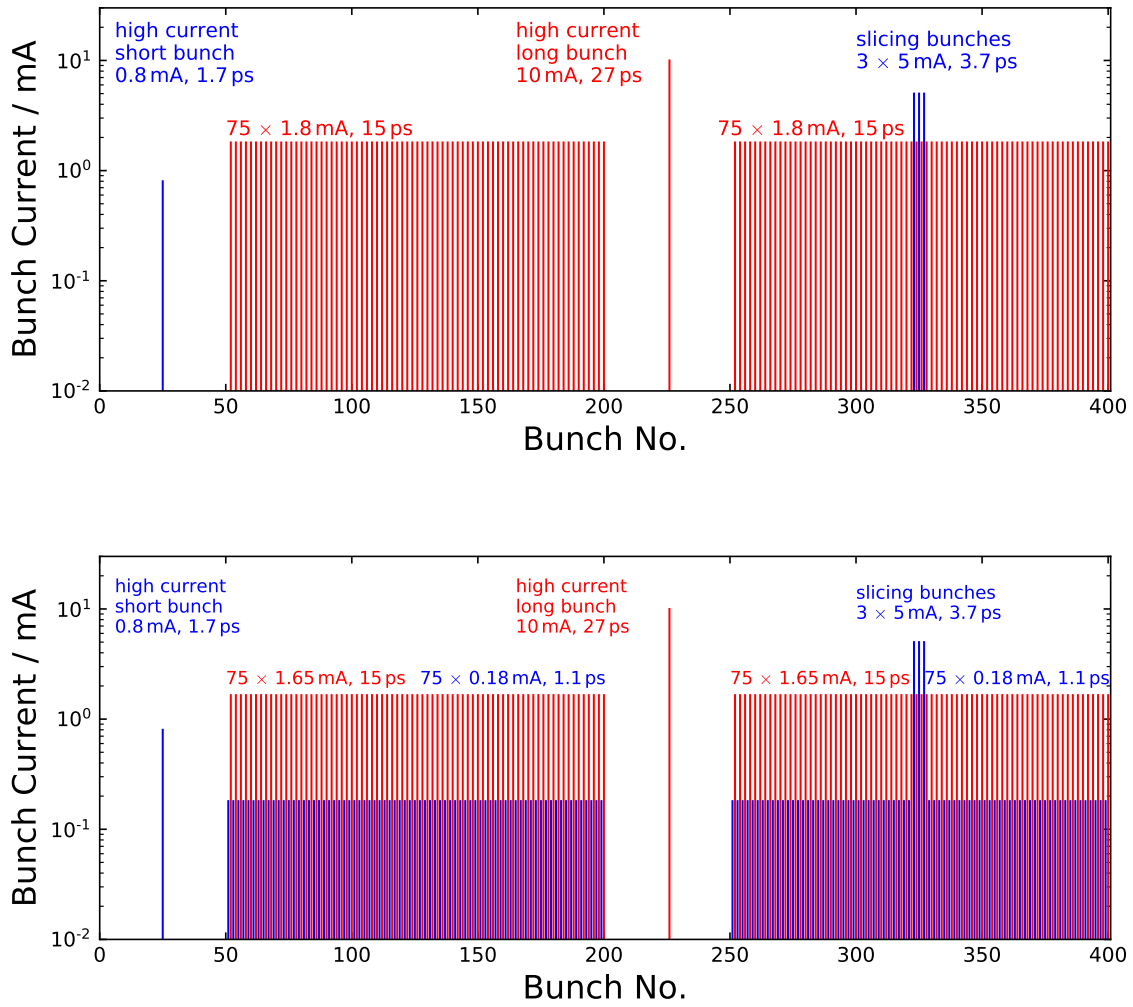

Figure 2.5.: Baseline (top) and extended option (bottom) fill pattern for BESSY VSR, simultaneously storing short bunches (blue) and long bunches (red). The bunch currents and expected bunch lengths for the different bunch types are shown [3].

Table 2.3.: BESSY VSR bunch parameters, including the bunch length, bunch current and the peak current calculated from bunch charge divided by rms bunch length [3].

	No.	**Length / ps**	**Current / mA**	**Peak current / A**
Std. long bunch	150	15	1.8	96
Std. short bunch	150	1.1	0.18	131
Long single bunch	1	27	10	296
Short single bunch	1	1.7	0.8	376
Slicing bunch	3	3.7	5	1081

3. Interferometric Beam Size Measurement

Interferometry methods using synchrotron radiation to measure the transverse beam size have been installed at numerous storage rings. The theory is introduced in [12] and shortly outlined in the following chapter. At first the basic theory of spatial coherence of light and the van Cittert-Zernike theorem are introduced. Then the properties of synchrotron radiation are discussed and applied. Finally the principle of the double slit interferometer is described.

3.1. Spatial Coherence and the van Cittert-Zernike Theorem

Consider a setup shown in Fig. 3.1. The light is emitted from a broad source, falls onto an obstacle and is observed on the screen.

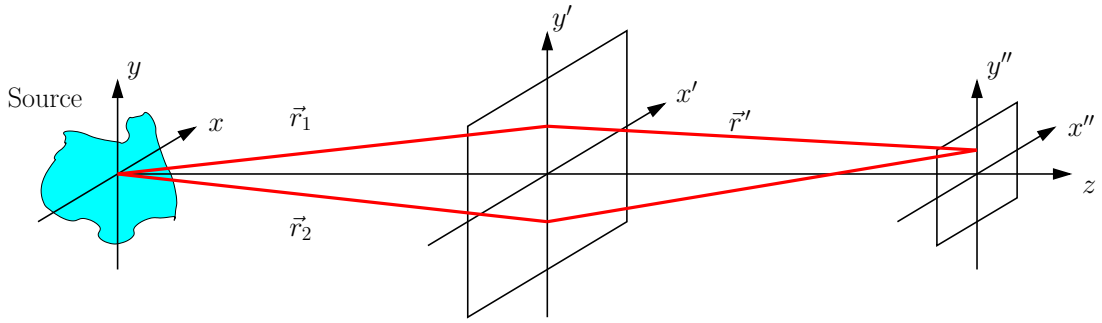

Figure 3.1.: Sketch for the derivation of spatial coherence of light. The light is emitted from a broad source in (x, y), falls onto an obstacle in (x', y') and is observed on the screen in (x'', y'').

First Order Coherence Let $E(\vec{r}_1, t_1)$ and $E(\vec{r}_2, t_2)$ be two modes of one photon emitted simultaneously from one point source, observed at $\vec{r}_1$ at a time t_1 and at $\vec{r}_2$ at a time t_2, respectively. The sum amplitude observed at $\vec{r}'$ is:

$$E(\vec{r}', t_1, t_2) = E(\vec{r}_1, t_1) + E(\vec{r}_2, t_2). \tag{3.1}$$

Substituting the time difference with $\tau = t_2 - t_1$, it follows

$$E(\vec{r}', t) = E(\vec{r}_1, t) + E(\vec{r}_2, t + \tau). \tag{3.2}$$

The intensity observed at $\vec{r}'$ is then given by the square of the absolute value of the sum amplitude:

$$I(\vec{r}',t) = \langle E(\vec{r}',t)E(\vec{r}',t)\rangle = E(\vec{r}',t)E^*(\vec{r}',t) \tag{3.3}$$
$$= [E(\vec{r}_1,t) + E(\vec{r}_2,t+\tau)]\,[E^*(\vec{r}_1,t) + E^*(\vec{r}_2,t+\tau)] \tag{3.4}$$
$$= I(\vec{r}_1) + I(\vec{r}_2) + 2Re\left\{\Gamma_{12}(\tau)\right\}, \tag{3.5}$$

where $\Gamma_{12}(\tau) \equiv \Gamma(\vec{r}_1,\vec{r}_2,\tau)$ and

$$\Gamma_{ij}(\tau) = \langle E\left(\vec{r}_i,t+\tau\right) E\left(\vec{r}_j,t\right)\rangle. \tag{3.6}$$

the (first order) complex mutual coherence function of the light from $\vec{r}_i$ and $\vec{r}_j$. By normalizing it with the auto correlations $\Gamma_{11}(\tau)$ and $\Gamma_{22}(\tau)$, one gets the complex degree of coherence γ_{12}:

$$\gamma_{12}(\tau) = \frac{\Gamma_{12}(\tau)}{\sqrt{\Gamma_{11}(\tau=0)\Gamma_{22}(\tau=0)}} = \frac{\Gamma_{12}(\tau)}{\sqrt{I(\vec{r}_1)I(\vec{r}_2)}}. \tag{3.7}$$

Introducing a phase term $\phi_{12}(\tau)$ the complex degree of coherence can be rewritten as $\gamma_{12}(\tau) = |\gamma_{12}(\tau)|\exp\left[i\phi_{12}(\tau)\right]$ and Eq. 3.5 becomes:

$$I(\vec{r}',\tau) = I(\vec{r}_1) + I(\vec{r}_2) + 2\sqrt{I(\vec{r}_1)I(\vec{r}_2)}|\gamma_{12}(\tau)|\cos\left[\phi_{12}(\tau)\right]. \tag{3.8}$$

The first two terms in Eq. 3.8 are the intensities of the two modes and the third term is the interference term. If $\vec{r}_1 - \vec{r}_2 = 0$, only effects from temporal coherence and if $\tau = 0$, only effects from spatial coherence are observed.

The visibility V is defined by the maximum intensity $I_{\max}$ and the local minimum intensity $I_{\min}$ next to the maximum intensity

$$V = \frac{I_{\max} - I_{\min}}{I_{\max} + I_{\min}}. \tag{3.9}$$

Inserting Eq. 3.8 for $\cos\left[\phi_{12}(\tau)\right] = \pm 1$ the visibility is given by the product of the so called imbalance factor of the two intensities and the absolute value of the complex degree of coherence:

$$V = \underbrace{\frac{2\sqrt{I(\vec{r}_1)I(\vec{r}_2)}}{I(\vec{r}_1) + I(\vec{r}_2)}}_{\text{imbalance factor}}|\gamma_{12}(\tau)|. \tag{3.10}$$

Replacing the complex degree of coherence with the visibility and substituting the phase term with the normalized optical path difference $\psi = 2\pi\Delta l/\lambda$, where λ is the wavelength and Δl the path difference, for spatial coherence the intensity in Eq. 3.8 becomes then:

$$I(\vec{r}') = [I(\vec{r}_1) + I(\vec{r}_2)]\left[1 + \frac{2\sqrt{I(\vec{r}_1)I(\vec{r}_2)}}{I(\vec{r}_1) + I(\vec{r}_2)}|\gamma_{12}(\tau)|\cos(\psi)\right] \tag{3.11}$$
$$= [I(\vec{r}_1) + I(\vec{r}_2)]\left[1 + V\cos(\psi)\right]. \tag{3.12}$$

Van Cittert-Cernike Theorem Above only light emitted from a point source was discussed. Considering again Eq. 3.6 as differential mutual coherence function for a partial coherence of light emitted from $\mathrm{d}\sigma$ of the light source Σ:

$$\Gamma_{12}(\tau)\mathrm{d}\sigma = \langle E\left(\vec{r}_1, t+\tau\right) E\left(\vec{r}_2, t\right)\rangle. \tag{3.13}$$

The complex amplitudes of the sum amplitude from spherical waves at $\vec{r_i}$ are given by:

$$E(\vec{r}_i, t) = \alpha(\vec{r}_i, t)\frac{1}{r_i}\exp\left[-i\left(\omega t - \vec{k}\vec{r}_i\right)\right] \tag{3.14}$$

with $r_i = |\vec{r}_i|$, the wave vector $\vec{k}$, the amplitude $\alpha(\vec{r}_i, t)$ and the angular frequency ω. The differential of the mutual coherence becomes:

$$\begin{aligned}\Gamma_{12}(\tau)\mathrm{d}\sigma &= E\left(\vec{r}_1, t+\tau\right) E^*\left(\vec{r}_2, t\right) &(3.15)\\ &= \alpha(\vec{r}_1, t+\tau)\alpha^*(\vec{r}_2, t)\frac{1}{r_1 r_2}\exp\left[-i\vec{k}\left(\vec{r}_2 - \vec{r}_1\right) - i\omega\tau\right] &(3.16)\end{aligned}$$

and for spatial coherence with $\tau = 0$ simplifies to:

$$\Gamma_{12}\mathrm{d}\sigma = I(\sigma)\mathrm{d}\sigma\frac{1}{r_1 r_2}\exp\left[-i\vec{k}\left(\vec{r}_2 - \vec{r}_1\right)\right]. \tag{3.17}$$

The first order mutual coherence is then given by integrating over the whole source:

$$\Gamma_{12} = \int_\Sigma I(\sigma)\frac{1}{r_1 r_2}\exp\left[-i\vec{k}\left(\vec{r}_2 - \vec{r}_1\right)\right]\mathrm{d}\sigma. \tag{3.18}$$

Normalizing this like in Eq. 3.7 one gets the complex degree of spatial coherence:

$$\begin{aligned}\gamma_{12} = \frac{\Gamma_{12}}{\Gamma_{11}\Gamma_{22}} &= \frac{\int_\Sigma I(\sigma)\exp\left[-i\vec{k}\left(\vec{r}_2 - \vec{r}_1\right)\right]\mathrm{d}\sigma}{\int_\Sigma I(\sigma)\mathrm{d}\sigma} &(3.19)\\ &= \int_\Sigma f(\sigma)\exp\left[-i\vec{k}\left(\vec{r}_2 - \vec{r}_1\right)\right]\mathrm{d}\sigma, &(3.20)\end{aligned}$$

where $f(\sigma)$ is the normalized intensity distribution of the source. Representing $f(\sigma)$ as a two dimensional distribution $f(x, y)$ Eq. 3.20 becomes:

$$\gamma_{12}(\nu_x, \nu_y) = \iint f(x, y)\exp\left[-2\pi i\left(\nu_x x + \nu_y y\right)\right]\mathrm{d}x\mathrm{d}y, \tag{3.21}$$

with the definition of the spatial frequencies ν_x, ν_y given by:

$$\nu_x = \frac{x_2 - x_1}{\lambda L}, \quad \nu_y = \frac{y_2 - y_1}{\lambda L}, \tag{3.22}$$

where $\lambda = \frac{2\pi}{|\vec{k}|}$ is the wavelength and L is the distance between the source and the interference obstacle. For the derivation of the spatial frequencies see also Eqs. B.20 to B.22 in Appendix B. Equation 3.21 is the van Cittert-Zernike theorem. It states that the complex degree of spatial coherence is given by a Fourier transform of the intensity distribution of the source object. This means that the visibility in an interference pattern of a point source is 1 and gets smaller for an extended source, i. e. the contrast in the interference pattern gets worse [12, 23, 24].

3.2. Modifications for Synchrotron Radiation

Until now it was only spherical radiation emitted from point sources considered. Synchrotron radiation however, is emitted from relativistic electrons and the spectral and spatial power distribution of the emitted energy inside a bending magnet is given by [22, Eq. 22.105]:

$$\frac{\mathrm{d}^2 W}{\mathrm{d}\Omega \mathrm{d}\omega} \propto \gamma^2 \left(\frac{\omega}{\omega_\mathrm{c}}\right)^2 \left(1+\gamma^2\theta^2\right)^2 \left[K_{2/3}^2(\xi) + \frac{\gamma^2\theta^2}{1+\gamma^2\theta^2} K_{1/3}^2(\xi)\right], \tag{3.23}$$

$$\xi = \frac{1}{2}\frac{\omega}{\omega_\mathrm{c}}\left(1+\gamma^2\theta^2\right)^{3/2}, \tag{3.24}$$

where $\omega = kc$, Ω the solid angle, γ the Lorentz factor, θ the vertical opening angle and K_ν are modified Bessel functions of the second kind. The two terms inside the square brackets in Eq. 3.23 are the two polarisation modes of SR, representing the σ-polarisation and the π-polarisation. The spatial and spectral distribution of synchrotron radiation energy is plotted in Fig. 3.2 for both SR polarisation modes. In the following the effects for the vertical and horizontal plane in case of synchrotron radiation are discussed.

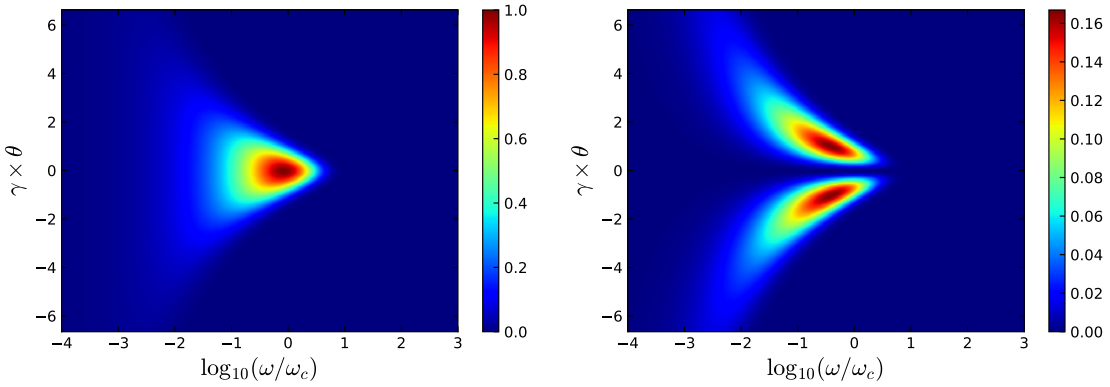

Figure 3.2.: Spatial and spectral distribution of synchrotron radiation power according to Eq. 3.23 for σ-polarisation (left) and π-polarisation (right). The color code and scale are normalized to the maximum power for σ-polarisation.

In the vertical direction the intensities are different, because of the angular distribution of synchrotron radiation and the dispersion of electrons in the beam. Thus to get the vertical visibility it has to be integrated over the angular distribution:

$$V_\mathrm{v}' = \int V \mathrm{d}\varphi = \int \frac{2\sqrt{I_1(\varphi) I_2(\varphi)}}{I_1(\varphi) + I_2(\varphi)} \mathrm{d}\varphi \, |\gamma_{12}|, \tag{3.25}$$

with $I_1(\varphi)$ and $I_2(\varphi)$ being the intensities of two modes of one photons. Note that for simplicity the phase of the SR is not considered here. Since it is intended to use visible light, the opening angle of the synchrotron beam in the order of mrad is much higher than the electron dispersion of usually a few µrad and the later can be neglected. The effect of the imbalance of the two intensities is depicted in Fig. 3.3. The imbalance factor introduced in Eq. 3.10 is plotted against the intensity ratio I_1/I_2. At a ratio of 0.8 the imbalance factor is still close to 1, namely at 0.9938.

Thus the effect from the angular distribution of synchrotron radiation is insignificant in the visible region and the integration from Eq. 3.25 will not be considered.

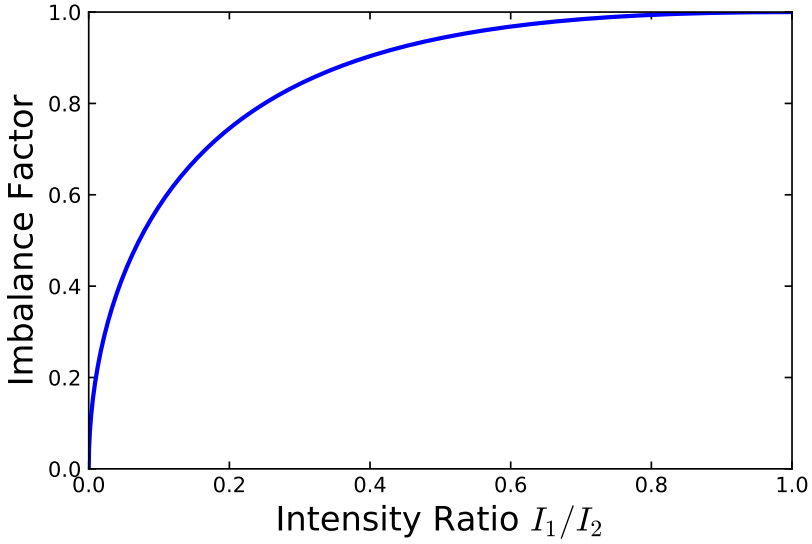

Figure 3.3.: Intensity imbalance factor defined in Eq. 3.10 as a function of the intensity ratio I_1/I_2.

Another effect is that photons from different longitudinal positions are observed, which is defined by the horizontal acceptance of the beamline. Therefore the visibility is given by a superimposing integral along the longitudinal beam position s:

$$V_{\mathrm{v}}'' = \int V \mathrm{d}s = \iint \frac{2\sqrt{I_1(s)I_2(s)}}{I_1(s)+I_2(s)} f(y,s) \exp\left[-2\pi i \nu_y y\right] \mathrm{d}s\mathrm{d}y, \tag{3.26}$$

where $I_1(s)$ and $I_2(s)$ are the intensities of the two photon modes and $f(y,s)$ is the vertical beam profile at s. For the impact of possible intensities imbalances the discussion from above applies and the visibility becomes:

$$V_{\mathrm{v}}'' = \int \overline{f}(y) \exp\left[-2\pi i \nu_y y\right] \mathrm{d}y, \tag{3.27}$$

where $\overline{f}(y)$ is the mean vertical beam profile along the horizontal acceptance.

Measuring the horizontal beam size, the effects of intensity imbalances and the horizontal acceptance again apply. In addition the curved trajectory of the beam in the bending magnet has to be considered. This leads to the following modification of the visibility in the horizontal case:

$$V_{\mathrm{h}}' = \int \frac{2\sqrt{I_1(\vartheta)I_2(\vartheta)}}{I_1(\vartheta)+I_2(\vartheta)} I(\vartheta)\gamma_{12}(\vartheta)\mathrm{d}\vartheta \tag{3.28}$$

$$= \iint \frac{2\sqrt{I_1(\vartheta)I_2(\vartheta)}}{I_1(\vartheta)+I_2(\vartheta)} I(\vartheta) f\left[x-\rho(1-\cos\vartheta),\vartheta\right] \exp\left(-2\pi i \nu_x x\right) \mathrm{d}x\mathrm{d}\vartheta, \tag{3.29}$$

with the observation angle ϑ, the intensities $I_1(\vartheta)$ and $I_2(\vartheta)$ of the two photon modes, the intensity scale factor in the horizontal direction $I(\vartheta)$ and the beam

profile $f\left[x-\rho(1-\cos\vartheta),\vartheta\right]$ depending on the observation angle and therefore also depending on the longitudinal position and the bending radius ρ. The so called incoherent depth of field effect in Eq. 3.29 becomes relevant for a large bending radius and small beam sizes [12, 25] and the effect for BESSY II is discussed in Section 4.5.

3.3. Double Slit Interferometer Concept

To measure spatial coherence an interferometer which divides the wavefront is needed. Figure 3.4 shows schematically the setup of the SR interferometer. The light from a bending magnet is guided to the interferometer systems. The source point is imaged with a lens onto a CCD camera and a double slit or other diffraction obstacles can be illuminated with the synchrotron radiation to get a diffraction pattern. In addition the light passes through a polarisation filter, because of the two polarisation of SR, and a bandpass filter, as the spatial frequencies Eq. 3.22 change with the wavelength, to obtain an interference pattern from a monochromatic polarized ray.

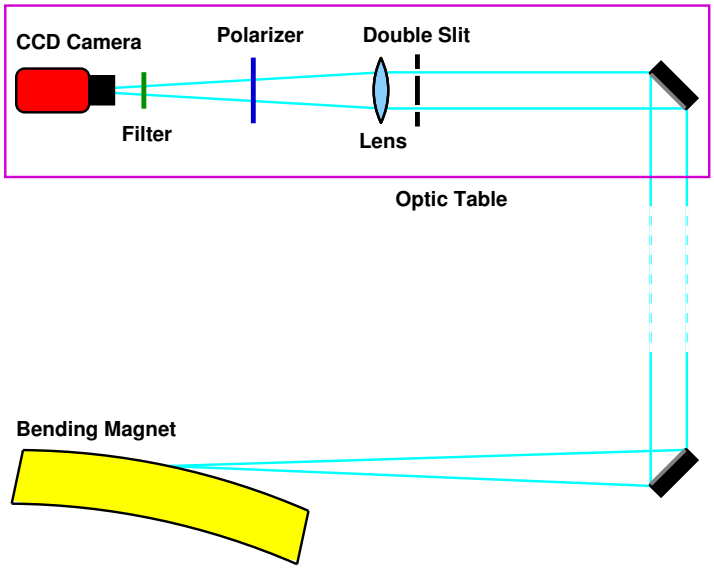

Figure 3.4.: Sketch of the Double Slit Interferometer.

The interference pattern from a double slit can be described in two parts. First the envelope is given by the interference pattern from a single slit and the intensity is:

$$I(x'') = I_0 \,\mathrm{sinc}^2\left(\frac{\pi a}{\lambda f}x''\right), \tag{3.30}$$

where x'' is the position at the detector, a the full single slit width, f the effective distance between the double slit and the detector screen, λ the wavelength and I_0 the intensity at the slit. The second part is the modulation of the pattern due to the coherence effects described in Section 3.1. The double slit interference pattern at the detector plane of a broad source is derived in Appendix B and is given by:

$$I(x'') = (I_1 + I_2)\,\mathrm{sinc}^2\left(\frac{\pi a}{\lambda f}x''\right)\left[1 + V\cos\left(\frac{2\pi d}{\lambda f}x'' + \psi\right)\right], \tag{3.31}$$

with the full double slit separation d, the photon phase ψ, the intensity I_1 and I_2 at the respective slits and the visibility V defined in Eq. 3.9. The interference patterns of a single slit and a double slit with the same single slit widths for a point source with $V = 1$ and $\psi = 0$ are shown in Fig. 3.5.

Figure 3.5.: Interference patterns of a single slit (left) and a double slit (right) with the same single slit widths of a point source and without any phase shift.

To illustrate the meaning of the visibility, the double slit interference pattern is plotted for $V = 1$ and $V = 0.5$ in Fig. 3.6. For a point source the visibility is 1 and all local minima are zero. For a broader source the local minima will not be zero. Measuring the visibility (and the phase) gives a parameter from which the size (shape) of the source, which is in this case is the electron beam, can be deduced.

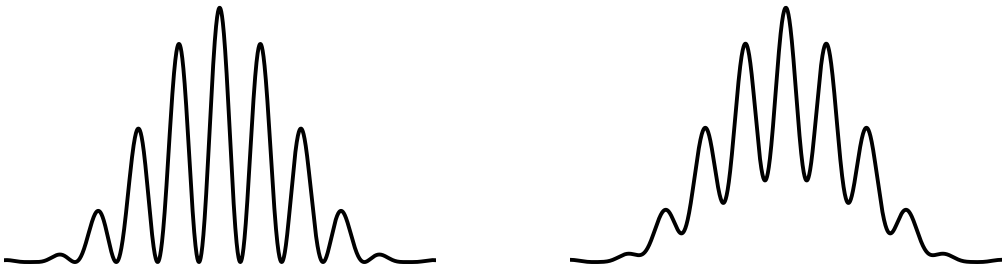

Figure 3.6.: Double slit interference patterns for a point source with a visibility $V = 1$ (left) and a broad source with a visibility $V = 0.5$ (right), both at a phase of $\psi = 0$.

The general method is therefore to measure the visibility (more specifically the absolute value of the complex degree spatial coherence) and the phase for different spatial frequencies, e.g. for different slit separations or wavelengths, since the distance to the source is rather difficult to vary on a significant order. Rewriting the complex degree spatial coherence and the phase as a function of the slit separation or the wavelength, respectively:

$$\gamma(d,\lambda) = \int \mathrm{d}x f(x) \exp\left(-i\frac{2\pi d}{\lambda L}x\right) \tag{3.32}$$

$$= \mathcal{F}(d,\lambda) = \mathcal{COS}(d,\lambda) + i\mathcal{SIN}(d,\lambda) \tag{3.33}$$

$$\psi(d,\lambda) = \arctan\frac{\mathcal{SIN}(d,\lambda)}{\mathcal{COS}(d,\lambda)}, \tag{3.34}$$

where $\mathcal{SIN}$ denotes the Fourier sine transform and $\mathcal{COS}$ the Fourier cosine transform of $f(x)$. With this one can get the beam profile by a Fourier transform of $\gamma(d,\lambda)$ or just the symmetric contributions from the Fourier cosine transform, since it is generally assumed to have a symmetric beam [12].

Assuming a Gaussian distribution of the beam profile the complex degree of coherence can furthermore be calculated. Consider a centered normalized Gaussian:

$$f(x) = \frac{1}{\sigma\sqrt{2\pi}} \exp\left[-\frac{1}{2}\left(\frac{x}{\sigma_x}\right)^2\right] \tag{3.35}$$

where σ_x is the rms width of the beam and the Fourier transform from Eq. 3.32 can be solved:

$$\gamma(d,\lambda) = \int \mathrm{d}x f(x) \exp\left(-i\frac{2\pi d}{\lambda L}x\right) \tag{3.36}$$

$$= \int_{-\infty}^{\infty} \mathrm{d}x \frac{1}{\sigma_x\sqrt{2\pi}} \exp\left[-\frac{1}{2}\left(\frac{x}{\sigma_x}\right)^2\right] \exp\left(-i\frac{2\pi d}{\lambda L}x\right) \tag{3.37}$$

$$= \exp\left[-2\left(\frac{\pi\sigma_x d}{\lambda L}\right)^2\right]. \tag{3.38}$$

Here $|\gamma(d,\lambda)| = \gamma(d,\lambda)$ and by neglecting any intensity imbalances and field depth effects the visibility becomes:

$$\boxed{V(d,\lambda) = \exp\left[-2\left(\frac{\pi\sigma_x d}{\lambda L}\right)^2\right].} \tag{3.39}$$

With this it is possible to obtain the beam size by doing a measurement series for different slit separations or wavelengths and fitting the measured visibility with Eq. 3.39.

It is also possible to get the beam size from just one measurement of the visibility, to setup a simple online beam size monitor. Solving Eq. 3.39 for the rms beam size yields:

$$\boxed{\sigma_x \overset{|\gamma|=\gamma}{=} \frac{\lambda L}{\pi d}\sqrt{\frac{1}{2}\ln\left(\frac{1}{|\gamma|}\right)}} \tag{3.40}$$

$$\boxed{\overset{I_1=I_2}{=} \frac{\lambda L}{\pi d}\sqrt{\frac{1}{2}\ln\left(\frac{1}{V}\right)}.} \tag{3.41}$$

4. Implementation

This chapter describes the steps of implementing the interferometric beam size monitor and the data evaluation. The conditions given by the diagnostics beamline are introduced and further considerations for the beam size monitor are made. The interferometer setup and the components are presented, the data analysis process is outlined and an estimation of the measurement uncertainties is given.

4.1. Optical Diagnostics Beamline

The light is guided vertically out of plane to the top of the storage ring bunker, allowing operation while beam shutters are closed, e. g. at injection. The synchrotron radiation is extracted by a platinum mirror and is guided with two additional mirrors to an optic table. At the optic table, which was installed in late 2015, new diagnostic methods using synchrotron radiation in the visible region can be tested and implemented.

Beam Line Acceptance The area illuminated by synchrotron radiation on the optical table has a diameter of roughly 30 mm to maximum 35 mm. This correlates to a maximum opening angle or horizontal acceptance of 2.3 mrad assuming a distance of 15 m to the source point. In the vertical plane however, the position of the illuminated area relative to the center of the synchrotron beam could not be determined. From the properties of synchrotron radiation shown in Fig. 3.2 one would expect a dip of the intensity in the center. The angular distribution of the SR calculated with Eq. 3.23 is shown exemplarily for a BESSY II bending magnet at a wavelength of 500 nm in Fig. 4.1.

For an opening angle of about 2 mrad it should still be possible to see a dip in the vertical intensity profile at the diagnostics beamline. However it was not possible to get a clear result with different wavelength and polarisations which region of the vertical opening angle is observed on the optical table. It has to be considered that it is likely not the central region, but rather a region near the peaks at ± 2 mrad where the variation of the intensity is minimal. Another possibility is that the beam spot might be smeared out or distorted by the mirrors reflecting the beam to the optical table, which could have a significant impact on the interference pattern.

Spectrum The spectral distribution of the synchrotron radiation was measured with a compact CCD spectrometer [26]. The measurement was done during standard user operation at a current of 250 mA. The SR was focused with the 1 m focal length lens also used for the interferometer (see Section 4.3) onto a cosine corrector [27] and the spectrum was measured with an exposure time of 1 s. This measurement was repeated with the polarisation filter used for the interferometer (see Section 4.3) for σ-polarisation and π-polarisation and in addition the background was measured. The measured spectra are shown in Fig. 4.2. Note that no

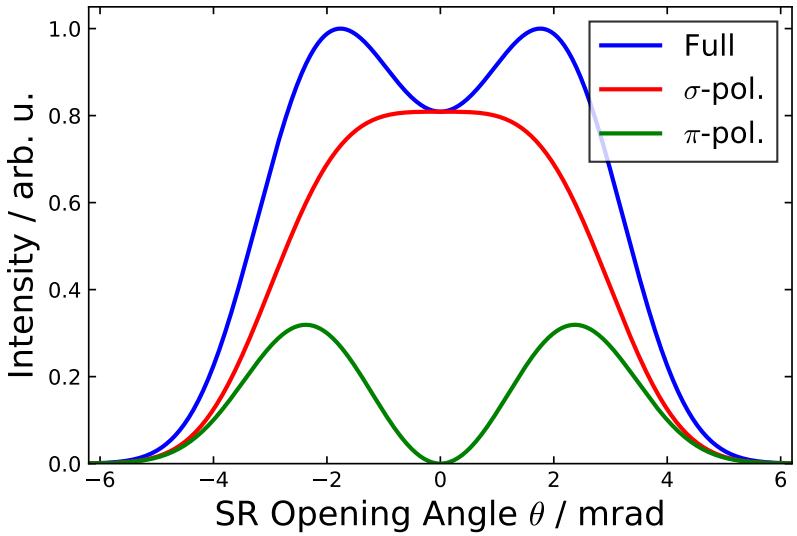

Figure 4.1.: Simulation of the angular distribution of the SR at a wavelength of 500 nm at an energy of 1.7 GeV and a bending radius of 4.35 m for σ-polarisation and π-polarisation.

correction for the spectrometer response was applied and therefore only qualitative statements can be made.

The maximum intensity was observed for wavelengths between 450 nm and

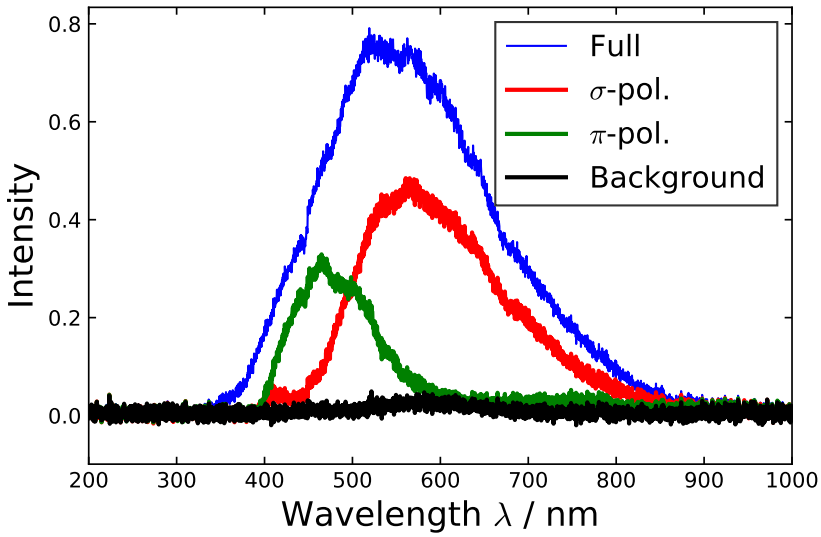

Figure 4.2.: Qualitative measurement of the synchrotron radiation spectrum without and with a polarisation filter set for σ-polarisation and π-polarisation. The measurement was done in standard user operation at 250 mA with the CCD spectrometer and without any response correction [26].

650 nm and the intensity reduces towards higher and lower wavelengths. The intensity decrease at higher wavelength is caused due the less emitted photons. A simulation of the spectral photon flux is also shown in Fig. 4.3 for a total beam current of 0.2 pA at an energy of 1.7 GeV integrated over an opening angle of 6.7 mrad positioned in the center of the SR beam [28].

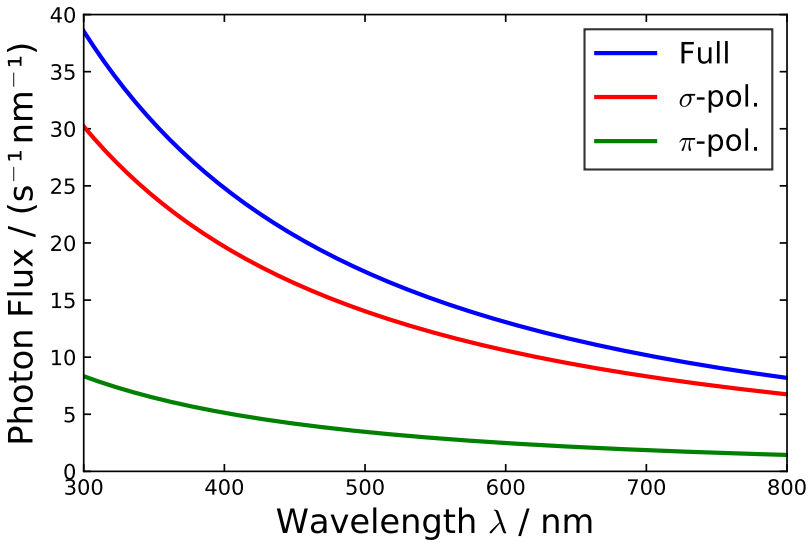

Figure 4.3.: Simulation of the spectral distribution of the photon flux at the diagnostic beam line for a current of 0.2 pA at an energy of 1.7 GeV integrated over an opening angle of 6.7 mrad positioned in the center of the SR beam.

The simulation also shows a decrease of the photon flux towards higher wavelengths. In addition the mirror reflectance is optimized for the synchrotron radiation in the visible region, which causes an intensity decrease for higher wavelengths. For lower wavelength the abrupt decrease is mainly caused by the response of the CCD spectrometer or the fiber cables used, so that almost no radiation is detected below a wavelength of 350 nm. Note that the lens position was optimized for the maximum in spectrum at wavelength around 550 nm, which also reduces the intensity for lower and higher wavelengths.

The measured maxima of the spectra of the two polarisations are different. The spectrum for π-polarisation has its maximum at about 450 nm and almost vanishes for wavelengths above 600 nm, whereas the spectrum for the σ-polarisation is significantly lower for wavelength below 450 nm and has its maximum around 575 nm. From the simulation in Fig. 4.3 however, one would expect that the photon flux of the σ-polarisation is always higher than the photon flux from π-polarisation and it is not known what is causing the separation and the observed intensities for the different polarisations.

4.2. Preparatory Considerations for the Setup

The visibility introduced in Chapter 3 is the only measurement parameter from which the beam size is calculated. So, before setting up the double slit interferometer or any doing measurements some considerations are made to understand how the different parameters affect the visibility and to get a better understanding of the parameter visibility itself. For a Gaussian beam and no intensity imbalance the visibility is given by Eq. 3.39 and depends on four parameters. The beam size is the parameter which is obtained by measuring the visibility and the other three parameters can be set but are limited by the properties of the beam line.

The maximum double slit separation is limited by the width of the illuminated

area by SR on the optical table. Not using the edges of the area and considering a finite single slit width of a few millimeter the maximum double slit separation is limited to below 30 mm. According to Fig. 4.2 the wavelength can be chosen between 400 nm and 800 nm and concerning a high photon flux a wavelength between 450 nm to 650 nm would be optimal. The distance from the source point to the optical table is roughly 15 m. For convenient tests at the optical table it is only possible to elongate this by about 1 m, which is however only little compared to absolute value.

In addition it is important to know for which beam sizes the setup is sensitive. For this purpose at first the error of the beam size is shown as a function of the visibility in Fig. 4.4 for various slit separations, a distance of the double slit to the source of 15 m at a wavelength of 550 nm. The error of the beam size is calculated by error propagation from Eq. 3.41 assuming a double slit separation error of 50 µm, an error of 0.1 m for the distance of the double slit to the source and a 0.01 uncertainty of the visibility measurement.

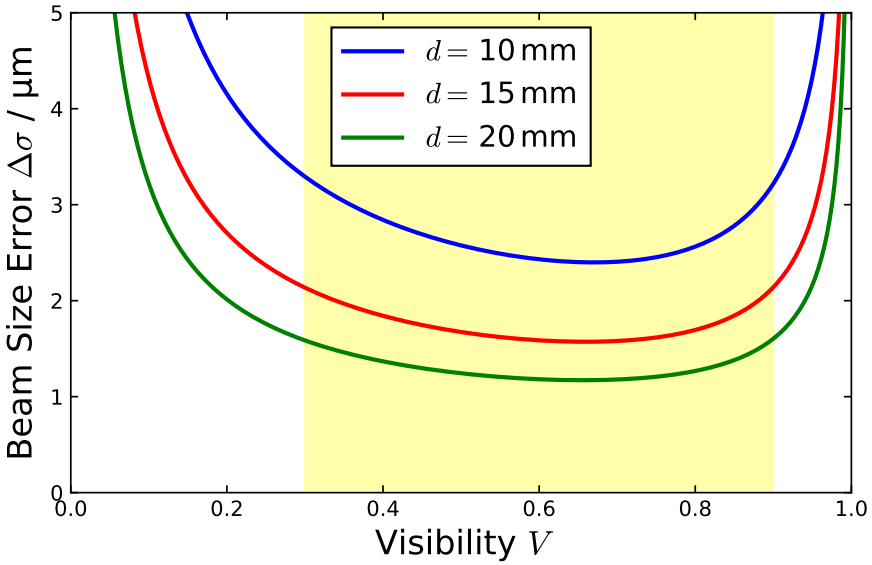

Figure 4.4.: Beam size error as a function of the visibility for various slit separations at wavelength of 550 nm and a distance of the double slit to the source of 15 m. The slit separation uncertainty was set to 50 µm, the distance to the source uncertainty to 0.1 m and the visibility uncertainty to 0.01. The shaded area illustrates the visibility region for minimal beam size errors.

The error of the beam size is nearly constant for a visibility region from 0.3 to 0.9 and increases significantly for visibilities near 0 and 1. The tilt towards higher visibilities is caused by the contribution by the distance to the source and the double slit separation error.

The beam size is not shown directly in Fig. 4.4, but for each parameter configuration the visibility correlates to a particular beam size according to Eq. 3.41. Therefore the beam size region for which the respective parameter combination is sensitive can be shown by plotting the beam size error as a function of the beam size. This is shown in Fig. 4.5 for the same parameter configurations as in Fig. 4.4.

A setup with a larger double slit separation is more sensitive for smaller beam sizes, but the absolute range where the beam size can be measured with a roughly constant error gets smaller. The absolute measurement error increases for larger double slit

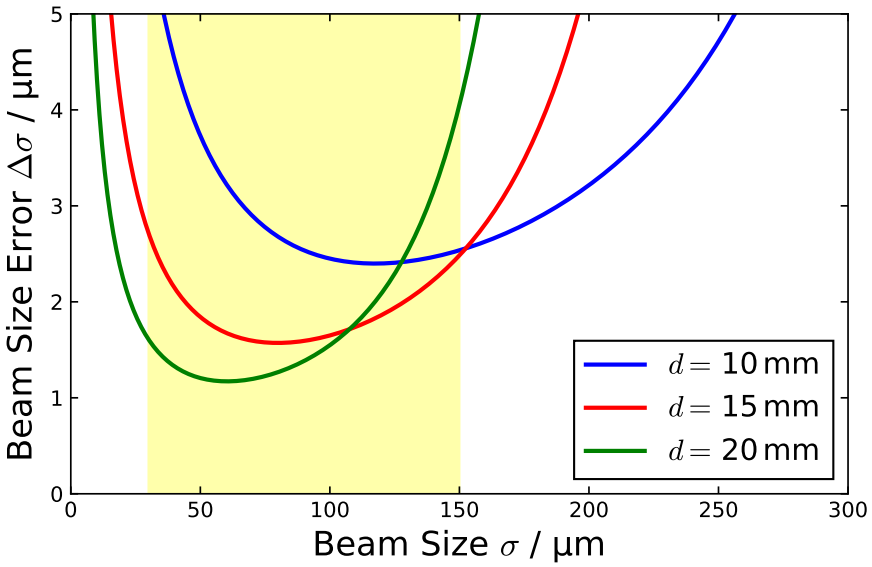

Figure 4.5.: Beam size error as a function of the beam size for various slit separations calculated from Fig. 4.4 at wavelength of 550 nm and a distance of the double slit to the source of 15 m. The slit separation uncertainty was set to 50 µm, the distance to the source uncertainty to 0.1 m and the visibility uncertainty to 0.01. The shaded area illustrates the interesting region for BESSY II beam sizes.

separation, but note that the minimum of the relative error stays constant for each parameter combination.

At BESSY II the interesting region for beam sizes the system should be able to measure are in the range from 30 µm to about 150 µm, which is also illustrated in Fig. 4.5. Combining this and the region for the visibility from Fig. 4.4 the visibility is shown as a function of the beam size for various slit separations with the same parameters for the wavelength and the distance to the source in Fig. 4.6 according to Eq. 3.41. In the beam size regions for which the visibility is near 0 or 1 the visibility changes only little for significant changes of the beam sizes, leading to the large measurement errors shown in Fig. 4.4. To minimize this effect the visibility should be measured in a region with a maximal change of the visibility for a change of the beam size, for which in this case a slit separation of 15 mm to 20 mm would be optimal.

Note that the same discussion as made for varying the double slit separation also applies for a possible variation of the wavelength. In addition only the impact of exemplary statistical errors was considered. Further considerations of the actual error contributions and the discussion of possible systematic errors are made in Section 4.5.

4.3. Double Slit Interferometer Setup

An image of the double slit interferometer setup at the diagnostics beam line is shown in Fig. 4.7. The synchrotron radiation is guided along an optic rail where the components of the interferometer are mounted. After the double slit the radiation passes through the first lens, a polarisation filter, a second lens, a bandpass filter

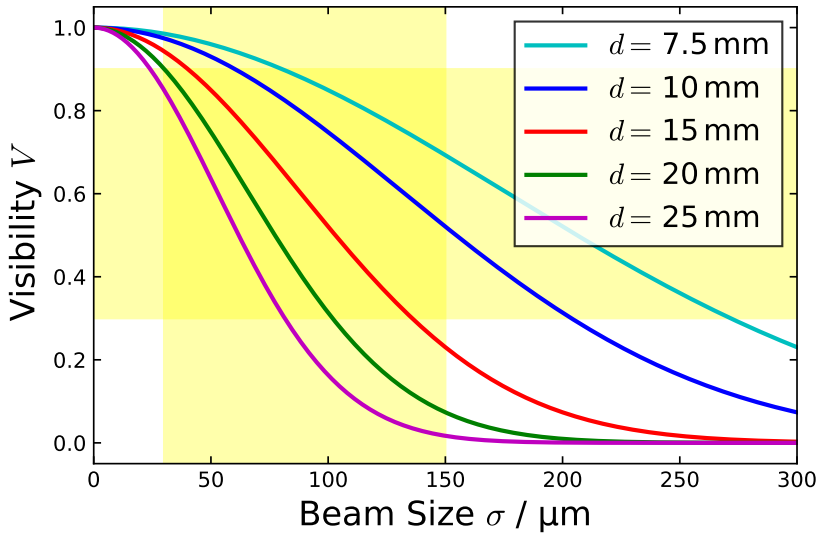

Figure 4.6.: Visibility as a function of the beam size for various slit separations at a wavelength of 550 nm for a distance to source of 15 m calculated with Eq. 3.39. The shaded area illustrates the region of the visibility to minimize the beam size error from Fig. 4.4 and the interesting region of beam sizes at BESSY II.

and is finally imaged onto the CCD camera. The single components are discussed in the following.

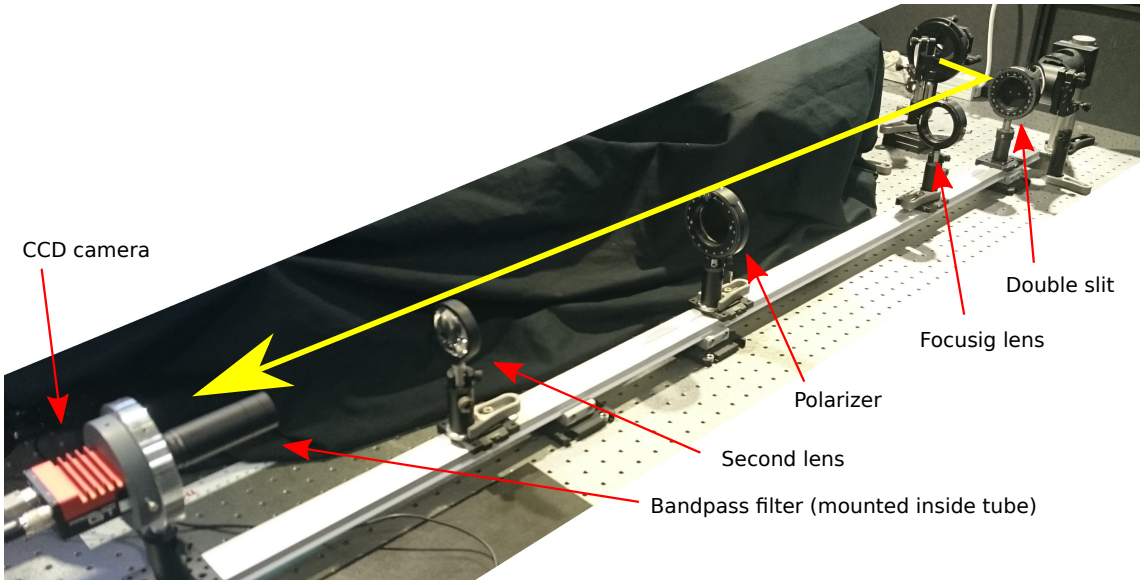

Figure 4.7.: Double slit interferometer setup at the BESSY II diagnostics beam line, including the double slit, the two lenses, the polarisation filter and the camera with a bandpass filter mounted inside the tube. The path of synchrotron radiation is shown by the yellow arrow.

Double Slits The double slits where printed with a 3D printer with an anti-reflection coating. Apertures made with the 3D printer are cheap and are also

available very fast, making this method ideal for testing purposes. Various slit separations from 7.5 mm to 25 mm with quadratic single holes of 3× 3 mm were produced. Those were either made in a quadratic form for a holder also printed with the 3D printer or in a round form with a diameter of two inch for regular optics mounts. An image of two double slits, one for the printed mount and one for a two inch optics mount, is shown in Fig. 4.8. Despite the quadratic form of the holes, they will be referred as slits in the following. The fabrication error of the printer is specified to be 0.1 mm, which was also the maximum deviation measured from the requested double slit separation.

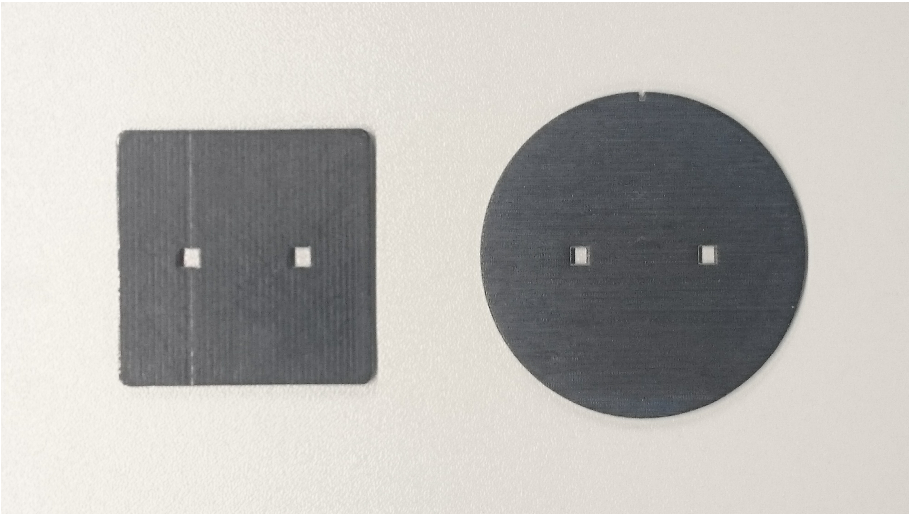

Figure 4.8.: Image of double slits printed with the 3D printer. The quadratic form (left) is for a horizontal aligned mount and the round form (right) can be mounted in a regular two inch optics mount.

Lenses For imaging of the interference pattern onto the camera a system of two lenses are used. One plano convex lens with a diameter of two inch and a focal length of about 1 m [29] is positioned as close as possible to the double slit to reduce the effect of an increased apparent double slit separation due to the synchrotron radiation opening angle. Since this lens is used for the measurement of the distance from the double slit to the source (see below) the focal length of the lens is calculated and shown as a function of the wavelength in Fig. 4.9. The focal length was also measured at a wavelength of 543 nm. The measured value of $f = 0.989 \pm 0.002$ m is about 4 mm smaller compared to the data from [30].

A second lens with a smaller focal length is used to enlarge the interference pattern on the camera chip. If not stated otherwise measurements are done with a magnification of 2.5 to 3. The focal length of the second lens is 5 cm, but the properties of this lens were not further analyzed, since it is only used for the enlargement of the interference pattern.

Polarisation Filter A thin film polarisation filter is used to separate σ-polarisation and π-polarisation. The polarizer has a transmission ratio of about 80 % for light aligned with the polarisation axis and an extinction ratio of 2000 for wavelengths between 400 nm and 750 nm [31].

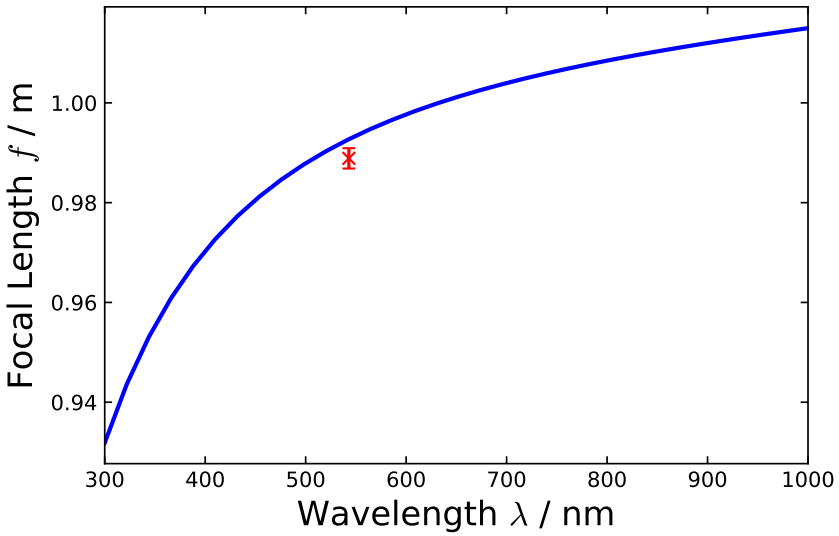

Figure 4.9.: Focal length of the focusing lens as a function of the wavelength (blue line) calculated with the refractive index [30] and the geometry of the lens [29]. In addition a measurement of the focal length at 543 nm is shown.

Bandpass Filter To get a quasi-monochromatic interference pattern hard coated bandpass filters are used [32]. The bandpass filters have a diameter of 25 mm and are positioned behind the second lens where light passes with small angle through the filter. For the interferometer the filters are mounted in a tube in front of the CCD camera, which simultaneously reduces the background light. The measured synchrotron spectrum passing through various bandpass filters is shown in Fig. 4.10. The respective spectra are each normalized to their maximum.

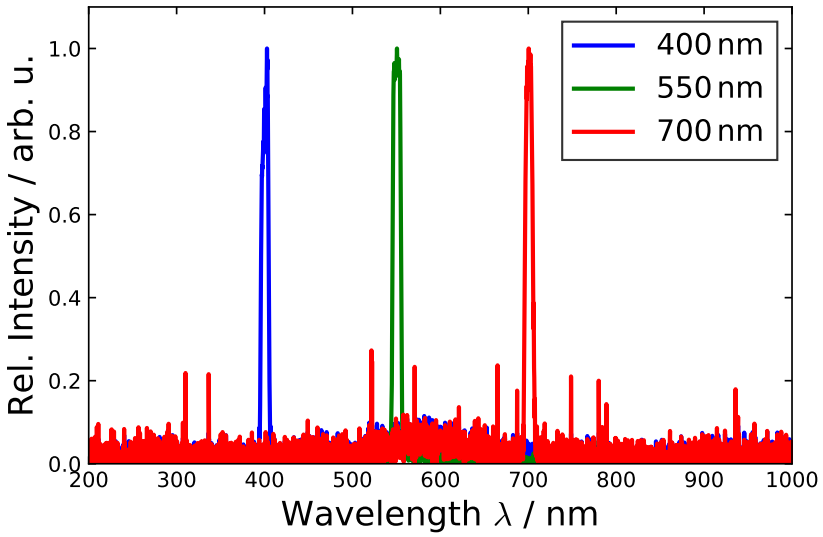

Figure 4.10.: Measured synchrotron spectra with bandpass filters at wavelengths of 400 nm, 550 nm and 700 nm with 10 nm bandwidth (FWHM). The spectra are normalized to their respective maximum.

The spectra were also fitted to obtain the central wavelength and the bandwidth of the filters. The maximum deviation found from the specified wavelength was 1.7 nm and the fitted bandwidths also matched the specified bandwidth of 10 nm (FWHM) with a maximum deviation of 0.9 nm. Note that this deviation might also be caused by the measurement with the spectrometer, since the measured intensity is a convolution of the transmission ratio and the synchrotron spectrum shown in Fig. 4.2.

Camera For the observation of the interference pattern the CCD camera Prosilica GT1920 from Allied Vision is used [33]. The chip has a resolution of 1936×1456 pixel with a pixel size of $4.54\,\mu m \times 4.54\,\mu m$. The camera integration time can be varied from 10 µs to over 20 s.

Distance to Source Point The distance of the position of the double slit to the source point was determined using the 1 m focal length lens. For different wavelengths the source point was imaged onto the camera and the distance from the focal plane to the camera chip was measured. Using only σ-polarized SR the measurements were done in standard user operation at 250 mA and repeated with low current of 1 mA. According to the lens formula

$$\frac{1}{f} = \frac{1}{b} + \frac{1}{g}, \tag{4.1}$$

where f is the focal length, g is the object distance and b the measured image distance, the distance of the double slit to the source can be obtained by the result for g, considering an additional offset for the slit position. The measurements were done separately for the horizontal and the vertical direction, since both planes could not be focused simultaneously. The results for the different storage ring currents and wavelengths are shown in Tab. 4.1.

Table 4.1.: Measured image distances for different storage ring current and wavelengths in the horizontal and vertical plane. The object distance is calculated with Eq. 4.1 and is the distance between the source point and the respective lens position.

Plane	**Current / mA**	λ **/ nm**	b **/ m**	g **/ m**
Hor.	1	400	1.0280 ± 0.0014	17.25 ± 0.90
Hor.	1	550	1.0570 ± 0.0014	16.50 ± 0.83
Hor.	1	800	1.0730 ± 0.0014	16.76 ± 0.83
Hor.	250	400	1.0320 ± 0.0014	16.20 ± 0.83
Hor.	250	550	1.0560 ± 0.0014	16.75 ± 0.84
Hor.	250	800	1.0730 ± 0.0014	16.76 ± 0.82
Ver.	1	400	1.0390 ± 0.0014	14.65 ± 0.74
Ver.	1	550	1.0645 ± 0.0014	14.87 ± 0.73
Ver.	1	800	1.0795 ± 0.0014	15.32 ± 0.74
Ver.	250	400	1.0410 ± 0.0014	14.27 ± 0.72
Ver.	250	550	1.0640 ± 0.0014	14.96 ± 0.74
Ver.	250	800	1.0840 ± 0.0014	14.47 ± 0.70

The distance of double slit could then be calculated considering an additional offset of the double slit to the respective lens position. For this measurements the camera was setup at a distance of 1.667 ± 0.005 m from the double slit position for regular beam size measurements. The results for the distance of the double slit to the source point for the horizontal and vertical direction are listed in Tab. 4.2.

Table 4.2.: Distance of the double slit to the source point obtained with the object distance of the measurements in Tab. 4.1 and considering an offset for the position of the double slit respective to the lens position.

	Distance to source / m
Horizontal	16.09 ± 0.84
Vertical	14.15 ± 0.73

The distance measured focusing the vertical plane is almost 2 m smaller than from the measurement in the horizontal plane. Also it is lower than the rough estimation for the minimum distance of 15 m, whereas the 16.09 m is reasonable considering the additional distance to the slit on the optic table. This effect is likely caused by a deformation of the extraction mirror due to the heat load from the high energy synchrotron radiation. This is also illustrated in Fig. 4.11 and the introduced angle leads to a smaller apparent distance to the source point. Therefore, for beam size measurement the value obtained in the horizontal plane is used. For the uncertainty of the distance to source, which is relatively high at about 5 %, the uncertainty of the image width measurement and the uncertainty from the measurement of the focal length of the lens (see above) are considered.

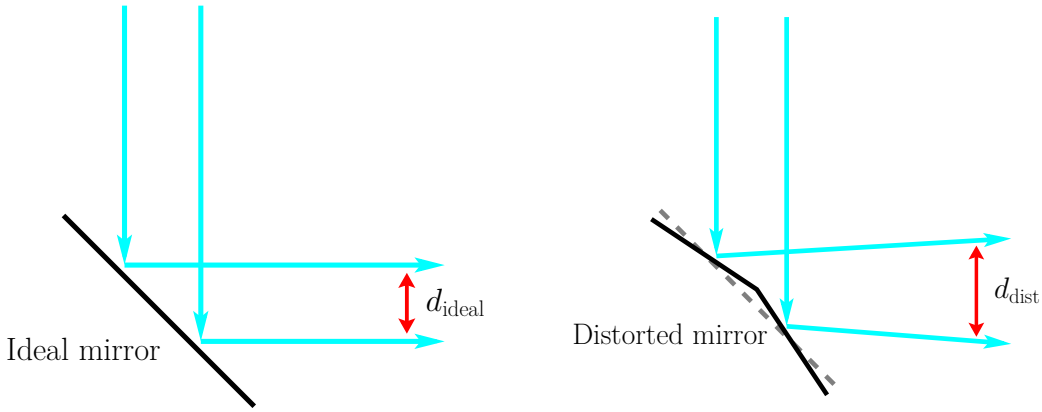

Figure 4.11.: Sketch of an ideal and a distorted plane mirror, where the deformation may be caused by heat load from high energy SR.

4.4. Data Analysis

The CCD camera is readout with a Labview program, which then provides access to the camera data via the BESSY II EPICS environment. A python tool is used to analyze the inference pattern and calculate the beam size.

4.4.1. Labview Tool and EPICS

The Labview camera interface which reads out the camera is the same as used for the pinhole systems, see Appendix A. A screen capture of the Labview tool showing the live camera image from the double slit interference of the synchrotron radiation can be seen in Fig. 4.12. The tool provides various possibilities to analyze and store the data and control the exposure time of the camera.

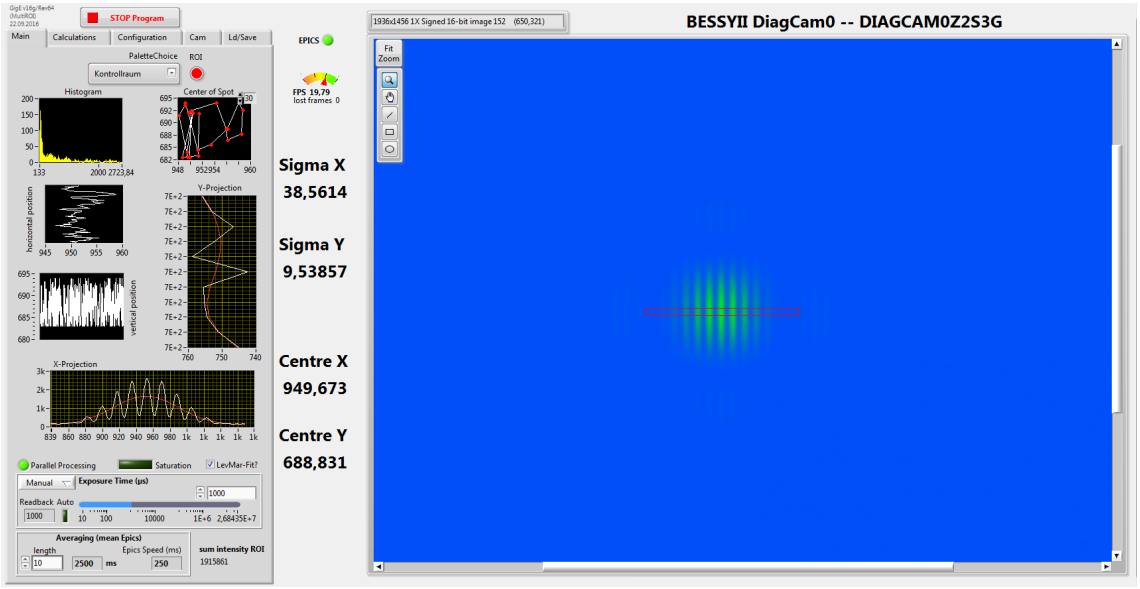

Figure 4.12.: Screen capture of the Labview tool for the CCD camera. On the left side are control and analysis panels and on the right is a live image from the camera. Inside the camera image the region of interest is included by the red rectangle.

BESSY II uses EPICS (Experimental Physics and Industrial Control System) to control the storage ring, and to transfer and archive data via process variables (PVs), which can be single data points or data arrays. The Labview tool is connected to multiple PVs allowing remote control over and readout of the analysis of the camera image. Most important for analyzing the interference pattern is the ability to set the camera exposure time and the region of interest (ROI) for which the analysis is performed. For further analysis of the interference pattern the projection of the data inside the ROI corresponding to the double slit orientation is used.

4.4.2. Python Tool for Online-Analysis

The python program analyses the projection of the interference pattern given by the Labview tool and does an online fit to provide the visibility and the beam size. A screen capture of the application is shown in Fig. 4.13. It shows an image from the camera, the interference fringe data from the region of interest with the fit, and has control panels for the fit and the important camera settings. The program is integrated in the BESSY II control system and can be used for transverse beam size measurements.

The camera image is shown again in Fig. 4.14. It also includes the ROI used for the measurement, which can be optimized on request (see also Section 4.5).

The live data from the intensity projection of the interference pattern corresponding to the double slit orientation is shown together with the fit in Fig. 4.15. The

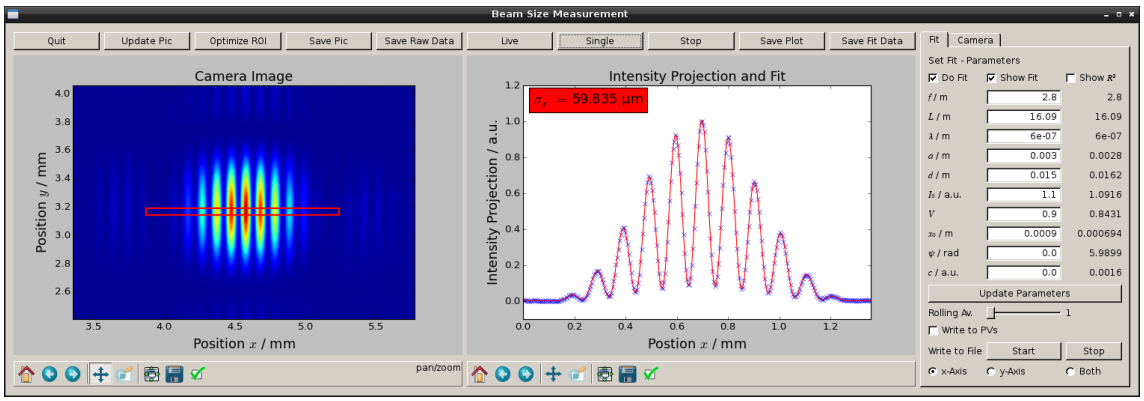

Figure 4.13.: Screen capture of the python tool for online analysis of the double slit interference pattern. The tool shows a camera image with the ROI (left), the live data of the intensity projection inside the ROI from the Labview tool with the fit (middle) and has panels to control the fit and camera settings (right).

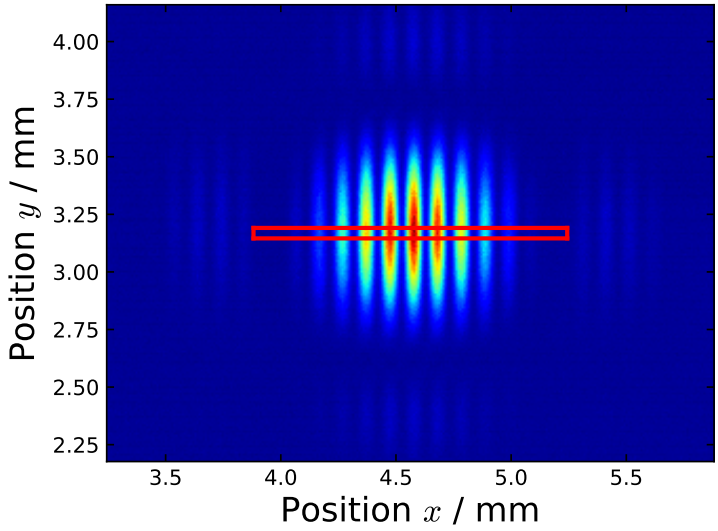

Figure 4.14.: Camera image zoomed onto the center of the interference pattern from a double slit separation of 15 mm, using a 600 nm bandpass filter. The ROI for the measurement is depicted by the red rectangle.

analysis can also be done for single measurements and the raw data as well as the camera image can be stored for single measurements.

The interference fringe data is fitted with the following function:

$$I(x) = a_0 \,\mathrm{sinc}^2\left[a_1(x - a_2)\right]\left[1 + a_3 \cos(a_4(x - a_2) + a_5)\right] + a_6. \tag{4.2}$$

Compared to Eq. 3.31 two additional free parameters are added, a_2 for the center of the interference pattern and a_6 for background intensity and camera noise. Further corresponds a_0 to $I_1 + I_2$, a_1 to $\pi a/f$, a_4 to $\pi d/f$, a_5 to ψ and a_3 is the visibility V. Before the fit the minimum from the projection data is subtracted from the whole data set and the data is then rescaled to a maximum of one. This allows a more stable fit, because a_1 and a_6 can now be estimated easier and are independent of the exposure time, background light and intensity changes.

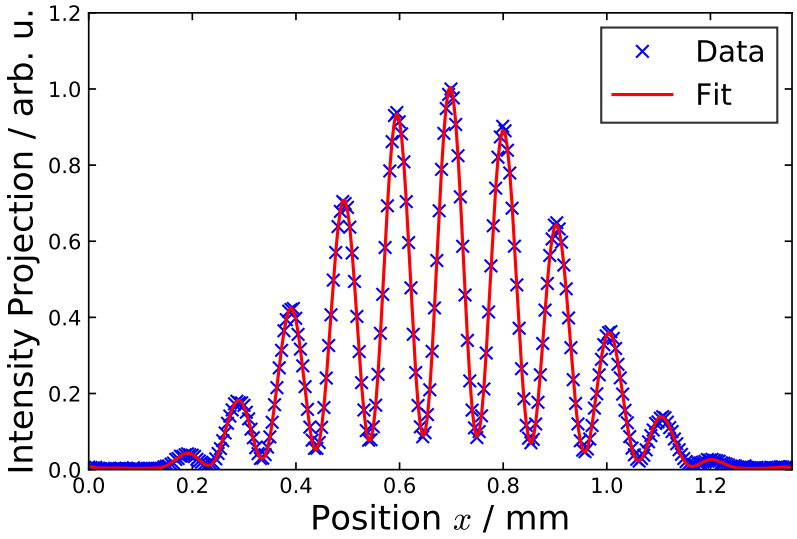

Figure 4.15.: Projected data of the double slit interference pattern from the ROI of Fig. 4.14 from a double slit separation of 15 mm, using a 600 nm bandpass filter. The data is fitted with Eq. 4.2.

The control panels for the data analysis can be seen in Fig. 4.16. In the fit panel the parameters are given for the initial fit estimation and for the variable parameters the fit results are shown. The distance between double slit and the source point, the double slit separation and the camera and the wavelength are not variable. The beam size is then calculated according to Eq. 3.41 and shown in the python tool. In addition several more options are given in the panel, e. g. averaging and storing the data, writing the fit results to PVs or set the orientation of the fit.

In the camera panel the important parameters to measure the intensity projection can be set. The exposure time can be set via the Labview tool and the width and center of the ROI in the Labview tool can be adjusted manually for both planes.

4.5. Resolution Limit and Error Estimation

4.5.1. Measurement Range and Statistical Error Contributions

Measurable Beam Size Range Considering the possible parameter combinations for the wavelength, the double slit separation and the visibility range given in Section 4.2 a range of beam sizes measurable with the present setup can be given. A maximal beam size which can be measured at a minimum visibility of 0.3, at a wavelength of 800 nm and a double slit separation of 7.5 mm would according to Eq. 3.41 be 424 µm. In contrast the minimum beam size at a visibility of 0.9 with a double slit separation of 25 mm at a wavelength of 400 nm is 18.8 µm.

Statistical Errors For the statistical error the measured uncertainties of the parameters used to calculate the beam size according to Eq. 3.41 are considered. This includes the contribution from the visibility, the distance of the double slit to the source point, the wavelength and the double slit separation. The relative error contributions of the single parameters to the beam size are listed in Tab. 4.3. The

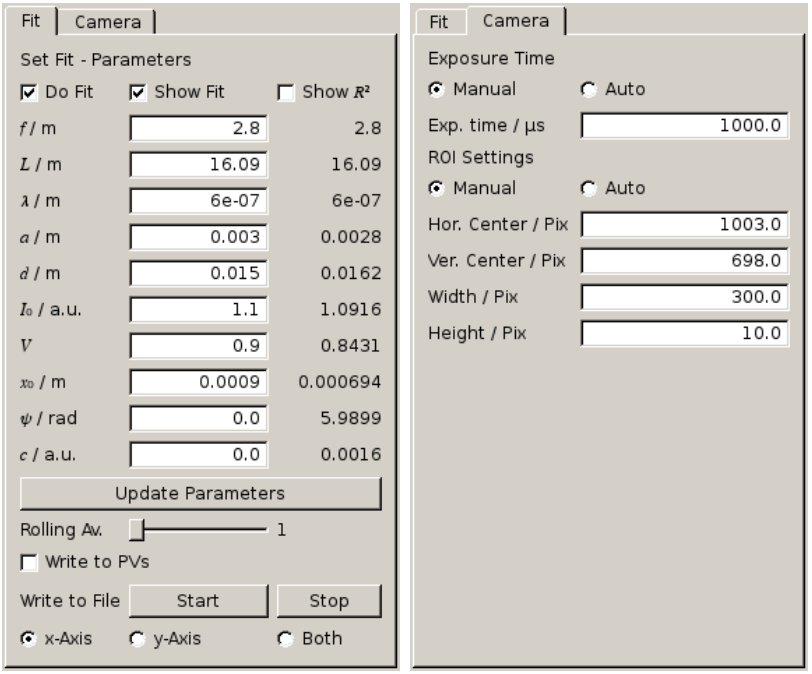

Figure 4.16.: Screen capture of the fit (left) and camera panel (right) of the python tool.

uncertainty of the measured visibility is exemplarily estimated with 0.005 and the impact on the beam size error is calculated for the maximum and minimum measurable beam sizes given before.

Table 4.3.: Relative impact of the uncertainties of the relevant parameters to calculate the beam size according to Eq. 3.41. The relative error contribution of the visibility uncertainty is given for the minimum and maximum measurable beam size.

Parameter	**Range**	**Uncertainty**	**Relative beam size error**
L / m	16.09	0.84	5.2 %
d / mm	$7.5 - 25$	0.1	$1.3 - 0.4$ %
λ / nm	$400 - 800$	1.6	$0.4 - 0.2$ %
$V(\sigma_{\min})$	0.3	0.005	0.7 %
$V(\sigma_{\max})$	0.9	0.005	2.6 %

With this the maximum and minimum measurable beam sizes are 424 ± 23 µm and 18.8 ± 1.1 µm. Thereby originates the largest contribution by far from the uncertainty of the distance of the double slit to the source point with over 5 %. Second is the contribution of the visibility, but only for an extreme case and the impact is generally lower. After that the uncertainty of the double slit separation follows and the impact of the uncertainty of the wavelength is vanishing compared to the other contributions.

4.5.2. Systematic Error Contributions

The objective of this section is to discuss effects which might possibly introduce a systematic change in the measured visibility and estimate their impact. This

mainly covers parts of the interferometer setup, including the beam line, but also some aspects concerning the theory introduced in Chapter 3.

Bandpass Filter Bandwidth The effect of the filter bandwidth was tested with bandpass filters with various filter bandwidths at central wavelength of 550 nm. The SR spectra of the bandpass filter with bandwidths of 10 nm, 25 nm and 50 nm were measured with the compact CCD spectrometer and are shown in Fig. 4.17.

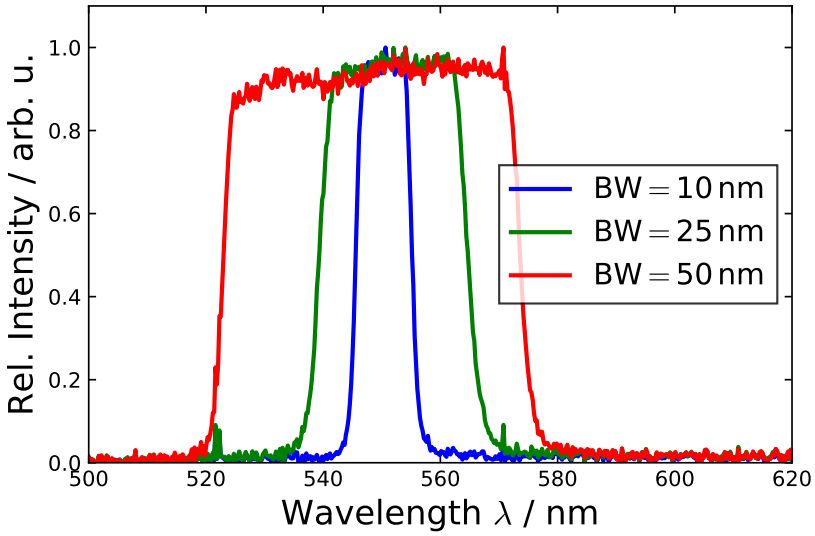

Figure 4.17.: Measured synchrotron spectra with bandpass filters at a central wavelength of 550 nm with bandwidths of 10 nm, 25 nm and 50 nm (FWHM). The spectra are normalized to their respective maximum.

The visibility was measured with those three bandpass filters in standard user operation at a current of 250 mA and with a double slit separation of 15 mm. The measurement of the visibility as a function of the filter bandwidth is shown in Fig. 4.18. Compared to the 10 nm filter bandwidth, the visibility decreases slightly for the 25 nm filter bandwidth by about 0.005 and significantly for a filter bandwidth of 50 nm by about 0.025. Note that this result might not only be an effect of the impact of the wavelength on the interference pattern. Additionally a chromatic aberration of the focusing lens could have an impact on the measurement.

Measurements with the interferometric beam size monitor are therefore always made with the smallest filter bandwidth of 10 nm. Smaller filter bandwidths were not tested, but it has to be considered that further reducing the bandwidth makes it necessary to increase the camera integration time to retain a similar photon flux (see below). To estimate the effect of a 10 nm filter bandwidth a double slit interference pattern at visibility $V = 1$ is shown for a wavelength of 550 nm and for wavelengths of (550 ± 5) nm for a double slit with slit separation of 15 mm and a single slit width of 3 mm at a distance from the double slit to the camera of 1 m in Fig. 4.19.

In the interference pattern a small difference can be seen near the minima from the single slit envelope. A possible correction of this effect would be, to fit the interference pattern integrated over the transmitted wavelengths, weighted with the intensity at that wavelength. However this does not seem necessary for a 10 nm bandwidth.

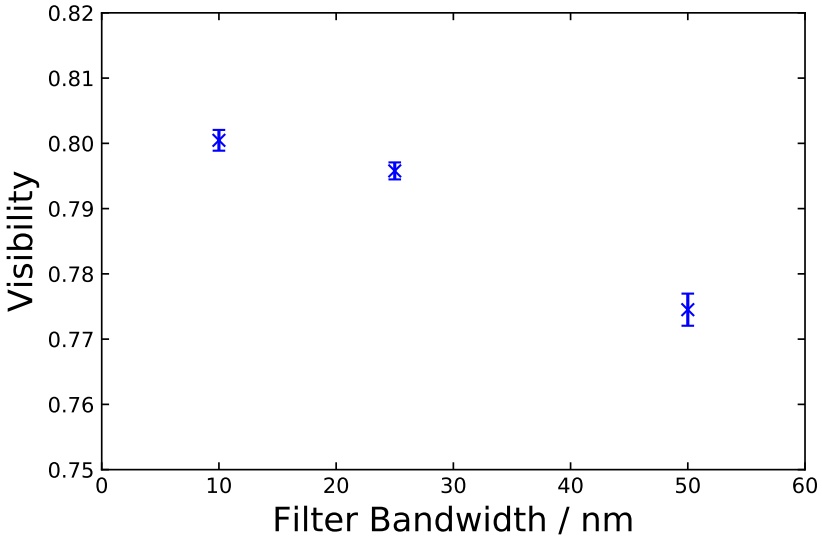

Figure 4.18.: Measured visibility for bandpass filters at a wavelength of 550 nm with different bandwidths in standard user operation. The double slit separation was 15 mm and the filter bandwidth is given in FWHM.

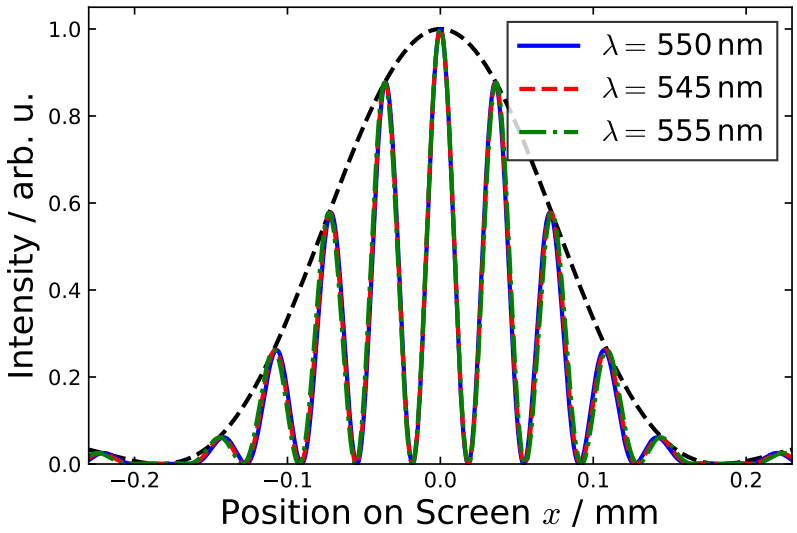

Figure 4.19.: Double slit interference pattern for a central wavelength of 550 nm and for wavelengths at 550±5 nm. The double slit separation is set to 15 mm, the single slit width to 3 mm and the distance from the double slit to the camera to 1 m. In addition the single slit envelope is plotted for 550 nm (dashed blue line).

Single Slit Width and Height From the theory in Chapter 3 and the derivation of Eq. 3.31 in Appendix B the single slit width has no impact on the visibility, if the single slit width is small compared to the double slit separation. However, the single slit width indirectly has an effect on some other parameters. One aspect is that a larger single slit width results in a more compact interference pattern which needs to be measured, since the interference pattern beyond the first minima of the

single slit envelope are not used for the analysis and thus reduces the effect of the bandpass filter width as discussed above or chromatic aberration from the lens (see below). In addition a larger slit width means higher light intensity, which enables a lower camera integration time. In contrast a smaller single slit width reduces any intensity changes or wavefront errors over a single slit.

The slit height has no impact on the normalized interference pattern, but the same argument concerning focusing, intensity changes and wavefront errors as discussed for the slit width applies. Therefore the slit height was chosen to be equal to the single slit width. The effect of the slit width and slit height were not further investigated, since the 3D printer could not print sufficient slits for slit widths of 1 mm and a slit width of 3 mm seems already large compared to double slit separations down to 7.5 mm.

Camera Integration Time and ROI The impact of the CCD camera settings were tested in standard user operation with 250 mA. A double slit with a double slit separation of 15 mm and a bandpass filter for a wavelength of 550 nm were used and the measurement was done in the horizontal plane. At first the visibility was measured varying the width and the height of the region of interest (ROI). This measurements were done with σ-polarisation and each for different camera exposure times of 0.5 ms and 5 ms. The ROI height defines the number of pixels, over which the intensity projection is averaged, whereas the ROI width defines the width of the projection, see for example Fig. 4.15.

The ROI height was varied from 1 to 150 pixel while the ROI width was set to 325 pixel. The measured visibility is shown as a function of the ROI height in Fig. 4.20. The visibility changes only little with the ROI height and no tendency is registered. It is noticeable that the fluctuation of the visibility is sometimes larger for higher integration times, which might be caused by vibrations. In general the ROI height does not seem to have a large impact on the visibility measurement and the magnification of the interference pattern with the second lens enhances this. For beam size measurement it was chosen to set the ROI height to 10 pixel, to minimize the effect of a larger ROI on more unstable setups where the interference pattern cannot be focused perfectly, e. g. see Section 5.5.

The ROI width was varied between 200 and 800 pixel and the measured visibility as a function of the ROI width is shown in Fig. 4.21. The center of the ROI was set to the center of the interference pattern and the ROI height was set to 10 pixel. In this setup a minimum width of over 200 pixel was needed to obtain a reasonable fit result. A proper visibility can only be measured if at least the first minimum of the envelope from the single slit interference is included, which in this case was satisfied for ROI width larger than approximately 280 pixel. For ROI widths larger than 340 pixel the visibility decreases slightly and remains nearly constant for a ROI width of more than 400 pixel. The decrease is caused by including the next maximum of the envelope from the single slit interference, which might not be focused properly due to lens aberrations. For beam size measurements the ROI width is therefore chosen depending on the setup and is set to a width somewhat larger than the first minimum of the envelope from the single slit interference, an example of this is shown in Fig. 4.15.

The effect of the exposure time was tested for a high intensity for which σ-polarisation was used and for lower intensity for which π-polarisation was used. The exposure time was varied from 50 µs where the first measurement was possible

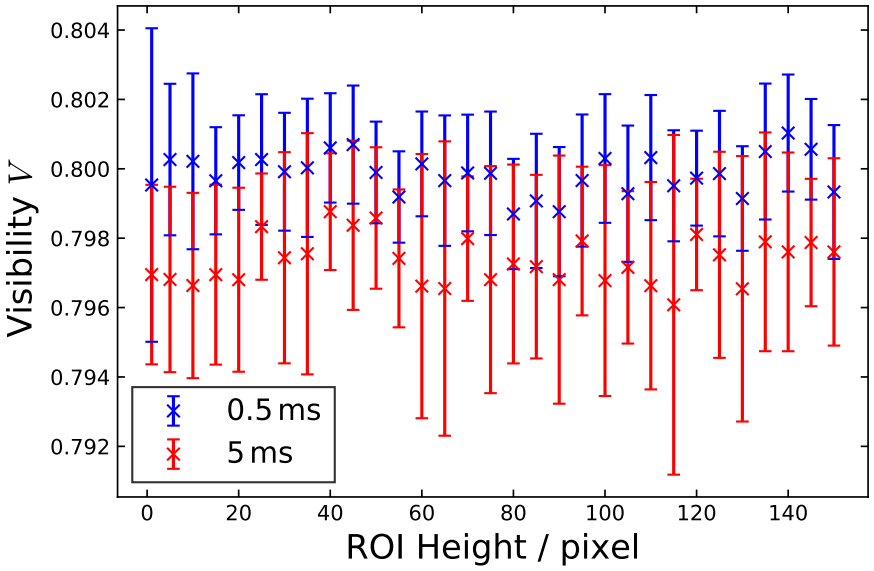

Figure 4.20.: Measured visibility as a function of the height of the ROI shown in Fig. 4.14 for different camera exposure times. The measurement was done with a double slit separation of 15 mm and a wavelength filter at 550 nm in standard user operation at 250 mA.

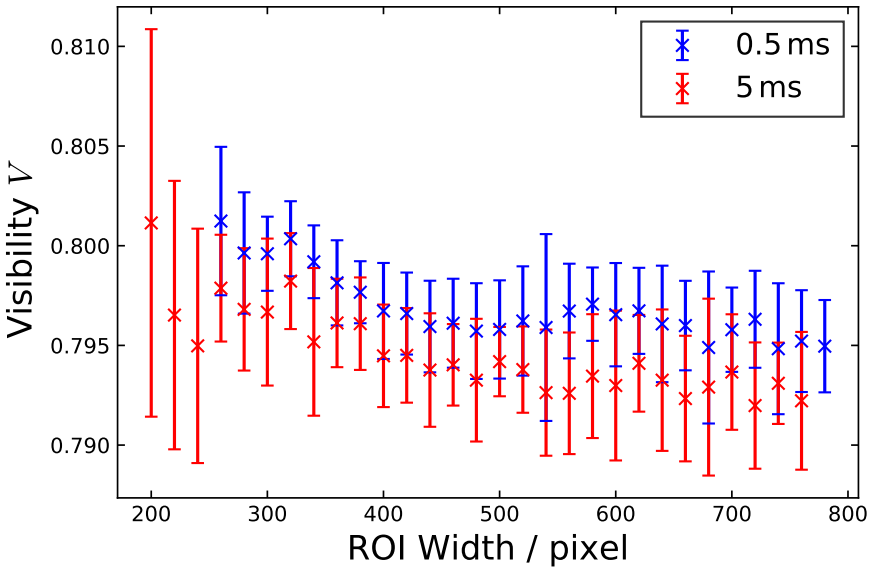

Figure 4.21.: Measured visibility as a function of the width of the ROI shown in Fig. 4.14 for different camera exposure times. The measurement was done with a double slit separation of 15 mm and a wavelength filter at 550 nm in standard user operation at 250 mA.

up to where the saturation limit of the camera was reached. The measured visibility as a function of the exposure time is shown in Fig. 4.22. In both cases the visibility has a large error for low integration times and increases to a maximum at about 0.5 ms and 2 ms respectively. This caused by insufficient light intensity for a proper fit at lower exposure times. Towards higher exposure times the visibility decreases slightly, which is likely caused by vibrations of the photon beam introduced by a

beamline component until the saturation limit is reached at 8 ms and 30 ms, respectively. For beam size measurement the exposure time is generally set to a few ms, except for conditions where the light intensity is too low, e. g. in low-α or single bunch operation. As already discussed above the camera exposure time is connected to the bandwidth of the filter and the single slit dimension. Those three parameters have to be considered simultaneously, however changing the camera exposure time is the simplest way to control the intensity. Note that the difference between the two measurements is likely caused by a significant intensity imbalance for the higher intensity at σ-polarisation.

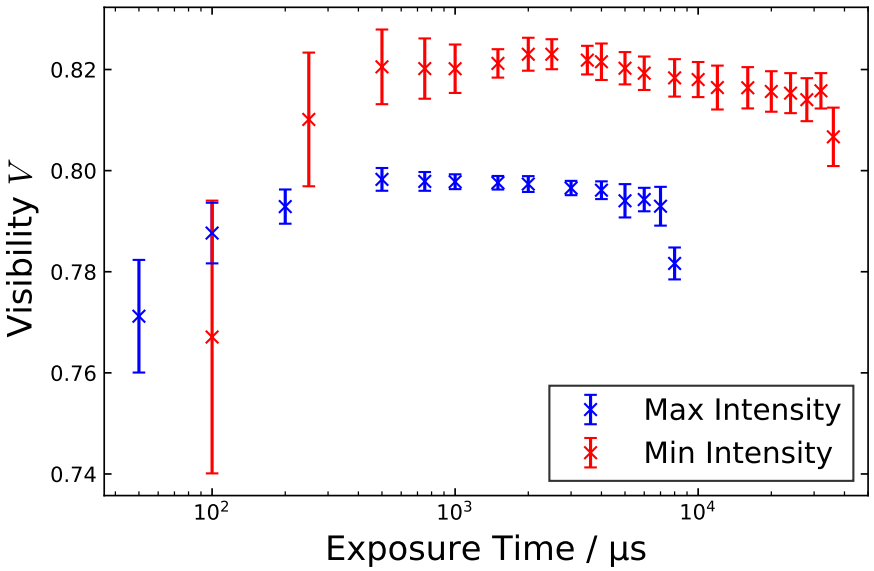

Figure 4.22.: Measured visibility as a function of the camera exposure time for high intensity (σ-polarisation) and low intensity (π-polarisation). The measurement was done with a double slit separation of 15 mm and a wavelength filter of 550 nm in standard user operation at 250 mA.

Camera Noise The effect of the camera noise was evaluated by plotting the intensity of a pixel row perpendicular to the direction of the double slit interference pattern. For this the image taken with an exposure time of 1 ms from Fig. 4.14 was used and a pixel row in the maximum and a pixel row near the first local minimum of the interference pattern were chosen. The two pixel rows are also illustrated in Fig. 4.23.

The intensity along the two pixel rows is shown in Fig. 4.24. Both intensities have the form of a single slit interference and both curves are shifted up by a constant term caused by the camera noise. This effect is considered in the data analysis by adding a constant term in the fit and is furthermore minimized by using a projection width over several pixel. Therefore the impact of the camera noise is neglected for a reasonable aligned setup.

Incoherence Depth of Field Effect The incoherence depth of field is introduced in Eq. 3.29 to correct the visibility in the plane of the synchrotron radiation, i. e. the horizontal plane [25]. A simulation of this effect as a function of the beam size is shown in Fig. 4.25 for the BESSY II bending radius of 4.35 m and electron energy

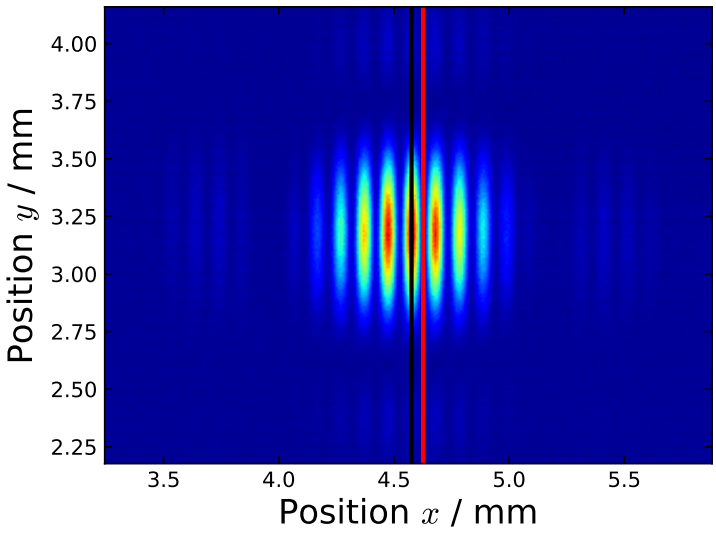

Figure 4.23.: Camera image zoomed onto the center of an interference pattern from a double slit separation of 15 mm and a 600 nm bandpass filter. The maximum (black line) and next local minimum (red line) pixel rows perpendicular to the double slit orientation are shown.

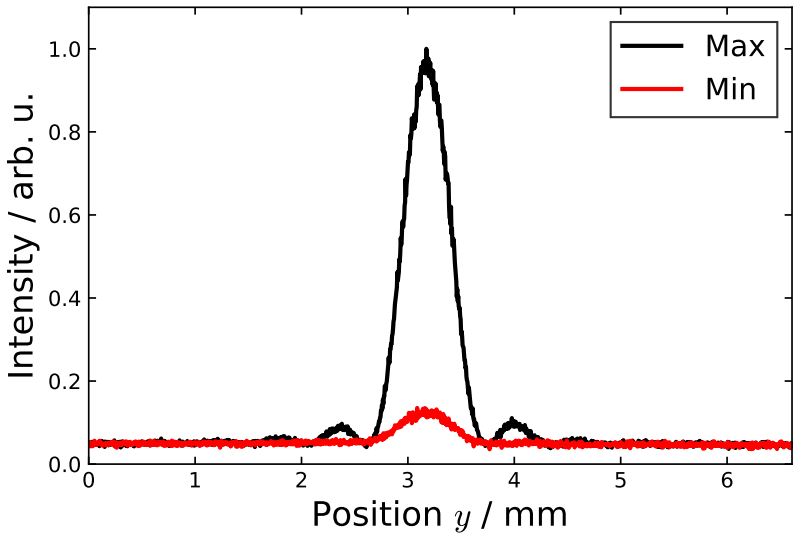

Figure 4.24.: Intensity profile of the maximum and next local minimum pixel rows perpendicular to the double slit orientation of the double slit interference pattern from Fig. 4.23.

of 1.7 GeV, assuming a double slit separation of 15 mm and a distance of the double slit to the source of 16.1 m at a wavelength of 400 nm.

Compared to the visibility obtained with Eq. 3.39 the incoherent depth of field effect causes a decrease of the visibility. The effect is especially significant for smaller beam sizes leading to a maximum visibility of about 0.95 for a hypothetical vanishing beam size. This is important to note, considering the discussion in Section 4.2. In the horizontal case the maximum visibility for the same beam size error shifts by

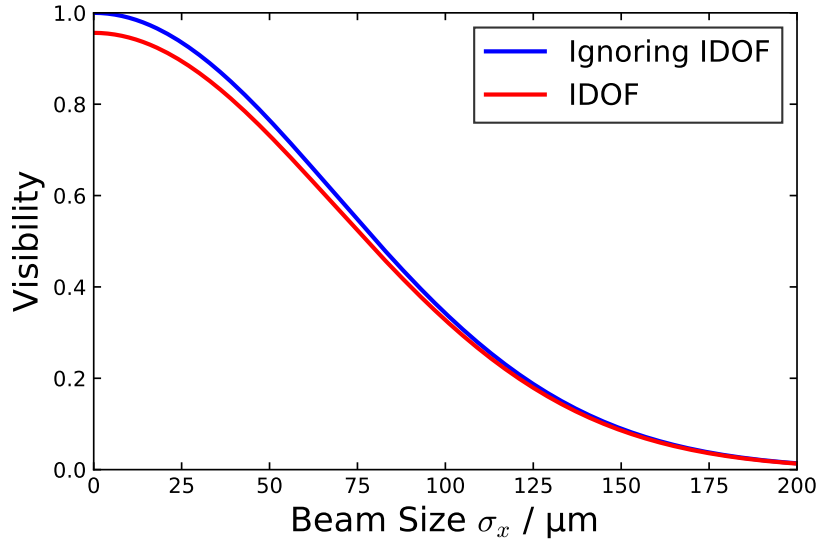

Figure 4.25.: Visibility as a function of the beam size neglecting and considering the incoherent depth of field effect from Eq. 3.29 for a double slit separation of 15 mm, a distance to the source of 16.1 m and a wavelength of 400 nm.

about 0.05 further down, so that measured visibilities should be at least below 0.9. A simulation of the incoherence depth of field effect on the measured beam size as a function of the given beam size is also shown in Fig. 4.26 for the same parameters as in Fig. 4.25.

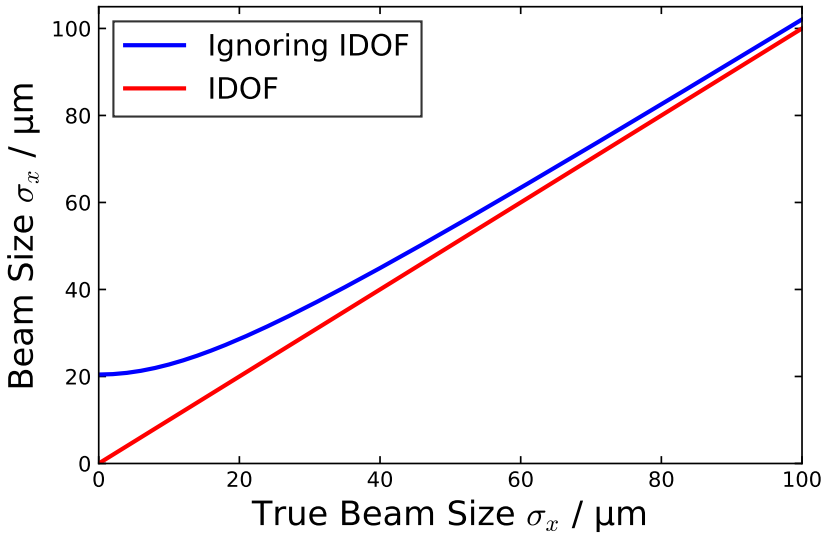

Figure 4.26.: Beam size as a function of the beam size neglecting and considering coherent depth of field effect from Eq. 3.29 for a double slit separation of 15 mm, a distance to the source of 16.1 m and a wavelength of 400 nm.

If the effect would not be considered, the beam size calculated with Eq. 3.41 will appear to be resolution limited, resulting in a measured beam size of about 20 µm for

a hypothetical vanishing beam size. For larger beam sizes the deviation gets smaller and asymptotical converges to the given beam size. If not stated otherwise the incoherent depth of field effect will be corrected for measurements of the horizontal beam size.

Lens Dispersion A simple lens has a chromatic and a spherical aberration effect. The chromatic aberration is caused by the wavelength dependent focal length, which is shown for the plano convex lens with a focal length of about 1 m in Fig. 4.9. As discussed for the filter bandwidth this effect might be significant for larger bandwidths, but for a 10 nm bandwidth and for a large single slit width this effect can be neglected. The effect of the spherical aberration was not evaluated, but it was tried to minimize this effect by aligning the center of the lens with the center of the double slit.

Wavefront Distortion The wavefront of the illuminated area was not characterized, but a distortion was observed measuring the distance to the source point. In addition the position of the focusing lens has to be realigned when changing from measuring horizontal to vertical beam sizes. For calculations of the beam sizes in both orientations the value obtained in the horizontal direction is used, but the wavefront distortion is likely causing a systematic error especially for vertical beam sizes.

Intensity Imbalance and Uniform Slit Illumination As introduced in Section 3.2 an intensity imbalance between the respective single slits decreases the visibility. This was taken into account and measurements were only done if the ratio between the sum intensities of the two single slit was above 0.8, which according Fig. 3.3 leads to a negligible change in the visibility. This was ensured by comparing the intensities separately covering the respective other slit. Large intensity changes at a single slit were not observed and are not considered to have an impact on the measurement.

Slit Position The slit position relative to the center of the synchrotron beam is not known as discussed in Section 4.1. The position was often used as a free parameter to fulfill the intensity imbalance condition especially for measurement of the vertical beam size. However, no systematical tests were made, since intensity imbalances and wavefront distortions caused by the extraction mirror are too high to resolve the impact of the slit position.

Orbit Jitter A movement of the electron beam at the source point on timescales smaller than the camera exposure time will reduce the measured visibility and thus the measured beam size is a result of the superposition of the orbit jitter and the source distribution. The orbit jitter is monitored using beam position monitors and is in the order of 5 µm. To get an estimation for the source point of the interferometer this value has to be rescaled with the ratio of the β-functions from where the beam motion is measured and from the source point of the interferometer.

Vibrations and Air Disturbance The same discussion as for the orbit jitter applies if not the electron beam itself but a component of the beam line introduces a jitter

on the photon beam. Similar to orbit jitter any movement of the synchrotron ray caused for example by vibrations of mirrors or other beam line components leads to a decrease in the measured visibility. Another small impact on the measurement is expected due to air disturbances since the beamline is uncovered.

Summary Overall the effects of the filter bandwidth and the camera noise are neglected and the intensity imbalance of the two single slits and the depth of field effect in horizontal orientation are corrected. Furthermore the camera settings, including the ROI and the exposure time were optimized and are assumed to be small, but further studies are recommended to analyze the impact on the visibility. However this is only expected to have a minor impact on the visibility. The impact of the single slit width, the intensity variation at a single slit and the lens aberration were not investigated, but should also only have a minor effect for a well aligned setup. Very important is it however to consider that possible wavefront distortions and jitter effects are not corrected prior to any measurements and are part of the discussion of the measurement results in the following chapter.

5. Experimental Results

A preliminary setup of the double slit interferometer at the BESSY II storage ring has been commissioned. Multiple measurement series varying the spatial frequency, see Eq. 3.22, or the beam size in both planes are made and, if possible, compared with measurements from the pinhole system and the lattice models. Moreover some two dimensional applications of the system are shown.

5.1. Spatial Frequency Scans

As introduced in Section 3.3 the one dimensional beam profile can be obtained by varying the spatial frequency $\nu_{x,y}$ from Eq. 3.22 and fitting the visibility. There are three independent parameters to vary the spatial frequency: The slit separation d, the distance between the double slit and the source point L and the wavelength λ.

Measurements series were done for various slit separations from 7.5 mm to 25 mm and with various bandpass filters at wavelengths from 400 nm to 800 nm. The beam size was then obtained from fitting the measured visibility $V(d, \lambda)$ with Eq. 3.39 and also compared to the beam sizes for each single visibility measurement calculated with Eq. 3.41. Since the distance to the source of approximately 16 m could only be increased by about 1 m within one straight on the table, the spatial frequency and therefore the visibility could not be changed enough to provide a significant measurement series. Those frequency scans were also performed separately for different polarisations, orientations and storage ring conditions. The polarisation was set to σ and π-polarisation for horizontal and vertical visibility measurements. All measurements were made for standard user and low-α operation with high current and two additional measurement series were made in low-α operation with low current.

The measurements in standard user mode were done at a total beam current of 250 mA in top up operation. For all measurements varying the slit separation the 400 nm bandpass filter was used and for all measurements changing the wavelength the double slit with a slit separation of 20 mm was used. The camera exposure time was always set to 1 ms, except for higher wavelengths and π-polarisation it was increased up to 10 ms due to insufficient light intensity. The measured visibilities and beam sizes for the double slit separation and wavelength scans are shown in Fig. 5.1 and in Fig. 5.2 respectively and the fit results can be found in Tab. 5.1. The uncertainties given for the fit results do include the statistical errors discussed in Section 4.5 and the error bars in the plots only show the statistical errors from the measurement.

From the measurements changing the slit separation the single measurements and the fitted beam sizes agree and the resulting beam sizes from the fits are about 54 µm in the horizontal and 50 µm in the vertical direction. Those also agree with the beam sizes obtained from the measurements for a single configuration, except for the value obtained with a slit separation of 7.5 mm, which is significantly higher in all measurement series. Though already the 400 nm bandpass filter was chosen to decrease the visibility, the minimum visibility measured with a double slit separa-

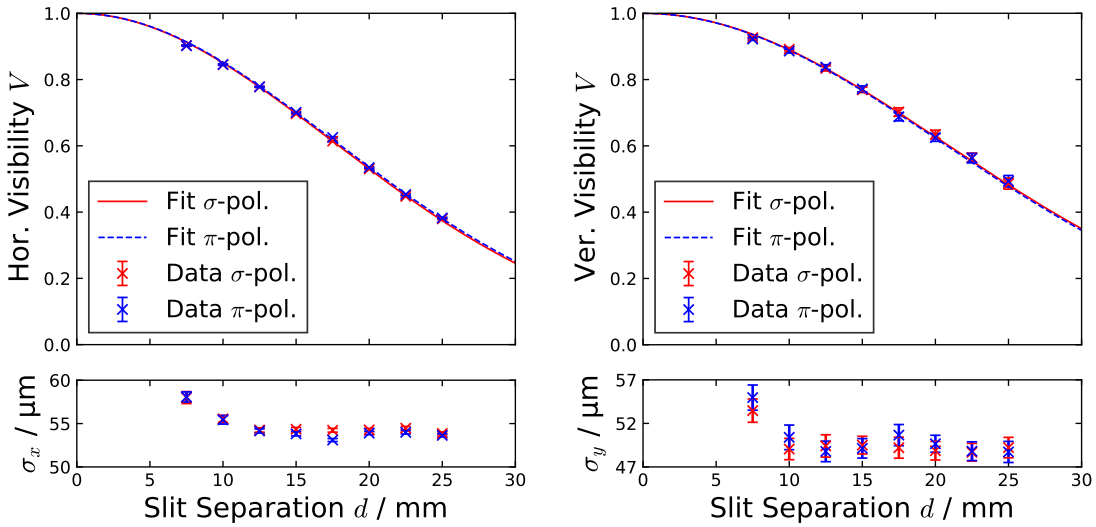

Figure 5.1.: Measured visibility and calculated beam size as a function of the slit separation for σ and π-polarisation in the horizontal (left) and vertical (right) plane in standard user mode at a wavelength of 400 nm. The lines show the fits according to Eq. 3.29 in the horizontal and to Eq. 3.39 in the vertical case, respectively.

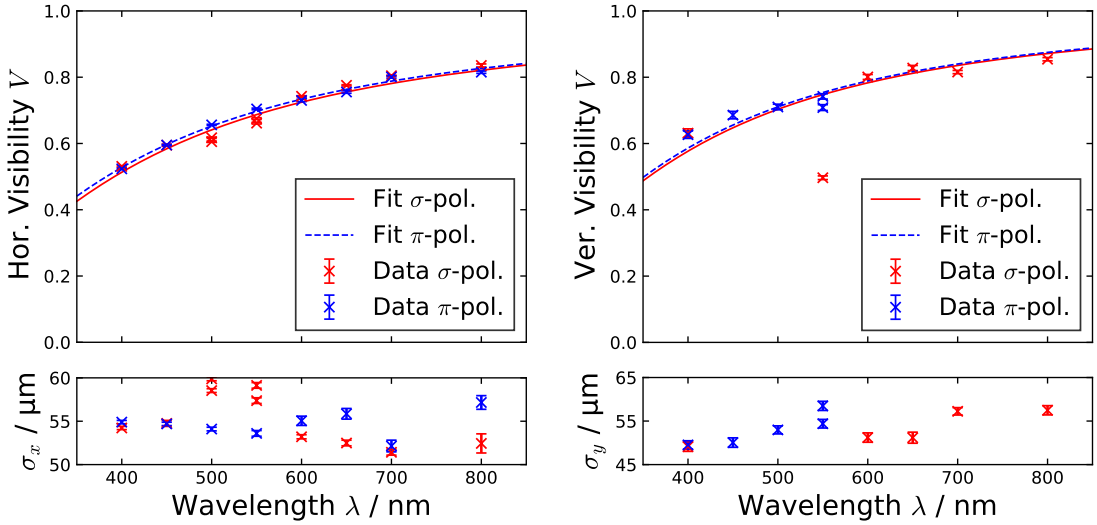

Figure 5.2.: Measured visibility and calculated beam size as a function of the wavelength for σ and π-polarisation in the horizontal (left) and vertical (right) plane in standard user mode at a double slit separation of 20 mm. The lines show the fits according to Eq. 3.29 in the horizontal and to Eq. 3.39 in the vertical case, respectively.

tion of 25 mm was still about 0.4 in the horizontal and 0.5 in the vertical direction, respectively, while the maximum visibility was about 0.9 in both cases. Covering a wider visibility range is not possible, since larger slit separations are not feasible, due to the limitations by the beam line.

For the wavelength scans is was more difficult to setup the system for some parameter combinations due to intensity imbalances at the two slits. For some wavelengths this could not be corrected by changing the slit position, especially in the vertical

direction, where only at 400 nm the visibility could be measured and was in the expected range for both polarisations. An example for this is can be seen in the measurement for the vertical direction at a wavelength of 550 nm for σ-polarisation in Fig. 5.2, which is not considered for the fit. Although extensive effort was put into the alignment of the system and only doing measurements were the intensity ratio between the two slits was acceptable, the results from the wavelength scans have a larger error than the results for the slit separation scans. Moreover the beam sizes from the visibilities measured at different wavelengths are fluctuating up to 10 µm. The results for the fitted beam sizes are a few µm larger for all measurement series and the uncertainties are also larger. The visibility range covered with this scan is smaller than for the slit separation scan, since the wavelength range for visible light is limited and already a large slit separation of 20 mm was used for the wavelength scans.

In low-α operation all eight measurement series were repeated. The measurements were done with decaying beam, but the total beam current was always between 100 mA and 90 mA to minimize any current depending changes of the beam size. The slit separation scans were done at a wavelength of 700 nm for σ-polarisation and at 450 nm for π-polarisation. The wavelength scans were all done using the double slit with 12.5 mm double slit separation. The exposure time was set to 2 ms due to less light at low-α and for wider slit separations or higher wavelengths, especially for π-polarisation it had to be increased up to 20 ms. The measurements varying the slit separation and the wavelength are shown in Fig. 5.3 and Fig. 5.4 and the fit results are listed in Tab. 5.1.

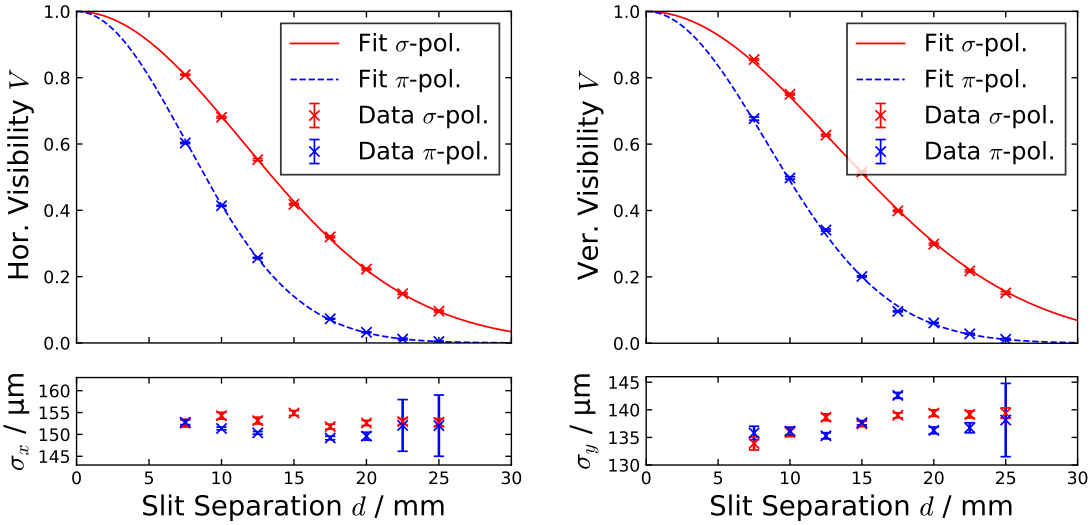

Figure 5.3.: Measured visibility and calculated beam size as a function of the double slit separation for σ and π-polarisation in the horizontal (left) and vertical (right) plane in low-α mode above bursting threshold. The measurement was done at a wavelength of 700 nm for σ-polarisation and at 450 nm for π-polarisation. The lines show the fits according to Eq. 3.29 in the horizontal and to Eq. 3.39 in the vertical case, respectively.

The fit results provide beam sizes somewhat larger than 150 µm in the horizontal and around 140 µm in the vertical direction. For the slit separation measurements with π-polarisation for large slit separation the visibility was close to 0, which leads

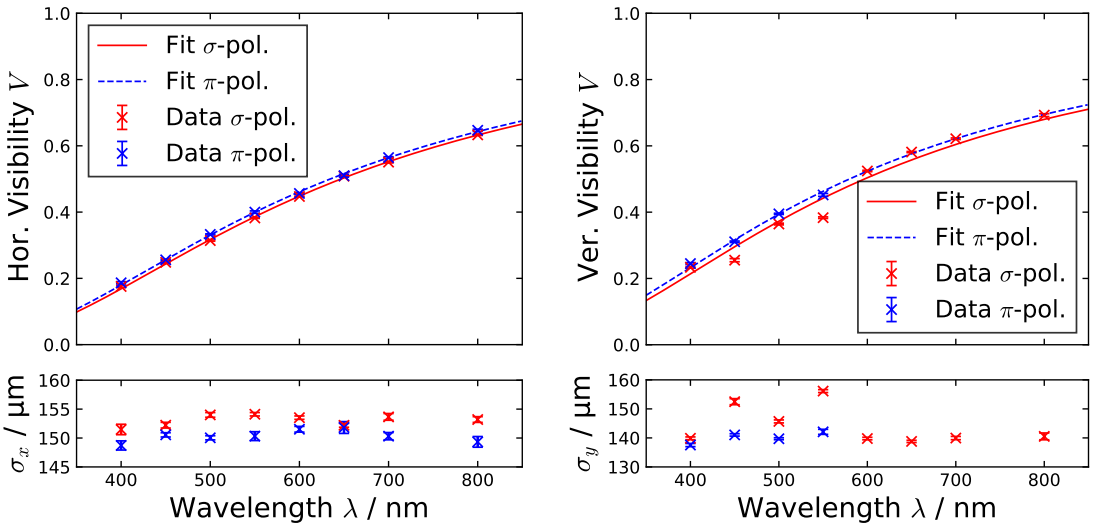

Figure 5.4.: Measured visibility and calculated beam size as a function of the wavelength for σ and π-polarisation in the horizontal (left) and vertical (right) plane in low-α mode above bursting threshold with a double slit separation of 12.5 mm. The lines show the fits according to Eq. 3.29 in the horizontal and to Eq. 3.39 in the vertical case, respectively.

to large errors for the beam sizes calculated from that visibility. The vertical measurement was not possible for wavelengths exceeding 550 nm with π-polarisation and difficult for lower wavelengths with σ-polarisation due to intensity imbalances. This was also the reason, why a lower wavelength for the slit separation scans with π-polarisation was chosen. The results with π-polarisation are all slightly lower than with σ-polarisation but within the uncertainties. This can also be observed from the beam sizes calculated from the single measurements, which also fluctuate much more than the slit separation scans in standard user mode. But in general the results from both methods show good agreement in the low-α mode.

To get some more insight on the effect of high beam current on the transverse beam size in low-α, slit separation scans with σ-polarisation were done for horizontal and vertical direction at a current below the bursting threshold of approximately 14.5 mA at a wavelength of 600 nm. The measurements are also done in decay mode, but at a lifetime of about 50 h the beam current did not change significantly during this measurements. The camera exposure time was set to 20 ms for both measurement series. The measured visibilities and beam sizes are shown in Fig. 5.5 and the fit results can also be found in Tab. 5.1.

The beam sizes obtained from the fits in low current operation are about 10 µm smaller in the horizontal and about 15 µm smaller in the vertical direction. This is generally expected due to bursting and coupling effects. The measurement errors for the single measurements are higher in the vertical direction, but in general both seem more stable than for the high current measurements.

Pinhole Measurements During the measurements in standard user mode the measurements of the two pinholes were recorded. For the comparison the average values are taken during the interferometer measurements. For low-α mode the pinhole values are taken from measurements at the beginning of the low-α week. For both pinhole systems the beam sizes were measured at 100 mA and at 15 mA once with

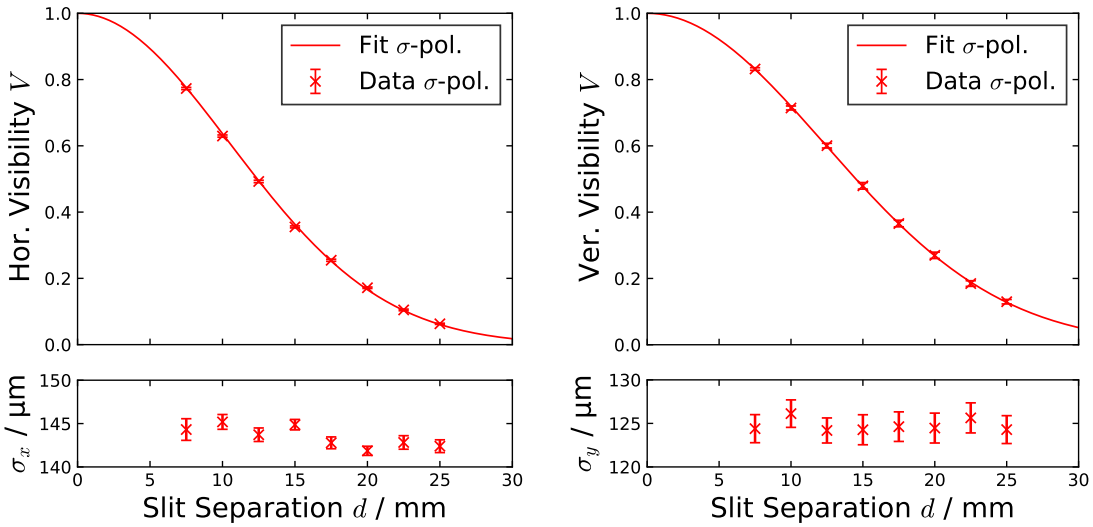

Figure 5.5.: Measured visibility and calculated beam size as a function of the slit separation for σ-polarisation in the horizontal (left) and vertical (right) plane in low-α mode below bursting threshold at a wavelength of 600 nm. The lines show the fits according to Eq. 3.29 in the horizontal and to Eq. 3.39 in the vertical case, respectively.

Table 5.1.: Measured beam sizes with the frequency scans for different storage ring conditions. The beam sizes are obtained by fitting the measured visibilities shown in Figs. 5.1 to 5.5.

Storage ring	Plane	Param.	Polarisation	Beam size / µm
Std. user, 250 mA, top up	Hor.	d	σ	54.3 ± 2.9
Std. user, 250 mA, top up	Hor.	d	π	53.8 ± 2.8
Std. user, 250 mA, top up	Hor.	λ	σ	55.8 ± 3.0
Std. user, 250 mA, top up	Hor.	λ	π	54.7 ± 2.9
Low-α, ≈95 mA, decay	Hor.	d	σ	153.1 ± 8.1
Low-α, ≈95 mA, decay	Hor.	d	π	150.7 ± 7.9
Low-α, ≈95 mA, decay	Hor.	λ	σ	153.3 ± 8.1
Low-α, ≈95 mA, decay	Hor.	λ	π	150.4 ± 8.0
Low-α, ≈15 mA, decay	Hor.	d	σ	143.5 ± 7.6
Std. user, 250 mA, top up	Ver.	d	σ	49.5 ± 2.6
Std. user, 250 mA, top up	Ver.	d	π	49.8 ± 2.7
Std. user, 250 mA, top up	Ver.	λ	σ	53.7 ± 3.3
Std. user, 250 mA, top up	Ver.	λ	π	52.9 ± 3.2
Low-α, ≈95 mA, decay	Ver.	d	σ	138.2 ± 7.2
Low-α, ≈95 mA, decay	Ver.	d	π	137.8 ± 7.3
Low-α, ≈95 mA, decay	Ver.	λ	σ	143.2 ± 8.1
Low-α, ≈95 mA, decay	Ver.	λ	π	139.8 ± 7.4
Low-α, ≈15 mA, decay	Ver.	d	σ	124.7 ± 6.6

the thicker filter and high integration time and once with a thinner filter and lower integration time. For the comparison only the values measured with the thicker filter are considered, since the thinner filter decreases the average photon energy

and therefore increases the resolution limit of the systems. The measurements from the pinhole systems can be found in Tab. 5.2. There are no measurement errors considered for the pinhole measurements, since the main contribution is always the resolution limit and the statistical errors are about 1 µm.

Table 5.2.: Transverse beam sizes measured with the pinhole systems for standard user and low-α operation.

Storage ring	Orientation	PINH3 / µm	PINH9 / µm
Std. user, 250 mA	Hor.	75.0	65.9
Std. user, 250 mA	Ver.	84.4	51.3
Low-α, ≈100 mA	Hor.	137	124
Low-α, ≈100 mA	Ver.	155	124
Low-α, ≈15 mA	Hor.	136	124
Low-α, ≈15 mA	Ver.	149	124

Comparison of Systems To compare the measurements from the three systems the different source point parameters have to be considered. For a Gaussian beam the beam size can be calculated with the source parameters according to [22, Eq. 8.67]:

$$\sigma_u(z) = \sqrt{\varepsilon_u \beta_u(z) + \delta^2 \eta_u^2(z)}, \tag{5.1}$$

where β is the β-function of the Twiss parameters, δ is the energy spread, η the dispersion and $u = x, y$. The lattice parameters to calculate the beam size at the three relevant positions for standard user and low-α are shown in Tab. 5.3. The source point positions of the systems can also be seen in Fig. 2.1. All three systems are positioned at similar positions with a high vertical and a low horizontal β-function. The horizontal beam sizes calculated with Eq. 5.1 are listed in Tab. 5.4.

Table 5.3.: Positions and optical parameters of the source points of the interferometer and the pinhole systems in standard user and low-α mode.

	Mode	PINH3	Interferometer	PINH9
Position s / m	–	35.04	35.07	125.03
Hor. β-function / m	Std. user	0.396	0.390	0.463
Ver. β-function / m	Std. user	21.1	21.1	22.5
Hor. dispersion / m	Std. user	0.0083	0.0104	0.0098
Hor. β-function / m	Low-α	0.672	0.628	0.676
Ver. β-function / m	Low-α	23.6	23.6	22.7
Hor. dispersion / m	Low-α	−0.034	−0.028	−0.035

The source point parameters are almost the same for the interferometer and the PINH3 system in standard user and for the PINH3 and the PINH9 system in low-α mode. The calculated horizontal beam sizes in standard user mode are around 45 µm for the interferometer and the PINH3 system and 4 µm higher for the PINH9 system. Note that for the calculation of the beam sizes in standard user operation an emittance of 5 nm rad was used, which is a better approximation for the real case

Table 5.4.: Horizontal beam sizes in standard user and low-α mode calculated from the source point parameters given in Tab. 5.3.

	PINH3	**Interferometer**	**PINH9**
Std. user σ_x / µm	44.5	44.2	48.1
Low-α σ_x / µm	132.5	127.6	133.0

than the emittance of 7.5 nm rad from the model, which does not consider any insertion devices. In low-α mode the beam sizes for the PINH3 and the PINH9 system are around 133 µm and slightly lower for the interferometer. Note that the model for low-α operation does not consider any bursting effects. A value for the vertical beam sizes cannot be obtained this easily as the main contribution is the vertical emittance introduced by coupling and the value given in Tab. 2.1 is only based on rough estimations.

In standard user mode the measured horizontal beam sizes are in general all higher than the ones calculated from the model. While the measurements from the interferometer and the PINH9 system are about up to 10 µm larger, the values measured with the PINH3 system are significantly larger. Although there are no absolute values for the vertical beam sizes to compare to from the model, there should still be only slight differences for all three systems. The measurements from the interferometer and the PINH9 system agree, but the measurement from the PINH3 system is again significantly larger. In general the measurements with the interferometer and the PINH9 system are within in the scope of what was expected to measure. The measured beam sizes are higher, which is probably caused by resolution limits of the systems. The PINH3 system seems to have a significantly higher resolution limit and for such low beam sizes a comparison to the other systems is not useful.

In low-α mode at high current the horizontal beam sizes measured with the interferometer are 25 µm larger than from the model. The beam size measured with the PINH3 system is close to and the beam sizes from the PINH9 system is smaller about 10 µm compared to the model. In the vertical case the PINH9 system measured the smallest beam size with 124 µm, the interferometer about 140 µm and the PINH3 system the largest with 155 µm. At low current the beam sizes measured with the PINH3 system are slightly smaller, for the interferometer measurement a more significant decrease of about 10 µm in both dimensions was measured and for PINH9 no changes were observed. For lower current the beam sizes measured with the PINH3 system decrease only a bit or not at all for the PINH9 system, while at the interferometer the both transverse beam sizes are significantly smaller than the ones measured at high current. The differences to the model are again likely caused by the resolution limits of the systems. However it is not understood why only the beam size measured with the interferometer changes significantly and that the PINH3 system measures a lower beam size in the horizontal, but a higher beam size in the vertical direction compared to the interferometer.

Summarizing the interferometer measurements itself, in general the slit separation scans seem more reliable than the wavelength scans. The setup only changing the slit separation is much easier to align, the scan can cover larger visibility ranges and the measured beam sizes are closer to the model and have smaller errors. For the wavelength scans it was for some parameter combinations not possible to find a slit position with equal slit intensities. This may be caused by wavefront errors, which

are not understand and are different concerning the wavelength and the polarisation. For example the wavelength of 400 nm seems to be very good for measurements and in low alpha also wavelengths from 600 nm to 700 nm except for the vertical direction with π-polarisation worked fine. Compared to the pinhole systems the slit separation scan with the interferometer provides a more accurate tool to measure the transverse size. However all beam sizes measured in standard user mode are larger than expected from the model. This likely caused by vibrations of the photon beam and has to be investigated.

5.2. Vertical Beam Size Manipulation

One of the first tests with the interferometric beam size monitor was to measure the beam size over a wider range and compare it with the two pinhole systems to get some insights about the real resolution of the systems. Therefore the vertical beam size was manipulated with the vertical noise excitation. A white noise generator with a bandwidth of 80 MHz is used to artificially achieve a static blow up of the vertical beam size and a higher lifetime. The beam is kicked with random frequencies and the amplitude of the excitation can be varied from 0 V to 10 V. In standard user operation the noise excitation is set to 2.3 V.

The measurement was done during top up operation in the standard user mode at a current of 250 mA varying the vertical noise excitation from 0 V to 10 V in 0.25 V steps. A wavelength of 400 nm was used and a double slit separation of 15 mm was chosen. The beam sizes measured during the noise scan with the slit interferometer and pinhole systems are shown in Fig. 5.6.

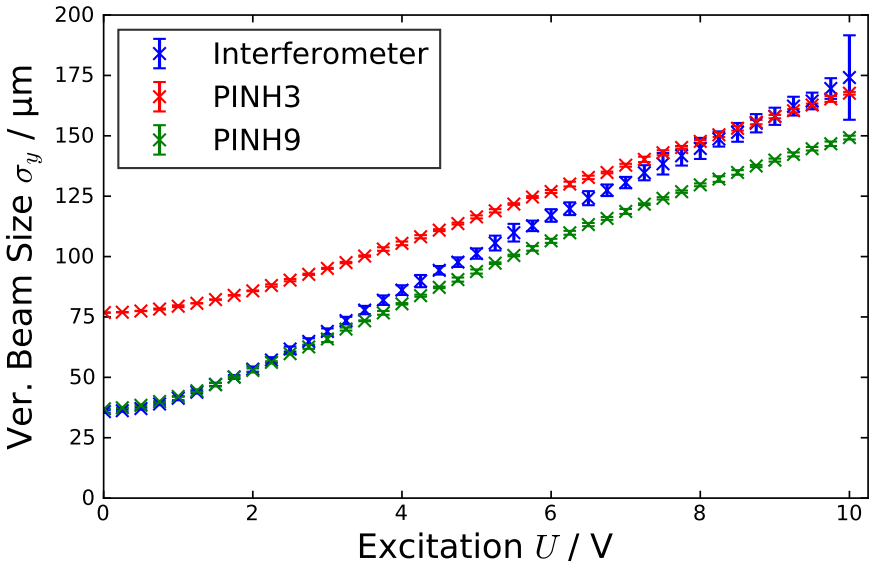

Figure 5.6.: Measured vertical beam size with the interferometer and the pinhole monitors as a function of the vertical noise excitation. For the interferometer a double slit separation of 15 mm and a wavelength of 400 nm were used.

The results from the PINH9 system and the double slit interferometer are in good agreement for beam sizes below 70 µm, while the beam size measured with the PINH3 system is approximately doubled. This implies that the PINH3 system is

not suited to measure smaller beam sizes. For larger excitations the measured beam sizes of the interferometer and PINH3 are in the same region. It is also visible that the interferometer has a higher noise, possibly due to vibrations or air disturbances at the beamline.

Since the source point parameters of all three systems, which can be found in Tab. 5.3, are similar large differences for the different systems are not expected. A consistence check is then to plot beam sizes measured with different systems against each other. It follows from Eq. 5.1, that, assuming the dispersion vanishes in the vertical direction, the squared slope of vertical beam sizes measured at different source positions should yield the ratio of the β-functions of the respective source points. The plots of the beam sizes against each other are shown in Fig. 5.7 together with linear fits and the fit results are listed in Tab. 5.5.

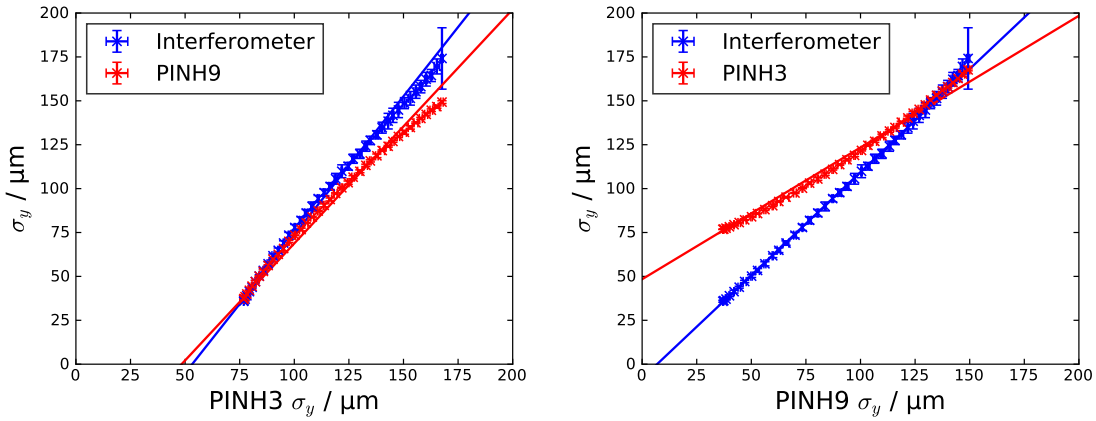

Figure 5.7.: Correlation of the measured vertical beam sizes during noise excitation of the interferometer and the pinhole systems. Linear fits of the measurement data are shown (solid lines).

Table 5.5.: Fit results for beam size vs. beam size plots shown in Fig. 5.7 and calculated β-ratio from Tab. 5.3.

	Slope^2	**Intercept / µm**	**β-ratio**
Interferometer/PINH3	2.49 ± 0.04	-84.0 ± 1.6	1.00
PINH9/PINH3	1.78 ± 0.03	-64.5 ± 1.5	0.94
Interferometer/PINH9	1.38 ± 0.01	-8.0 ± 0.2	1.07

As expected these plots also imply that the PINH3 system has a higher resolution limit than the other two systems and the data points deviate from a straight line for lower beam sizes. From the fits only the result for the comparison of PINH9 and the interferometer is in a reasonable range with an intercept near zero and the closest fit result the squared slope to the β-ratio, though it is still not included in the fit error.

Another approach was then to fit the measured data directly describing the beam size with a constant term σ_0 and a contribution linear in the noise excitation U:

$$\sigma_{\text{noise}}(U) = \alpha U, \tag{5.2}$$

where the constant α denotes the coupling to the excitation. The measured squared beam size is then the sum of those squared terms:

$$\sigma(U)^2 = \sigma_0^2 + \sigma_{\text{noise}}^2(U) = \sigma_0^2 + \alpha^2 U^2. \tag{5.3}$$

The fits of the measured beam sizes for all three systems with Eq. 5.3 are shown in Fig. 5.8 and the results can be found in Tab. 5.6. Since the model did not describe the data very well for higher beam the fit was done additionally only for low excitations up to 4.75 V which corresponds to the first ten data point for each measurement.

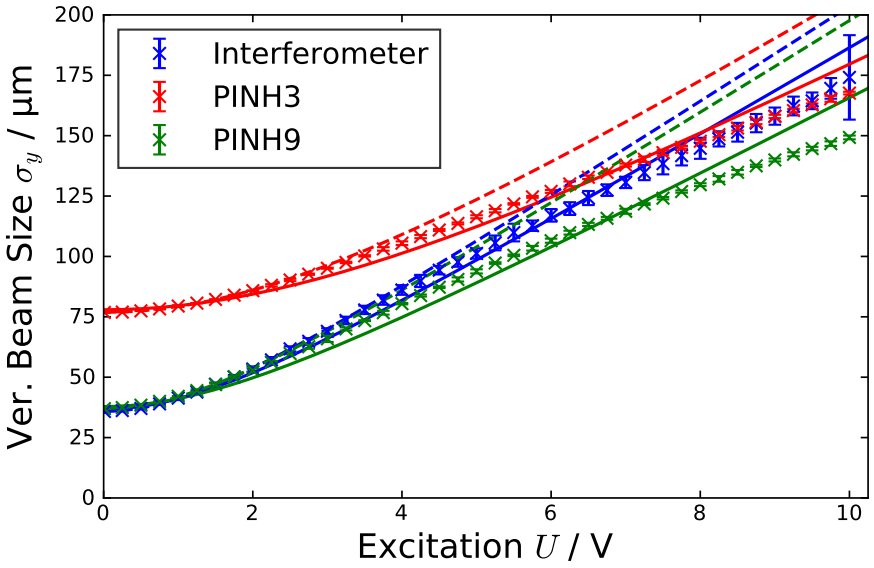

Figure 5.8.: Vertical beam size measured with the three systems as a function of the noise excitation. Fits according to Eq. 5.3 are shown for the complete data (solid lines) and for the first ten data points (dashed lines).

Table 5.6.: Fit results for beam size vs. noise excitation shown in Fig. 5.8.

System	**Data**	σ_0 / **µm**	α / **(µm/V)**
Interferometer	All	36.8 ± 0.4	18.3 ± 0.2
PINH3	All	77.9 ± 0.3	16.2 ± 0.2
PINH9	All	37.8 ± 0.5	16.1 ± 0.2
Interferometer	First ten	35.86 ± 0.08	20.0 ± 0.1
PINH3	First ten	76.87 ± 0.04	19.3 ± 0.1
PINH9	First ten	37.10 ± 0.06	19.4 ± 0.2

Using only the first ten data points of each measurement series, the model describes the data much better. The result from these fits for σ_0 are all lower than from the fits using the complete data and the results for the coupling constant α are all higher and similar for all three systems. The errors from the fits are in general very small, since the error bars of the data in the plot only represent the statistical measurement uncertainty and the uncertainties for slit separation, distance to source nor any systematic error for the interferometer and resolution limit for the pinhole systems are included in the analysis.

From this method one gets a fitted value for the beam size measured at zero excitation in σ_0 and a value for the coupling to the excitation with α. But the problem is that the systems have a resolution limit which is not considered in Eq. 5.3. Adding an additional term σ_{res} for the resolution to Eq. 5.3 describes the actual measured beam size

$$\sigma^2_{\mathrm{meas}}(U) = \sigma^2_{\mathrm{res}} + \sigma^2_{\mathrm{true}}(U) \tag{5.4}$$

$$= \sigma^2_{\mathrm{res}} + \sigma^2_{0,\mathrm{true}} + \alpha^2 U^2. \tag{5.5}$$

So the fit results for σ_0 yield a combination of the resolution limit and the true beam size at zero excitation $\sigma_{0,\mathrm{true}}$, which cannot be differentiated by a single system or multiple system with similar resolution limits.

The idea was then to combine these measurements with measurements from the beam loss monitors. The beam loss monitors consist of sodium iodide scintillation counters and are installed in high dispersion regions in the achromat sensible for the lifetime. For this analysis the measurements from board 9 positioned between the T4 and D5 section and the counts from four different photo diodes (further called BLM1 to BLM4) are used.

The measured loss rate LR is composed by one part independent of the beam size and one part scaling with the beam size:

$$LR = LR_{\mathrm{const}} + LR_{\sigma}. \tag{5.6}$$

The constant term LR_{const} is expected not to change with the shape of the beam only depending on the vacuum conditions and the beam current. The beam size dependent term LR_{σ} is caused by the Touschek effect [22, Chapter 18.1.3] and it is further assumed that this term is inversely proportional to the beam size $LR_{\sigma} \propto \sigma^{-1}$. Using this and Eq. 5.3 the inverse loss rate is then given by:

$$LR = \frac{1}{c} + \frac{\beta}{\sqrt{\sigma^2_{0,\mathrm{true}} + \alpha^2 U^2}} \tag{5.7}$$

$$= \frac{1}{c} + \frac{1}{\sqrt{a^2 + b^2 U^2}}, \tag{5.8}$$

with the constants $c = 1/LR_{\mathrm{const}}$, $a = \sigma_{0,\mathrm{true}}/\beta$ and $b = \alpha/\beta$.

Before comparing the loss rates with the beam sizes it is necessary to eliminate the beam size independent contribution from the loss rate to obtain the beam size dependent loss rate, which is in the following called corrected loss rate $LR_{\mathrm{cor}} \equiv LR_{\sigma}$. Therefore the loss rates are fitted with Eq. 5.8. The fit can be seen together with the measured loss rates as a function of the noise excitation in Fig. 5.9 and the fit results are listed in Tab. 5.7.

With the obtained constants the beam size independent loss rate is now subtracted from the measured loss rate. The corrected loss rates are then normalized and are plotted in Fig. 5.10 and the inverse loss rate is shown in Fig. 5.11. As expected the corrected and rescaled loss rates are pretty similar for the four different loss monitors. For further analysis the average of the inverse normalized corrected loss rate is used. For the inverse corrected loss rate this is also plotted in Fig. 5.11 for

$$LR_{\mathrm{c}}^{-1} = \sqrt{a^2 + b^2 U^2} \tag{5.9}$$

and the parameters are $a = 1.012 \pm 0.003$ and $b = 0.778 \pm 0.005$.

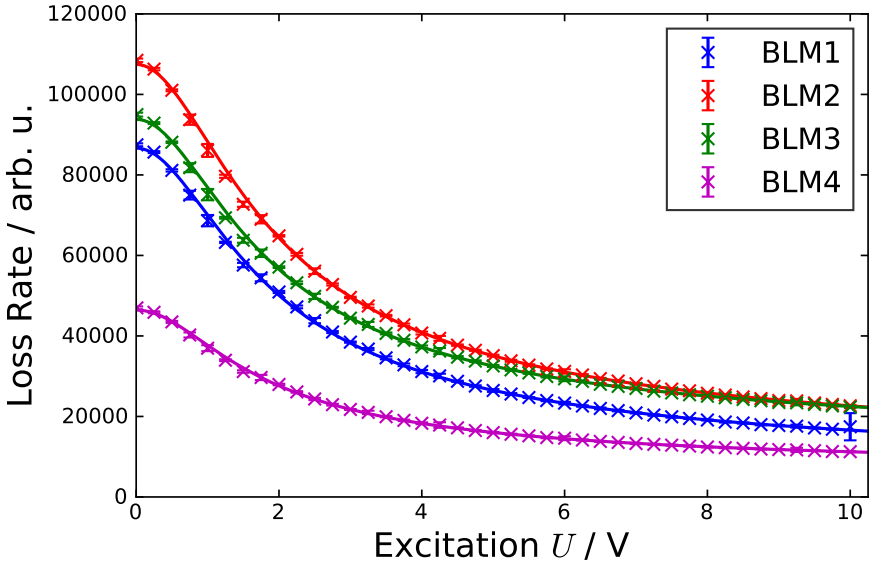

Figure 5.9.: Measured beam loss rates from four different loss monitors as a function of the noise excitation. The loss rates are fitted according to Eq. 5.8.

Table 5.7.: Fit results for the constants of Eq. 5.8 fitting the loss rates as a function of the excitation noise.

	a	b	c
BLM1	$(1.243 \pm 0.004) \cdot 10^{-5}$	$(9.558 \pm 0.071) \cdot 10^{-6}$	$(1.606 \pm 0.032) \cdot 10^{-4}$
BLM2	$(1.021 \pm 0.003) \cdot 10^{-5}$	$(7.555 \pm 0.044) \cdot 10^{-6}$	$(1.051 \pm 0.014) \cdot 10^{-4}$
BLM3	$(1.221 \pm 0.004) \cdot 10^{-5}$	$(9.041 \pm 0.070) \cdot 10^{-6}$	$(8.386 \pm 0.097) \cdot 10^{-5}$
BLM4	$(2.486 \pm 0.010) \cdot 10^{-5}$	$(1.976 \pm 0.015) \cdot 10^{-5}$	$(1.612 \pm 0.016) \cdot 10^{-4}$

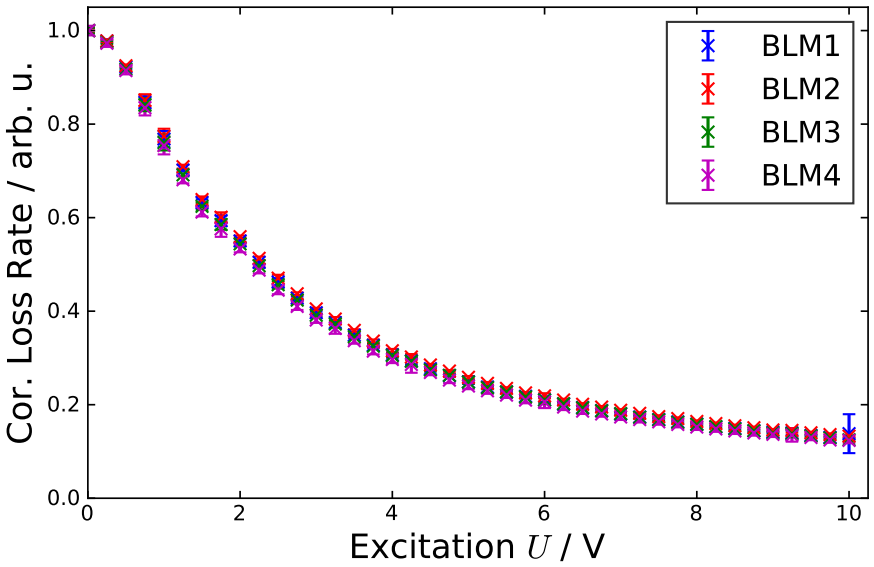

Figure 5.10.: Normalized corrected loss rates measured with the four different loss monitors as a function of the vertical noise excitation.

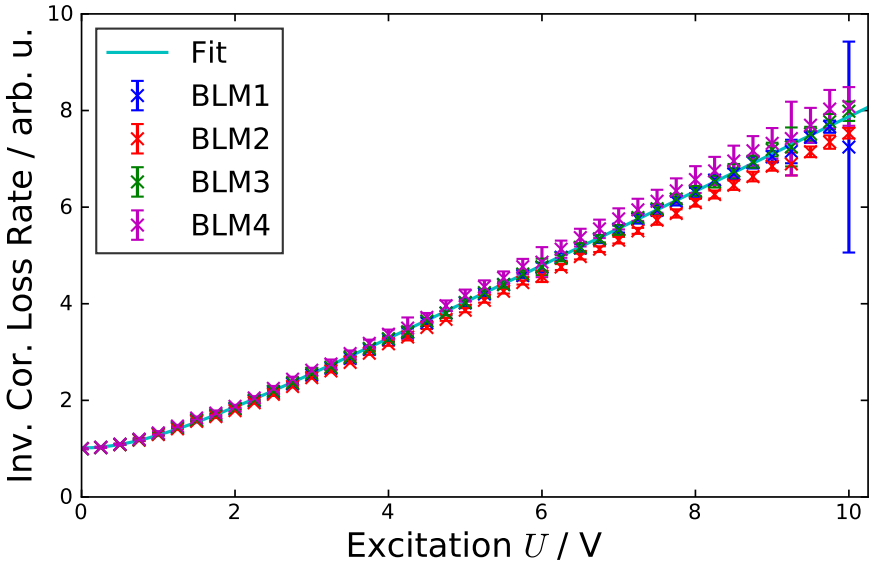

Figure 5.11.: Inverse normalized corrected loss rates measured with the four different loss monitors as a function of the vertical noise excitation and average fit result according to Eq. 5.8 without the constant term.

With this is possible to describe the beam as a function of the loss rate instead of the noise excitation. By solving Eq. 5.7 for the excitation

$$U^2 = \frac{\beta^2 L R_{\mathrm{cor}}^{-2} + \sigma_{0,\mathrm{true}}^2}{\alpha^2} \tag{5.10}$$

the noise can now be substituted in Eq. 5.5 and yields the beam size depending on the loss rate

$$\sigma_{\mathrm{meas}}^2(LR_{\mathrm{cor}}) = \sigma_{\mathrm{res}}^2 + \beta^2 L R_{\mathrm{cor}}^{-2} \tag{5.11}$$

$$= \sigma_{\mathrm{res}}^2 + \sigma_{\mathrm{true}}^2(LR_{\mathrm{cor}}). \tag{5.12}$$

Now it is possible to extract the resolution of the systems and the true beam sizes from the respective source points.

The vertical beam size plotted as a function of the average inverse corrected loss rate shown in Fig. 5.12 together with the fits according to Eq. 5.11. As for Fig. 5.8 the fit is again done for the complete data and for the first ten data points separately and the result are summarized in Tab. 5.8.

Again the fits using only the first ten data points describe the data much better. The results show that the interferometer has a slightly better resolution limit of 25 µm than the PINH9 system with a resolution limit of 28 µm. The PINH3 system has a resolution limit which is more than twice as high of 73 µm and confirms the assumption that the system is not usable to measure lower beam sizes. The large resolution limit of the system might be caused be misalignment of the pinhole array or other issues in the setup. With the results for β it is now also possible to calculate the true beam size at the three source points. At zero excitation the results for all three fits using the first ten data points provides a similar beam size of about 25 µm. The relative uncertainties of all fit results are relatively small, since for the results in Fig. 5.8 again only the statistical uncertainties from the measurement data are used for the analysis.

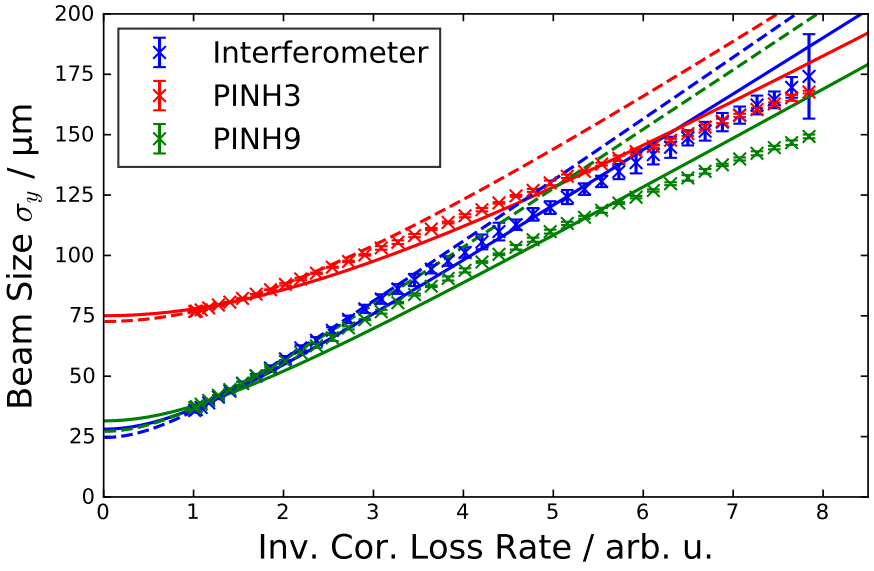

Figure 5.12.: Vertical beam size measured with the three system as a function of the average inverse corrected and normalized loss rate. The beam sizes are fitted according to Eq. 5.11 using the complete data (solid line) and only using the first ten data points (dashed line).

Table 5.8.: Fit results for beam size as a function of the average corrected inverse and normalized loss rate shown in Fig. 5.12.

System	**Data**	σ_{res} / **µm**	β / **µm**
Interferometer	All	28.1 ± 0.6	23.5 ± 0.2
PINH3	All	75.0 ± 0.3	20.8 ± 0.2
PINH9	All	31.5 ± 0.6	20.7 ± 0.2
Interferometer	First ten	24.6 ± 0.2	25.8 ± 0.1
PINH3	First ten	72.6 ± 0.1	24.9 ± 0.1
PINH9	First ten	27.2 ± 0.3	25.0 ± 0.3

In general the measurement made it possible to obtain the resolution limit of the systems and the true beam sizes at the respective source points, but also two inconsistencies occurred. The reason why the beam size is behaving different than the model for higher excitation value is unclear. There seems to be a damping effect or some possible nonlinear beam dynamics which reduce the beam size and could be caused by the bunch by bunch feedback systems. This is however not seen in the data from the loss monitors, implying that these effect are either local or the measurement systems are limited. In addition, apart from the PINH3 system, the results for the resolution limits of the systems are larger than expected. For the interferometer the resolution should be much better than 20 µm for beam sizes smaller than 25 µm, see Section 4.5, and also the pinhole system should have a lower resolution limit of about 10 µm. At the interferometer this resolution limit might be the result of a photon beam motion, which cannot be resolved if they are on much smaller timescale than the integration time of the camera. Both issues need further investigations.

5.3. PPRE Excitation

The PPRE bunch is one of the special bunches provided in the standard user fill, see Section 2.1. A narrow band excitation on a resonance is introduced with a horizontal kicker to increase the source size of the beam. This excitation is applied to a single bunch in the pattern, which can then be separated spatially. In standard user operation the excitation is done at the first synchrotron sideband at $(Q_{\mathrm{hor}} - Q_s) f_{\mathrm{rev}}$ and is set to 1.0556 MHz [20].

Since the PPRE bunch cannot be separated at the diagnostic beam line this measurement was done with just the single PPRE bunch inside the storage ring. The storage ring was in standard user optics, but unlike the other measurements two of the three superconducting insertion devices were turned off during these test. The PPRE bunch was filled with 3 mA at the start of the measurement. Due to the low intensity from only one bunch the camera exposure time was set to 30 ms and for the higher expected source size the 600 nm bandpass filter was chosen for the interferometer.

Measurements of the horizontal or vertical beam size of the PPRE bunch were done while varying either the excitation voltage or the excitation frequency of the kicker. In addition to the interferometer the beam sizes were also measured with the pinholes systems. Due to the low intensity at low current the exposure time of both systems was set to 2 s in order not having to use a thinner filter and therefore increase the resolution limit.

For the measurement of the beam size as a function of the excitation voltage a double slit separation of 15 mm was used and the excitation frequency was set to 1.0556 MHz, which is also the frequency used for standard user operation. The voltage was then varied from 0 V to 0.575 V in 0.025 V steps and the result for the horizontal beam size are shown in Fig. 5.13. The measurement was repeated with the same parameter configuration in the vertical direction and the results can be found in Fig. 5.14.

The horizontal beam size measured with the interferometer ranges from about 58 µm at no excitation to about 125 µm at maximum excitation. The range of the beam sizes measured with the pinhole systems are smaller. PINH3 measures beam sizes from 70 µm to 120 µm and the values obtained from PINH9 are always the lowest above 0.1 V and they are ranging from 62 µm to nearly 100 µm. As for the vertical noise excitation the fluctuations at the interferometer are higher than at the pinhole system. Another effect that can be seen for higher excitation is that the beam size increases stepwise.

For the vertical beam size measurements the measured beam size ranges from the three systems are different. While the measurements from the interferometer and the PINH3 system look similar in their shape, they range from 68 µm to 110 µm and from 97 µm to 132 µm, respectively. However the beam size measured with the PINH9 system increases only from 55 µm to 64 µm. The effect of the PPRE excitation on the vertical beam size is probably cause due to coupling and non equilibrium dynamics.

Compared to the measured beam sizes in standard user mode in Section 5.1, see Tab. 5.1, the beam sizes measured with this setup at no excitation of the PPRE bunch are smaller in the horizontal and significantly higher in the vertical direction for the interferometer and the PINH3 system. At PINH9 the horizontal beam size at no excitation is smaller and only slightly higher in the vertical direction. The

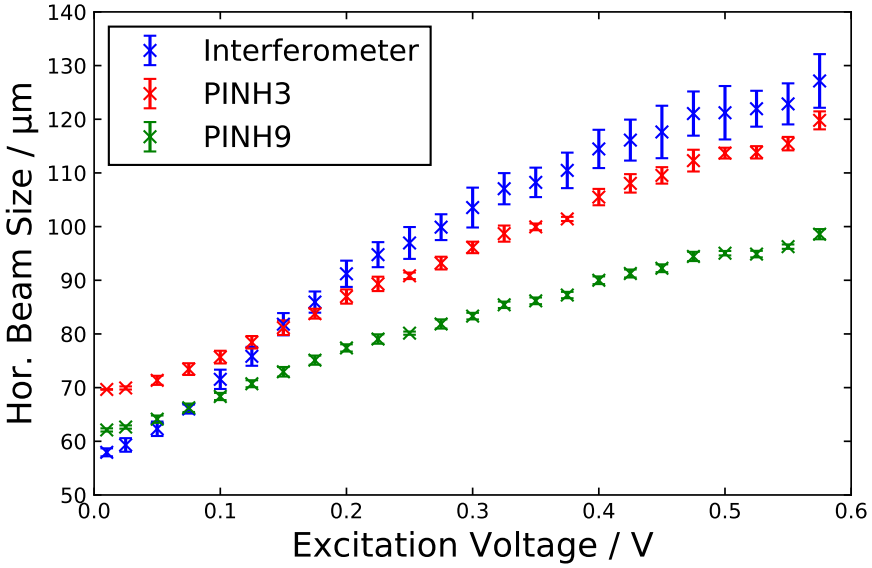

Figure 5.13.: Measured horizontal beam size of the PPRE bunch with the interferometer and the pinhole systems as a function of the excitation voltage for the horizontal PPRE excitation. For the interferometer a double slit separation of 15 mm and a wavelength of 600 nm were used.

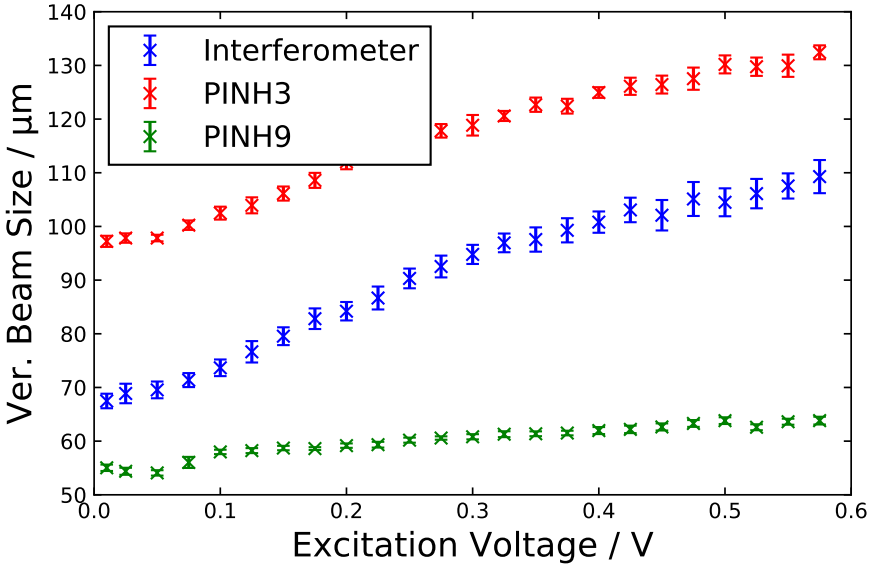

Figure 5.14.: Measured vertical beam size of the PPRE bunch with the interferometer and the pinhole systems as a function of the excitation voltage for the horizontal PPRE excitation. For the interferometer a double slit separation of 15 mm and a wavelength of 600 nm were used.

differences are likely caused by the different storage ring setup without two superconducting IDs. In addition the higher beam current could have an effect on the beam size, since all measurements in Section 5.1 were done with the standard fill pattern, which has a lower average beam current.

Another test was to change the excitation frequency with which the PPRE bunch is excited. For this measurement the excitation voltage was set to 0.25 V and a double slit with 10 mm slit separation was used, since high beam sizes or beam motions

were expected for excitations with a resonant frequency. The excitation frequency was changed from below the first synchrotron sideband at 1.0156 MHz to somewhat above the second synchrotron sideband at 1.0766 MHz in 200 Hz steps to cover at least both sidebands of the horizontal tune. The measured beam sizes as a function of the excitation frequency from the three system are shown in Fig. 5.15.

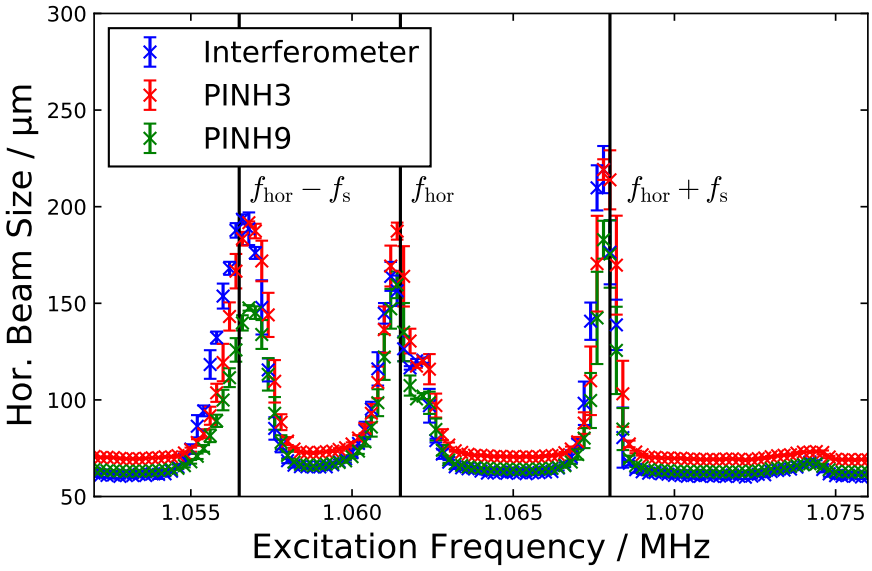

Figure 5.15.: Measured horizontal beam size of the PPRE bunch with the interferometer and the pinhole systems as a function of the excitation frequency for the horizontal PPRE excitation. For the interferometer a double slit separation of 10 mm and a wavelength of 600 nm were used.

The scan of the excitation frequency shows the peaks for the horizontal tune. The peak caused by the horizontal tune $f_{hor} = Q_{hor} f_{rev}$ is at about 1.0615 MHz and the peaks from the first sidebands $f_{hor} \pm f_s$ are at 1.0565 MHz where the excitation in standard user mode is done and at 1.068 MHz. In these peaks horizontal beam sizes up to 220 µm were measured with the interferometer and the PINH3 system. As for the voltage scan the beam sizes measured with the PINH9 system are smaller. A small peak for the second sideband can be seen at about 1.074 MHz. The distances between the peaks range from 5 kHz to 6.5 kHz, which is lower than the nominal synchrotron frequency of 8 kHz. The measurements from the pinhole systems are a bit delayed, since the frequency was changed every 5 s, which is in the order of the camera integration time.

Further analysis comparing the measurements of the three different peaks like in Section 5.2 systems were not done. Comparing the slopes of the beam sizes plotted against each other should yield the ratios of β-functions from the source point of the systems. However, in the horizontal direction Eq. 5.1 contains a dispersion term and the fits did not yield anything useful. Especially it has to be further investigated why the interferometer and the PINH9 behaved different in this setup compared to previous measurement. Moreover it is not easily possible to use the beam loss monitors since the model used for the vertical noise excitation does not apply in the horizontal case and a resolution limit of the systems cannot be calculated the same way for the horizontal direction. In general the PPRE excitation gives the possibility to study a variable horizontal beam size and with a bunch resolved setup it will be possible to measure its transverse properties during user operation.

5.4. Energy Ramp

Another parameter which affects the beam size is the electron energy. The horizontal equilibrium beam emittance is given by [22, Chapter 10.2]

$$\varepsilon_x = C_\mathrm{q}\gamma^2 \frac{\langle \mathcal{H}/|\rho^3|\rangle_z}{J_x \langle 1/\rho^2\rangle_z} \tag{5.13}$$

where C_q is the quantum excitation constant, γ the Lorentz factor, ρ the bending radius, J_x the damping partition number, $\langle \ldots \rangle_z$ denotes the average taken along the considered beam trajectory, and $\mathcal{H}$ is a lattice function defined by the Twiss parameters α_x, β_x, γ_x and the dispersion η:

$$\mathcal{H} = \beta_x \eta_x'^2 + 2\alpha_x \eta_x \eta_x' + \gamma_x \eta_x^2. \tag{5.14}$$

Furthermore the energy spread is given as

$$\delta^2 = C_\mathrm{q}\gamma^2 \frac{\langle |1/\rho^3|\rangle_z}{J_\varepsilon \langle 1/\rho^2\rangle_z}, \tag{5.15}$$

with the longitudinal damping partition number J_ε. Inserting Eqs. 5.13 and 5.15 into Eq. 5.1 it is expected to observe a linear dependency of the measured horizontal beam size on the beam energy

$$\sigma_x \propto \gamma, \tag{5.16}$$

until the resolution limit dominates the measured beam size.

Measurements were done during the configuration of the energy ramp for BESSY II and the superconducting IDs were turned off. The beam size was measured with a double slit separation of 25 mm at wavelength of 550 nm with σ-polarisation. The camera exposure time was adjusted depending on the beam current during the ramps. For multi bunch operation the beam energy was changed from 1.7 GeV down to 600 MeV and two measurement series, once for a high current of approximately 110 mA and once for a low current of approximately 4 mA, are shown in Fig. 5.16.

For beam energies down to about 1.2 GeV the beam sizes behave similar for high and low current. The beam size of the low current beam decreases further until it reaches a plateau at about 38 µm below energies of 900 MeV. The beam size for high beam current however, increased again and a large part of the beam was lost slightly below 1.1 GeV because the fast orbit feedback system was not configured for high currents. This can also be seen in Fig. 5.17 where the maximum horizontal beam motion is shown during the measurement. The maximum beam motion is measured by the bunch by bunch feedback providing the maximum rms motion of a single bunch.

Compared to the low current measurements the beam motion is more than an order of magnitude higher for the measurements with 110 mA below 1.65 GeV. Multiple smaller steps can be seen in Fig. 5.17, e. g. at 1.4 GeV and at 1.1 GeV where the beam was lost. The different densities of the beam size measurement in the plots depend on the ramp speed, which is slower for lower energies and was increased after the beam loss.

For the low current measurement the energy ramp was paused every 100 MeV to make static beam size measurement at that energy (spikes in Fig. 5.16). This was

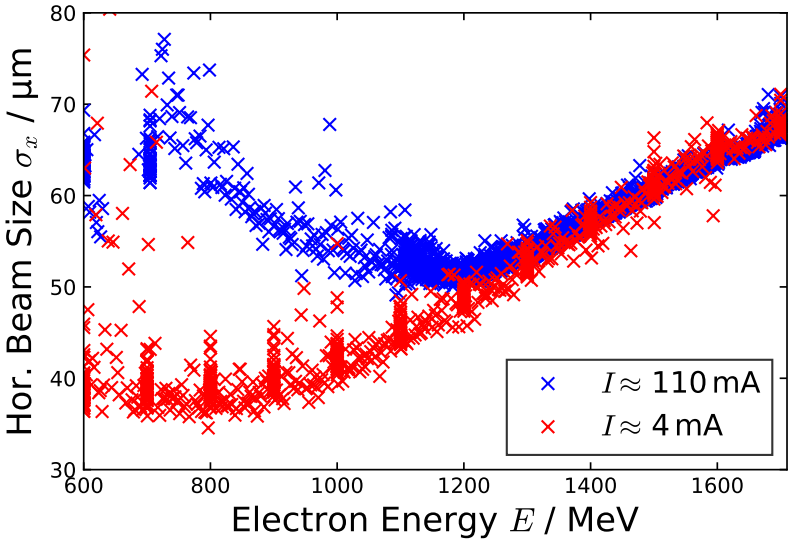

Figure 5.16.: Measured horizontal beam size as a function of the beam energy with the interferometric beam size monitor during the energy ramp for currents of approximately 4 mA and 110 mA. For the interferometer a double slit separation of 25 mm and wavelength of 550 nm were used.

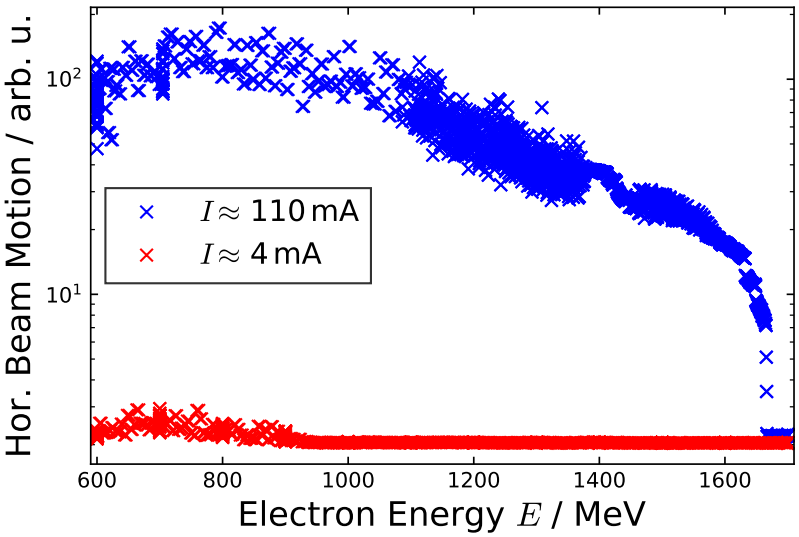

Figure 5.17.: Horizontal beam motion as a function of the beam energy measured during the energy ramp for currents of approximately 4 mA and 110 mA.

repeated for the up ramp from 800 MeV back to 1.7 GeV with approximately 1 mA and the measured beam sizes are shown in Fig. 5.18.

The beam sizes for both measurements are similar for the different energies and roughly follow the from the theory expected linear dependency on the energy between 900 MeV and 1.7 GeV. Below 900 MeV the beam size is then probably dominated by the resolution limit of the interferometer or other nonlinear effects.

The energy ramp was reconfigured in further commissioning shifts and should now

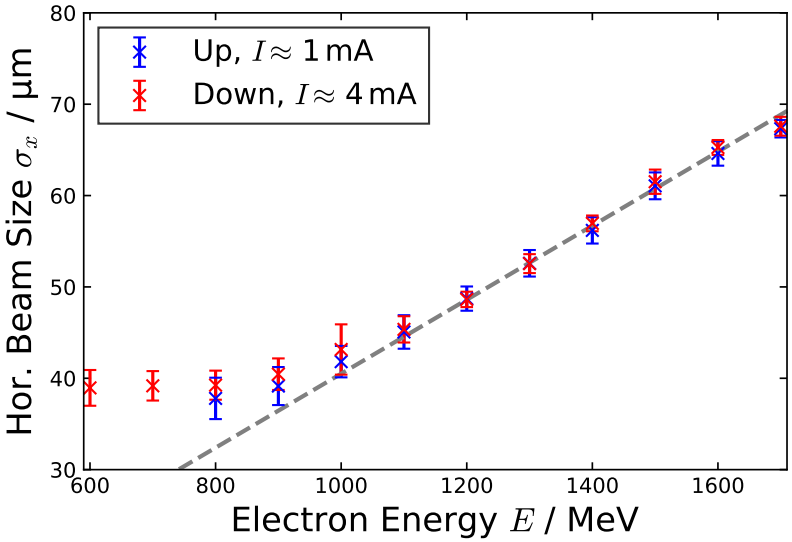

Figure 5.18.: Measured horizontal beam sizes with the interferometric beam size monitor for different beam energies on the up and down ramp for low current. An auxiliary line through the origin is depicted in gray and shows the linear behavior for higher beam energies according to Eq. 5.16.

also enable stable beam conditions for higher beam currents. Beam size measurements with the pinhole systems are not useful for lower beam energies, since these systems use a photon energy just below the maximum photon energy produced at the standard 1.7 GeV beam energy. The synchrotron spectrum is shifted to lower energies and the needed high energy photons vanish already for energies below approximately 1.6 GeV. Therefore the interferometric beam size monitor gives the only opportunity to measure the beam size for lower energies.

5.5. Two Dimensional Beam Profile Measurements

A method to use the double slit interferometer to reconstruct the transverse beam profile is introduced in [34]. By rotating the double slit the visibility can be measured as a function of the angular orientation and by calculating the horizontal and the vertical contribution for each orientation the two dimensional beam profile can be reconstructed, see also Eq. 3.21.

In standard user mode the measurement was done with a current of 250 mA and with a double slit with 20 mm slit separation. With the rotation of the double slit a large region of the beam spot is needed for this measurement. To minimize the error from wavefront distortions the 400 nm bandpass filter was chosen, which already proved to work well for the measurements in Section 5.1. The camera exposure time was set to 1 ms and the camera was rotated simultaneously with the double slit to provide the intensity projection corresponding to the double slit orientation. The visibility was measured starting in the horizontal direction in 5° steps with π-polarisation and in 10° steps with σ-polarisation until the system was again in the horizontal orientation, but upside down. The incoherent depth of field effect was applied by obtaining the ratio of the beam size considering and not considering the

effect and then rescaling the horizontal contribution for each angle with this ratio. This assumes a constant horizontal beam size depending on the vertical position. The obtained beam size as a function of the rotation angle is shown in Fig. 5.19.

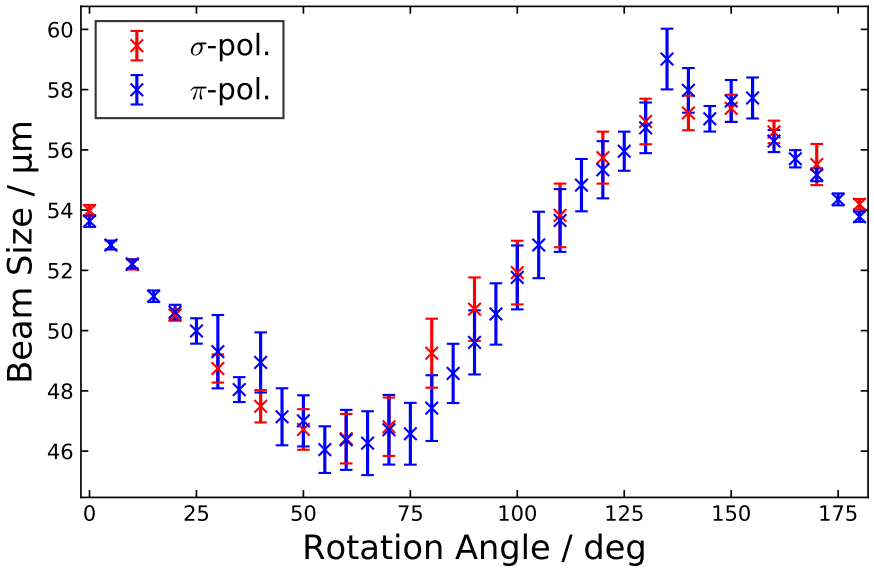

Figure 5.19.: Measured transverse beam size as a function of the rotation angle of the double slit interferometer in standard user operation, 0° corresponds to the horizontal orientation. For the measurement a double slit separation of 15 mm a wavelength of 400 nm was used.

The measured beam size ranges from approximately 46 µm at 55° to about 58 µm at 140° and seems to change continuously with the rotation angle. There is also an increase of the measurement fluctuation near the vertical direction for angles between 40° and 120° observed, which might correspond to the orientation of a possible vibration.

From the beam sizes measured as a function of the rotation angle $\sigma(\phi)$ the respective horizontal and vertical beam sizes can be calculated with

$$\sigma_x(\phi) = \sigma(\phi)\cos\phi \tag{5.17}$$

$$\sigma_y(\phi) = \sigma(\phi)\sin\phi. \tag{5.18}$$

For the standard user measurement those are plotted in Fig. 5.20 to give the transverse beam profile.

As already deducted from beam size as a function of the angle the beam is an ellipse with a minor axis length of about 46 µm and a major axis length of about 58 µm and the major axis is rotated by approximately −37.5° from the horizontal orientation. Note that the measured beam profile is vertically mirrored due to the beam line mirror geometry, which essentially reflects the synchrotron radiation in the backwards direction.

The measurements were repeated in low-α mode once for high current at approximately 98 mA and once for low current at about 14.5 mA. For this measurement the double slit with 15 mm slit separation was chosen and the exposure time was set to 2 ms for the high current and to 20 ms for the low current measurement. The measurements were done with σ-polarisation, therefore the 600 nm bandpass filter, which performed well in the measurements in Section 5.1, was used to increase the

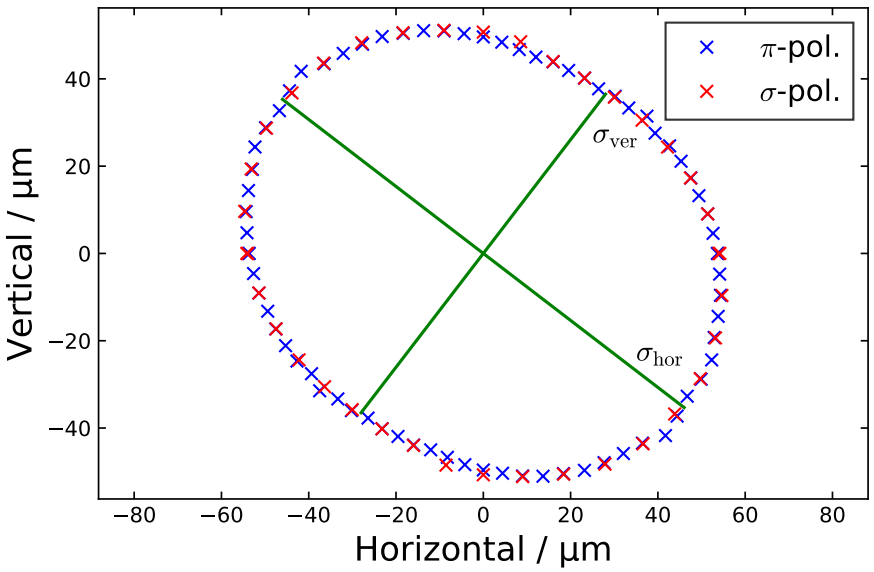

Figure 5.20.: Transverse standard user beam profile calculated from the measurements shown in Fig. 5.19.

visibility. Both measurements were done in 10° steps from 0° to 180°. The effect of the incoherent depth of field effect is considered the same way as previously for the measurement in standard user mode. The results for the transverse beam size as a function of the rotation angle are shown in Fig. 5.21 and the therefrom calculated transverse profiles can be found in Fig. 5.22.

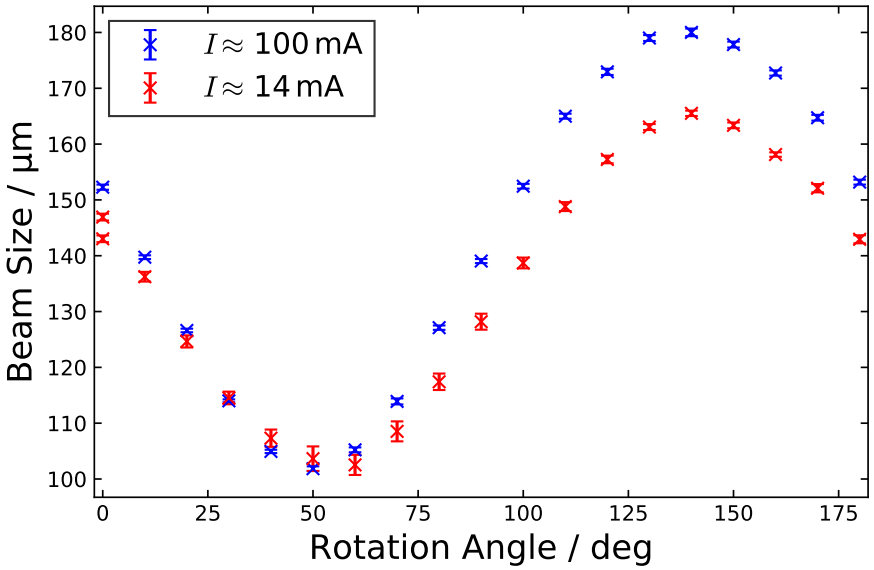

Figure 5.21.: Measured transverse beam size as a function of the rotation angle of the double slit interferometer at high and low current in low-α operation, 0° corresponds to the horizontal orientation. For the measurements a double slit separation of 15 mm and a wavelength of 600 nm was used.

For high current the transverse beam sizes ranges between approximately 105 µm and 180 µm. For lower current the minimum beam size decreases only slightly and

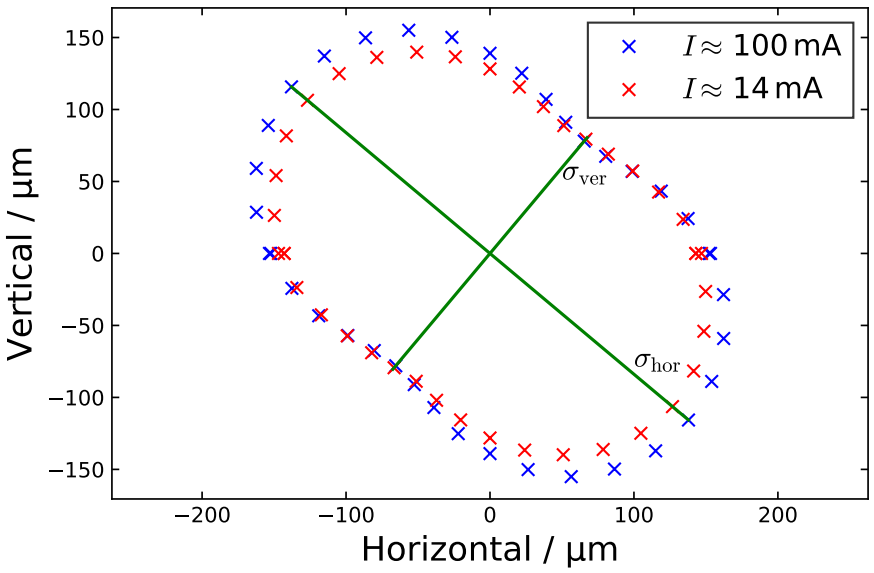

Figure 5.22.: Transverse low-α beam profile calculated from the measurements shown in Fig. 5.21 for high and low current.

the maximum reduces more significantly to about 165 µm. For both measurements the maximum beam size was measured at 140° and the minimum beam sizes were measured at 50° and 60° respectively resulting in a rotation of about −40° of the major ellipse axis from the horizontal direction. This time, the effect of higher fluctuations for some angles was not observed to the same extend as for the standard user measurements and only in the region of the minimum beam sizes for low current the fluctuation was higher. Because of the significant decrease of the major axis for lower beam current, it is assumed that this is the actual horizontal beam size.

The method worked and it was possible to obtain a two dimensional beam profile. The most difficult part of the measurements was to align the setup in a way that it was possible to minimize wavefront errors or intensity imbalances while rotating the double slit, since this method covers a much larger array of the beam spot than other measurements. Another issue was that especially for angles away from the horizontal or vertical axis it was not possible to interfere the light from both slits optimally. The ROI had to be chosen carefully for those angles, since this caused that only a part of the light spot on the camera had an interference pattern with equal intensities from both slits. This effect is likely caused by spherical aberration of the lenses and an imperfect alignment of the center of the lens and the center of the double slit. Further investigations concerning the rotation of beam are proposed. One approach would be to do further studies for different coupling configurations, e. g. by changing skew quadrupole settings, and to test the effect of the vertical noise excitation. In addition this should be compared to models including coupling effects.

5.6. Simultaneous Measurement of Horizontal and Vertical Beam Size

For simultaneous measurements of the horizontal and vertical beam size usually two separate system are used, e. g. a second beam line enabled by a beam splitter with another double slit and camera. Alternatively it is also possible to use a two dimensional interferometer and to obtain the transverse beam sizes from only one camera image [35].

Some two dimensional measurements are shown, since this concept would be very useful for future bunch resolved beam size measurements. However, it is not expected to get a perfect two dimensional interference pattern, since the measurements made to obtain the distance to the source in Section 4.1 already showed a difference of the focus length for the vertical and the horizontal direction. For this test purposes a quadrature slit, which shown in Fig. 5.23, was made with the 3D printer like the double slits in Section 4.3. The slit separations are 15 mm and the slit widths are 3 mm in both dimension. All measurements shown in this section were made at a wavelength of 600 nm and with σ-polarisation. A camera image of the interference pattern where it was tried to image both directions equally is shown in Fig. 5.23.

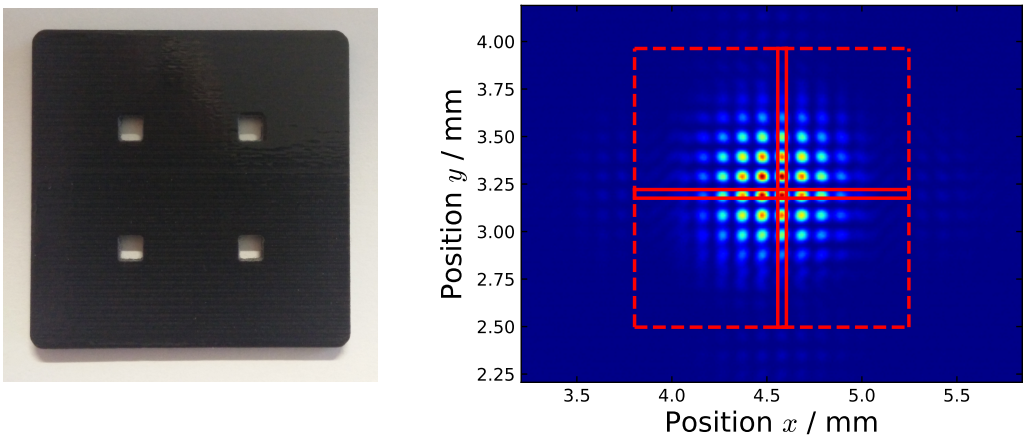

Figure 5.23.: Picture of the quadrature slit made with the 3D-printer (left) and the camera image of the interference pattern while trying to image the horizontal and vertical direction equally. In solid red the ROIs used for the one dimensional analysis in the horizontal and vertical direction and in dashed the combination used for two dimensional analysis are shown.

The interference pattern was then analyzed with regular ROIs with a width of ten pixel for both directions and with a larger ROI, which is obtained by the maximum width and height of the two smaller ROIs. Note that the smaller ROI is shifted to a maximum if in the center of the envelope of the single slit interference is a local minimum. The large ROI enables a simultaneous analysis of the interference pattern for both directions providing an intensity projection for the horizontal and for the vertical interference pattern. In addition the impact of the ROI size can be tested for this setup. The ROIs can also be seen in Fig. 5.23 and the intensity projection from the ROIs and the corresponding fits are shown in Fig. 5.24.

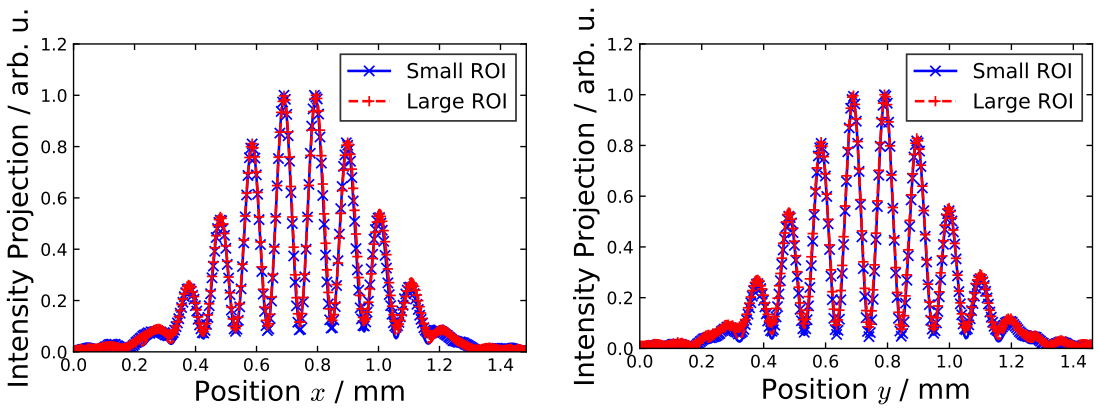

Figure 5.24.: Projection data and fit according to Eq. 4.2 of the interference pattern of Fig. 5.23 for the smaller (blue) and the larger (red) ROIs in the horizontal (left) and vertical (right) direction.

The results of the fits are listed in Tab. 5.9, but especially near the minimum of from the single slit envelope on the edges of the intensity projection one can recognize that the image is not focused perfectly and the fit does not match the data very well there. This effect is similar for the smaller and the larger ROI, but for the larger ROI also the minima near the center are higher and the visibility decreases due to imperfect focusing. This measurement was then compared to tests where it was tried to optimize the focusing for the horizontal and vertical direction respectively. Exemplary camera images are shown in Fig. 5.25.

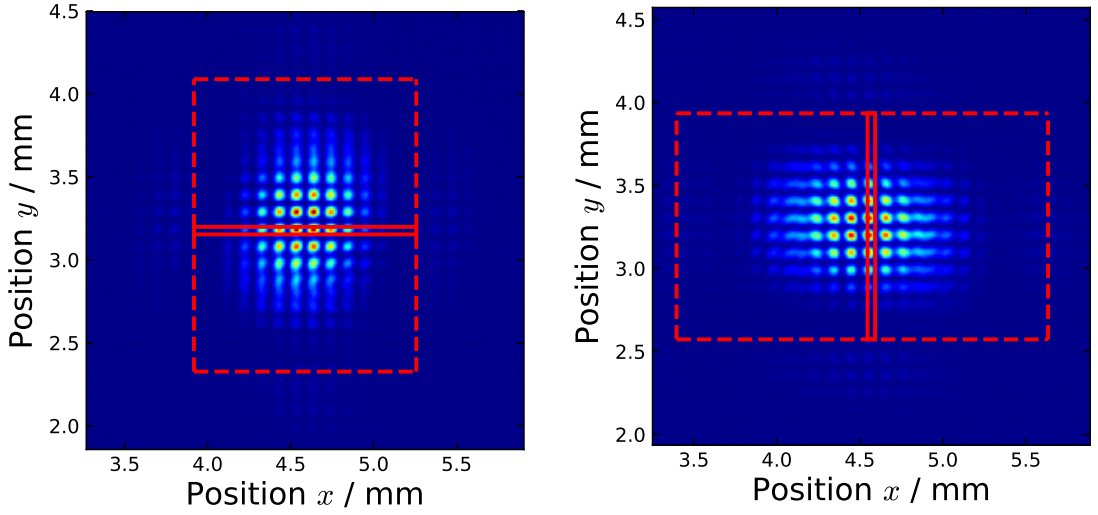

Figure 5.25.: Camera images of the interference pattern of the quadrature slit focused for the horizontal (left) and the vertical (right) direction. The ROIs for the one (solid) and two dimensional (dashed) analysis are shown.

The interference patterns are now widened in the respective direction which is not focused. This images were also analyzed with two different ROIs, but only for the respective focused direction. The intensity projections and fits of the interference patterns are shown in Fig. 5.26 and the fit results can also be found in Tab. 5.9.

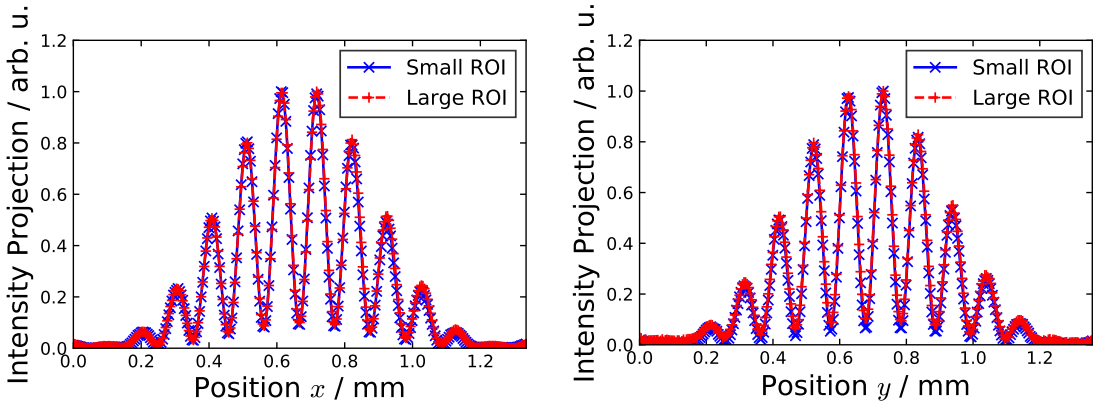

Figure 5.26.: Projection data and fits according to Eq. 4.2 of the interference patterns of Fig. 5.25 for the smaller (blue) and the larger (red) ROIs in the horizontal (left) and vertical (right) direction, respectively.

Table 5.9.: Beam sizes measured with a setup for simultaneous measurement of horizontal and vertical beam sizes. The fit results of the interference pattern shown in Figs. 5.24 and 5.26 are given.

Focus	**ROI**	σ_x / **µm**	σ_y / **µm**
Both	Small	55.3	52.0
Both	Large	65.1	66.7
Hor.	Small	53.5	–
Hor.	Large	56.1	–
Ver.	Small	–	55.3
Ver.	Large	–	67.2

The projection data looks much better for both ROIs in horizontal and vertical direction and the fit results of the projection data from the smaller ROIs are close to the beam sizes measured in Section 5.1. The horizontal beam size is somewhat higher, which might be caused by non-optimal alignment. The beam sizes obtained from the intensity projection of the larger ROIs are significantly larger and the impact is higher than measured with the regular double slit in Section 4.5, especially for vertical beam size measurements. In the vertical case the beam sizes obtained from the worse focused image are actually smaller. The added constant in the fit shifts the minimum up due to the bad focusing near the minimum of the single slit envelope and thus increases the visibility. Note that no uncertainty estimation of the measured beam sizes is done and exemplarily only “good” images are shown to demonstrate the concept. At the present setup a quadrature slit is not useful to monitor the horizontal or the vertical beam size since vibrations result in high systematic fluctuations towards lower visibilities.

Assuming a perfect setup concerning the wavefront the simultaneous measurement of the transverse beam sizes with a quadrature slit generally brings some disadvantages in terms of flexibility. The parameter setup for horizontal and vertical measurements has to be similar except for the slit separation and for convenience horizontal and vertical beam size should also be in same order of magnitude. But with regard to the upgrade to a bunch resolved system (see next chapter) it might worth giving up some flexibility and the effort to improve the setup allowing simultaneous measurements of the horizontal and vertical beam size.

6. Outlook

This chapter lists possible upgrades or modifications of the existing system to minimize errors and some further applications of the interferometric size monitor. Finally the upgrade to a bunch resolved system is discussed.

6.1. Upgrades

Mirror Distortion The mirror distortion has a large impact on the beam size measurement, especially for the vertical orientation. This is likely caused by the heat load of the high energy synchrotron radiation bending the mirror slightly towards the source point as illustrated in Fig. 4.11. A possible solution would be to put an absorber in front of the extraction mirror in the center of the synchrotron beam. The concept is shown in Fig. 6.1 and the high energy SR would not reach the extraction mirror. Another possible solution are one or two separate mirrors, which would not cover of the center of the SR beam.

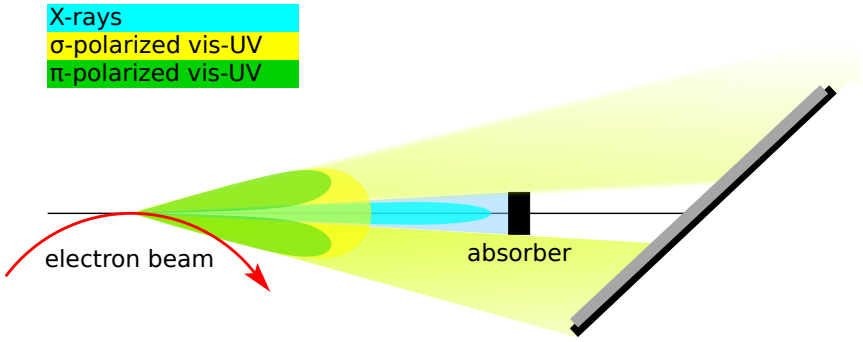

Figure 6.1.: Sketch of an absorber positioned in the center of the synchrotron radiation cone in front of the extraction mirror blocking the high energy SR to reduce the heat load on the mirror.

Wavefront Analysis It could be useful to analyze the wavefront of the synchrotron beam, e. g. with a Hartmann-Shack wavefront sensor. This is in general useful to characterize the synchrotron beam and could give the possibility to identify misalignments or deformations of beam line components, which could then be corrected.

Double Slits The double slits made with the 3D printer were optimal for testing purposes, however for a final setup double slits with sharper edges and higher accuracy are useful. For this purpose a double slit, were the slits are cut by a laser, was produced. An image of this double slit is shown in Fig. 6.2. This double slit can also be mounted in a regular two inch optics mount and the production accuracy with a few 10 µm is about one order of magnitude higher than those from the 3D printer.

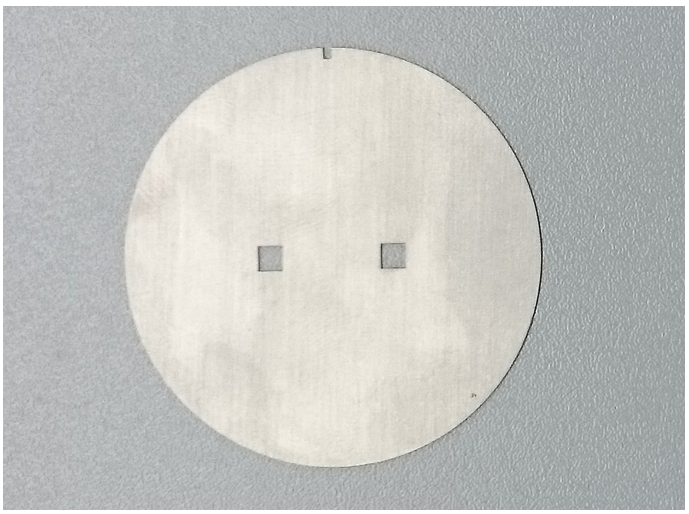

Figure 6.2.: Image of a laser cut double slit with a single slit width and height of 3×3 mm and a double slit separation of 15 mm.

Focusing Optics Aberration effects can be minimized by a replacement of the present lenses. One possibility are lenses from amateur astronomy telescopes, which have a very high quality and are not too expensive. Another possibility is to use reflective optics instead of lenses [36]. This also circumvents any chromatic effects and enables a much broader bandwidth to be used. The interference pattern can be fitted with an integral over a wide spectrum weighting the spectral intensity distribution.

Polarisation Filter The polarisation filter could be replaced with Glan-Taylor or Glan-Thompson prism. This would separate the synchrotron radiation based on the polarisation and one polarisation could be used for other applications. In addition this method yields a higher extinction ratio.

Vibration and Air Disturbance Possible resolution limits due vibrations of beam line components have to be investigated and minimized to reduce their impact on the visibility measurement. In addition the final setup should be covered to minimize air disturbances.

Data Analysis The data analysis could be upgraded by directly using the camera image instead of the intensity projection by the Labview tool. This would allow two dimensional fits, which could for example include an angle as additional free parameter. This would need some improvement of the fitting tool, however the main obstacle is that the analysis of the raw image has to be done locally at the computer reading out the camera data due to high data rates.

Distance of Double Slit to Source Point The measurement of the distance from the double slit to the source point presently introduces a large contribution to the beam size error compared to the other parameters. Since the measurement with the lens imaging method seems not to be accurate enough, a direct measurement of the distance to the source is necessary to reduce to the beam size measurement errors.

New Diagnostics Beamline It is already planned to move the diagnostics beam line and set it up at different position for BESSY VSR. This is also a reason why not too much effort was put into measuring the distance to the source point and realign the mirrors at the present beam line. However, all estimations and suggestions made in this chapter form the base for the future setup of the interferometric beam size monitor at the new VSR diagnostics beam line.

6.2. Further Applications

Emittance Measurement With Eq. 5.1 and variation of the β-function one could measure the beam size as a function of the β-function at the source point. The slope of $\sigma^2(\beta)$ would then yield the emittance. Similarly the energy spread could be obtained by varying the dispersion and would be given by the slope of $\sigma^2(\eta^2)$ [37]. Another approach is to measure the beam size at two different source points. Since the emittance and the energy spread of the storage ring are independent of the longitudinal position, Eq. 5.1 can be solved for the emittance and the energy spread [38]. These methods however require a very good knowledge of the lattice functions of the storage ring.

Intensity Imbalance Interferometer The effect of an intensity imbalance which is shown in Fig. 3.3 is usually neglected since $I_1 \approx I_2$. It is however possible to introduce a controlled imbalance, e. g. with a half coated flat optics, to artificially reduce the visibility. To calculate the beam size the intensity imbalance can then be corrected enabling a measurement of very small beam sizes with an uncertainty below 1 µm [39].

Beam Shape from Fourier Transform As described in Section 3.3 the Fourier or Fourier cosine transform of the visibility measured as a function of the double slit separation should yield the bunch profile. However this was is not shown in this work, because optimally a high resolution over a larger visibility range is needed. However for a future setup it might be possible to have a higher beam line acceptance and this method might be useful.

6.3. Bunch Resolved Measurements

The main motivation of the work was to setup an interferometric beam size monitor as preparation for bunch resolved transverse beam size measurements needed for BESSY VSR. Ideally all properties and issues of an interferometric beam size monitor which have been studied with the present setup without the ability to obtain bunch resolved measurements will transfer to the future setup. It is proposed to replace the CCD camera with a device enabling bunch resolved measurements. But before discussing the properties of possible devices an estimation of needed number of photons is given.

Number of Photons The estimation from of the photons available at the diagnostics beam line is based on the simulated photon flux given in Fig. 4.3. At a wavelength of 550 nm the photon flux is about $15\,\mathrm{nm^{-1}\,s^{-1}}$ for a storage ring current of 0.2 pA and an opening angle of 6.7 mrad. For a single bunch with a current of 1 mA

observed with a bandwidth of 10 nm it is then expected to observe about 600000 photons per turn. This value has to be rescaled to the effective area of the double slit. Assuming two 3×3 mm holes and an equal distribution of the synchrotron radiation for the area in the simulation approximately 3000 photons per bunch remain for the interference pattern. In addition one has to consider the efficiency of the beam line, e. g. by mirrors, camera and filter, and the setup it is estimated that about one order of magnitude of the photons are lost.

First simulations assuming a 1% camera noise were made and it is estimated that about 10000 photons are required to obtain a sufficient interference pattern for the visibility measurement. This means that an integration of the synchrotron light of up to 100 turns from one bunch is needed and would correspond to integration times in the order of 100 µs [40].

Photo Diode Array One possibility for a bunch resolved measurements would be the use of photo diodes. The CCD camera could be replaced with a photo diode array or only one remotely movable photo diode to scan the interference pattern. Further studies for the properties of photo diode would be necessary, especially concerning the effective sensitive area and the response time. In addition hardware and software for the readout of the photo diode or diode array is required. First tests for this could be performed during single bunch weeks.

ICCD Camera A more convenient approach is to replace the present CCD camera with a gated ICCD (intensified CCD). An ICCD consists of a high performance CCD camera and an image intensifier mounted in front of it. An image intensifier consists of a photo cathode, a micro channel plate (MCP) and a phosphor screen. The incoming photons are converted into photo electrons at the photo cathode and are then multiplied by the MCP. At the phosphor screen the electrons are converted back to photons, which are then imaged at the CCD. The image intensifier also enables the gating of the ICCD down to exposure times of 200 ps. This gating can be repeated at up to every 500 ns, which is smaller than the circulation period. The readout of the CCD and is limited to a maximum frame rate of 20 frames per second, which would correspond to an integration over approximately 60000 turns and should yield sufficient photons flux for the analysis of the interference pattern. With a frame rate of 20 fps interference patterns for 400 bunches can then be taken in 20 s [40, 41]. Since an ICCD is very expensive would be optimal to measure the horizontal and the vertical beam size simultaneously, e. g. with the approach shown in Section 5.6.

7. Conclusion

In the scope of this thesis an interferometric beam size monitor for transverse source size measurements was designed and has been installed at the BESSY II diagnostics beam line. The properties of the beamline and the components of the double slit interferometer are outlined and a detailed estimation of possible error contributions is given. A software tool was developed and can now be used for online measurements with the BESSY II control system. The setup was successfully commissioned and various measurements and tests were made during user operation and machine commissioning. The system is now in use for transverse beam diagnostics in addition to the existing pinhole monitors and the present setup is able to measure beam sizes ranging from about 20 µm to 400 µm with an uncertainty of about 5 %. Due to motions of the photon beam likely caused by vibrations of beam line components the anticipated resolution could not be achieved. Another effect, which complicates the beam size measurements at the present beam line, are distorted wavefronts.

The visibility scans as a function of the slit separation give the possibility for accurate beam size measurement during stable operation. Further tests were done with a variable beam size introduced by an excitation in vertical direction. With the beam loss monitors it was possible to deduct a resolution limit for the interferometer and the pinhole systems to obtain the corrected beam size. In the horizontal case the PPRE bunch gives the opportunity to do similar measurements and will be of interest considering future bunch resolved diagnostics. The measurements made with the interferometric beam size monitor were compared with the pinhole systems and proved to provide a more reliable and flexible system to measure transverse source sizes. In addition the interferometric beam size monitor gives the possibility to measure the beam size at lower energies and with the profile measurement it was possible to get the transverse beam shape at the present source point.

Further possible applications of the existing setup are proposed and a short estimation of the requirements for the upgrade to a bunch resolved system is given. The detailed studies and characterizations made at the present beamline form the base for the design of the bunch resolved interferometric beam size monitor at the new BESSY VSR diagnostics beamline, for which it is planned to replace the CCD camera with an ICCD. It has to be ensured that with regard to bunch resolved measurements especially wavefront distortions and vibrations on the photon beam caused by beamline or interferometer components do not limit the resolution of the beam size measurement.

A. BESSY II Pinhole Monitors

At BESSY II two pinhole systems, PINH3 and PINH9, are in operation to image the source point directly. The pinholes use synchrotron radiation from bending magnets at different positions (see Tab. 5.3 and Fig. 2.1) to measure the source dimension, the vertical opening angle, the horizontal and vertical source position and the emission angle. Because of the diffraction limit X-ray wavelengths must be used. The systems are placed inside the storage ring bunker to give online measurements independent concerning the beam shutters, e. g. during injection.

The principle of a pinhole system at a bending magnet is shown in Fig. A.1. The synchrotron light is falling through a pinhole array onto a phosphor screen, which converts the radiation into visible light. The array consists of 11×21 pinholes with a 20 µm diameter, positioned 6.1 m distant from the source. To increase the resolution the bandwidth of the observed radiation is limited by a molybdenum filter, resulting in an average photon energy of 16.33 keV, which falls onto the phosphor screen. At the phosphor screen the high energy photons are converted into visible light, which is then imaged onto a CCD camera. By knowing the geometry of the pinhole setup and the imaging system the beam size and other parameters can be calculated. The resolution of the pinhole systems is 11 µm [11, 42, 43].

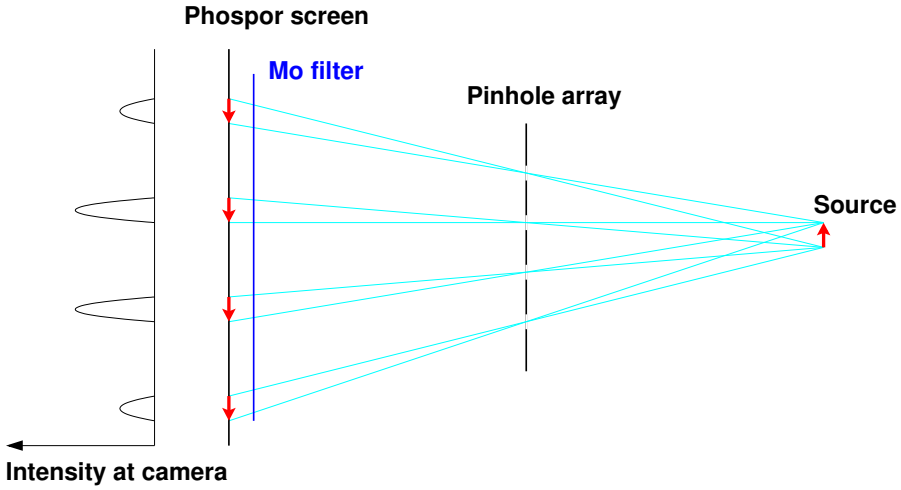

Figure A.1.: Geometry of the BESSY II pinhole monitor systems, including the pinhole array, the molybdenum filter and the phosphor screen.

For online analysis a *Labview* program is used, screen captures of the running program can be found in Fig. A.2. A region of interest (ROI) is set around an image of a single pinhole and a Gaussian fit applied to the horizontal and vertical projection of the ROI. The results for the rms beam size and the beam position are then monitored for both transverse dimensions.

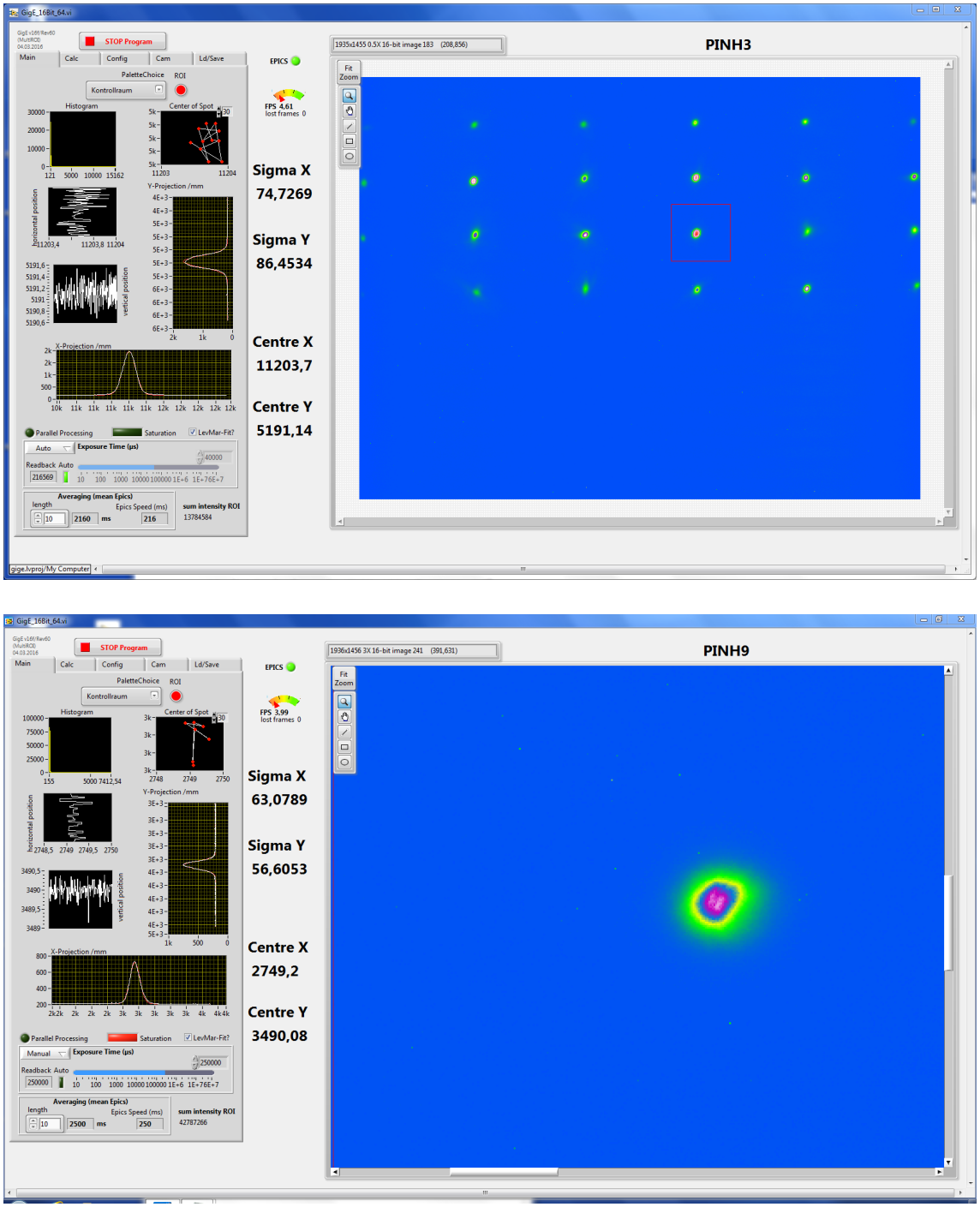

Figure A.2.: Screen captures from the *Labview* program for the pinhole systems, showing an image of the pinhole array from PINH9 (top) and zoomed in on a single pinhole at PINH3 (bottom). A Gaussian fit is applied to one pinhole inside the ROI (red).

B. Derivation of the Double Slit Interference Pattern

The objective of this appendix is the derivation of Eq. 3.31.Consider a simplified setup for only one transverse direction like in Fig. B.1. The radiation comes from a source in the reference system x and falls onto the double slit in x' at a distance L from the source. The interference pattern is then observed at the screen in x'', which is positioned at a distance f from the double slit.

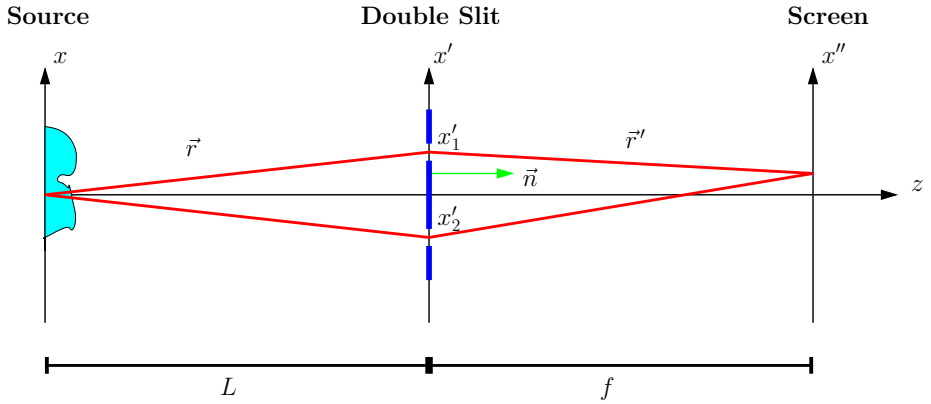

Figure B.1.: Sketch for derivation of double slit interference.

Assuming spherical waves like in Eq. 3.14 without the time depending term originating from a point source at $z = 0$, the complex amplitude of the sum amplitude at $\vec{r}$ is given by

$$E(\vec{r}) = \alpha(\vec{r})\frac{1}{r}e^{ikr}, \tag{B.1}$$

with the amplitude $\alpha(\vec{r})$, the wave vector $\vec{k}$, with $|\vec{k}| = \frac{2\pi}{\lambda}$, where λ is the wavelength, and $r = |\vec{r}|$. From Kirchhoff's diffraction theory [44, Chapter 8.3.2] one then gets the amplitude on the screen by integrating over the Aperture A:

$$E(S) = -\frac{i}{2\lambda}\int_A \frac{\alpha(\vec{r})}{rr'}e^{ik(r'+r)}\left[\cos(\vec{n},\vec{r}) - \cos(\vec{n},\vec{r}')\right]\mathrm{d}A, \tag{B.2}$$

with the normal $\vec{n}$ to the aperture.

Since the distances between the source, the double slit and the screen are large in comparison to the aperture the following approximations are made:

$$r \approx L \tag{B.3}$$

$$r' \approx f \tag{B.4}$$

$$\cos(\vec{n},\vec{r}) - \cos(\vec{n},\vec{r}') \approx -2. \tag{B.5}$$

In the term $e^{ikr'}$ the approximation of r' has to be done more carefully, because it varies in the order of the wavelength:

$$r' = \sqrt{f^2 + (x'' - x')^2} \tag{B.6}$$

$$\approx f + \frac{(x'' - x')^2}{2f} \tag{B.7}$$

$$\approx f - \frac{x'x''}{f}. \tag{B.8}$$

The approximation in Eq. B.7 is a Taylor expansion neglecting third and higher-order term and leads to the Fresnel diffraction. Neglecting also the second order term that do not depend on the sign of x' in Eq. B.8 leads to the Fraunhofer diffraction and the resulting approximation of Eq. B.2 is then:

$$E(x, x'') = \frac{e^{ikf}}{i\lambda L f} \int_A \mathrm{d}x' \alpha(\vec{r}) e^{ikr} e^{-i\frac{k}{f}x'x''}. \tag{B.9}$$

For a centered double slit with a full slit separation d and a full single slit width a the integral is:

$$E(x, x'') = \frac{e^{ikf}}{i\lambda L f} \left[\int_{\frac{d}{2}-\frac{a}{2}}^{\frac{d}{2}+\frac{a}{2}} \mathrm{d}x' \alpha(\vec{r}) e^{ikr} e^{-i\frac{k}{f}x'x''} + \int_{-\frac{d}{2}-\frac{a}{2}}^{-\frac{d}{2}+\frac{a}{2}} \mathrm{d}x' \alpha(\vec{r}) e^{ikr} e^{-i\frac{k}{f}x'x''} \right]. \tag{B.10}$$

Assuming the amplitude $\alpha(\vec{r})e^{ikr}$ does not change too much over a single slit and renaming it $\alpha_m(x)e^{ikr_m}$ with $m = 1, 2$ for the respective slits, the integral in Eq. B.10 can be solved:

$$E(x, x'') = \frac{e^{ikf}}{i\lambda L f} \left[\alpha_1(x) e^{ikr_1} \int_{\frac{d}{2}-\frac{a}{2}}^{\frac{d}{2}+\frac{a}{2}} \mathrm{d}x' e^{-i\frac{k}{f}x'x''} + \alpha_2(x) e^{ikr_2} \int_{-\frac{d}{2}-\frac{a}{2}}^{-\frac{d}{2}+\frac{a}{2}} \mathrm{d}x' e^{-i\frac{k}{f}x'x''} \right] \tag{B.11}$$

$$= \frac{e^{ikf}}{i\lambda L f} \left[\alpha_1(x) e^{ikr_1} \frac{if}{kx''} \left(e^{-o\frac{k}{f}x''\left(\frac{d}{2}+\frac{a}{2}\right)} - e^{-i\frac{k}{f}x''\left(\frac{d}{2}-\frac{a}{2}\right)} \right) \right.$$
$$\left. + \alpha_2(x) e^{ikr_2} \frac{if}{kx''} \left(e^{-i\frac{k}{f}x''\left(-\frac{d}{2}+\frac{a}{2}\right)} - e^{-i\frac{k}{f}x''\left(-\frac{d}{2}-\frac{a}{2}\right)} \right) \right] \tag{B.12}$$

$$= \frac{e^{ikf}}{i\lambda L f} \left[\alpha_1(x) e^{ikr_1} \frac{if}{kx''} e^{-i\frac{kd}{2f}x''} \left(e^{-i\frac{ka}{2f}x''} - e^{i\frac{ka}{2f}x''} \right) \right.$$
$$\left. + \alpha_2(x) e^{ikr_2} \frac{if}{kx''} e^{i\frac{kd}{2f}x''} \left(e^{-i\frac{ka}{2f}x''} - e^{i\frac{ka}{2f}x''} \right) \right] \tag{B.13}$$

$$= \frac{e^{ikf}}{i\lambda L f} \frac{if}{kx''} \sin\left(\frac{ka}{2f}x''\right) \left[\alpha_1(x) e^{ikr_1} e^{-i\frac{kd}{2f}x''} + \alpha_2(x) e^{ikr_2} e^{i\frac{kd}{2f}x''} \right] \tag{B.14}$$

$$= \frac{ae^{ikf}}{i\lambda L f} \mathrm{sinc}\left(\frac{ka}{2f}x''\right) \left[\alpha_1(x) e^{ikr_1} e^{-i\frac{kd}{2f}x''} + \alpha_2(x) e^{ikr_2} e^{i\frac{kd}{2f}x''} \right]. \tag{B.15}$$

To get the intensity at the screen the square of the absolute value of the amplitude has to be integrated:

$$I(x'') \propto \int |E(x,x'')|^2 \mathrm{d}x \tag{B.16}$$

$$\propto \mathrm{sinc}^2\left(\frac{ka}{2f}x''\right) \int \left|\alpha_1(x) e^{ikr_1} e^{-i\frac{kd}{2f}x''} + \alpha_2(x) e^{ikr_2} e^{i\frac{kd}{2f}x''}\right|^2 \mathrm{d}x \tag{B.17}$$

$$= \mathrm{sinc}^2\left(\frac{ka}{2f}x''\right) \int \mathrm{d}x \left[\alpha_1(x)\alpha_1^*(x) + \alpha_1(x)\alpha_2^*(x) e^{ik(r_1-r_2)} e^{-i\frac{kd}{f}x''} \right.$$

$$\left. + \alpha_2(x)\alpha_2^*(x) + \alpha_1^*(x)\alpha_2(x) e^{-ik(r_1-r_2)} e^{i\frac{kd}{f}x''}\right] \tag{B.18}$$

$$= \mathrm{sinc}^2\left(\frac{ka}{2f}x''\right) \left[\int I_1(x)\mathrm{d}x + e^{-i\frac{kd}{f}x''} \int I_{12}(x) e^{ik(r_1-r_2)}\mathrm{d}x \right.$$

$$\left. + \int I_2(x)\mathrm{d}x + e^{i\frac{kd}{f}x''} \int I_{21}(x) e^{-ik(r_1-r_2)}\mathrm{d}x\right]. \tag{B.19}$$

The step from Eq. B.18 to Eq. B.19 is similar as discussed for the van Cittert-Zernike theorem in Section 3.1 for the derivation of Eq. 3.18. The term $k(r_1 - r_2)$ can now approximated similarly to Eqs. B.6 to B.8:

$$r_1 - r_2 = \sqrt{\left(\frac{d}{2} - x\right)^2 + L^2} - \sqrt{\left(-\frac{d}{2} - x\right)^2 + L^2} \tag{B.20}$$

$$\approx L + \frac{1}{2L}\left(\frac{d}{2} - x\right)^2 - L - \frac{1}{2L}\left(-\frac{d}{2} - x\right)^2 \tag{B.21}$$

$$= \frac{1}{2L}\left(\frac{d}{2} - x\right)^2 - \frac{1}{2L}\left(\frac{d}{2} + x\right)^2 = -\frac{xd}{L}. \tag{B.22}$$

With the definition of

$$\int I_m(x)\mathrm{d}x = I_m \tag{B.23}$$

and the spatial frequency defined in Eq. 3.22 one gets:

$$I(x'') \propto \mathrm{sinc}^2\left(\frac{ka}{2f}x''\right) \left[I_1 + I_2 + e^{-i\frac{kd}{f}x''} \int I_{12}(x) e^{-i2\pi\nu_x x}\mathrm{d}x \right.$$

$$\left. + e^{i\frac{kd}{f}x''} \int I_{21}(x) e^{i2\pi\nu_x x)}\mathrm{d}x\right]. \tag{B.24}$$

After similar steps as in Eqs. 3.7, 3.8 and 3.11, Eqs. 3.19 and 3.20 respectively one gets:

$$I(x'') \propto (I_1 + I_2)\,\mathrm{sinc}^2\left(\frac{ka}{2f}x''\right)\left[1 + \frac{\sqrt{I_1 I_2}}{I_1 + I_2}e^{-i\frac{kd}{f}x''}\int f_{12}(x)e^{-i2\pi\nu_x x}\mathrm{d}x + \frac{\sqrt{I_1 I_2}}{I_1 + I_2}e^{i\frac{kd}{f}x''}\int f_{21}(x)e^{i2\pi\nu_x x)}\mathrm{d}x\right] \tag{B.25}$$

$$= (I_1 + I_2)\,\mathrm{sinc}^2\left(\frac{ka}{2f}x''\right)\left[1 + \frac{\sqrt{I_1 I_2}}{I_1 + I_2}\gamma_{12}e^{-i\frac{kd}{f}x''} + \frac{\sqrt{I_1 I_2}}{I_1 + I_2}\gamma_{21}e^{i\frac{kd}{f}x''}\right] \tag{B.26}$$

$$= (I_1 + I_2)\,\mathrm{sinc}^2\left(\frac{ka}{2f}x''\right)\left[1 + \frac{\sqrt{I_1 I_2}}{I_1 + I_2}|\gamma_{12}|e^{i\psi}e^{-i\frac{kd}{f}x''} + \frac{\sqrt{I_1 I_2}}{I_1 + I_2}|\gamma_{12}|e^{-i\psi}e^{i\frac{kd}{f}x''}\right] \tag{B.27}$$

$$= (I_1 + I_2)\,\mathrm{sinc}^2\left(\frac{ka}{2f}x''\right)\left[1 + \frac{\sqrt{I_1 I_2}}{I_1 + I_2}|\gamma_{12}|\left(e^{-i\frac{kd}{f}x''+\psi} + e^{i\frac{kd}{f}x''-\psi}\right)\right] \tag{B.28}$$

$$= (I_1 + I_2)\,\mathrm{sinc}^2\left(\frac{ka}{2f}x''\right)\left[1 + \frac{2\sqrt{I_1 I_2}}{I_1 + I_2}|\gamma_{12}|\cos\left(\frac{kd}{f}x'' - \psi\right)\right] \tag{B.29}$$

$$= (I_1 + I_2)\,\mathrm{sinc}^2\left(\frac{ka}{2f}x''\right)\left[1 + V\cos\left(\frac{kd}{f}x'' - \psi\right)\right]. \tag{B.30}$$

This derivation is made for spherical waves. The discussion for the modifications in case of synchrotron radiation are made in Section 3.2. Therefore actually the mean beam profile from the section of which synchrotron radiation is observed is measured and the incoherence depth of field effect described in Eq. 3.29 has to be considered for the horizontal case.

List of Figures

List of Tables

References

[1] F. R. Elder et al., "Radiation from Electrons in a Synchrotron", in: *Phys. Rev.* 71 (11 June 1947), pp. 829–830, DOI: 10.1103/PhysRev.71.829.5 (cit. on p. 1).

[2] E M Rowe and Frederick E Mills, "Tantalus I: A Dedicated Storage Ring Synchrotron Radiation source", in: *Part. Accel.* 4 (1973), pp. 211–227 (cit. on p. 1).

[3] A. Jankowiak et al., eds., "BESSY VSR – Technical Design Study", Helmholtz-Zentrum Berlin für Materialien und Energie GmbH, June 2015, DOI: 10.5442/R0001 (cit. on pp. 1, 3, 6–9).

[4] M Abo-Bakr et al., "Steady-state far-infrared coherent synchrotron radiation detected at BESSY II", in: *Phys. Rev. Lett.* 88.25 (2002), DOI: 10.1103/PhysRevLett.88.254801 (cit. on pp. 1, 5).

[5] Brian W. J. McNeil and Neil R. Thompson, "X-ray free-electron lasers", in: *Nature Photonics* 4.12 (Dec. 2010), pp. 814–821, DOI: 10.1038/nphoton.2010.239 (cit. on p. 1).

[6] Donald H. Bilderback et al., "Energy recovery linac (ERL) coherent hard x-ray sources", in: *New J. Phys.* 12 (2010), p. 035011, DOI: 10.1088/1367-2630/12/3/035011 (cit. on p. 1).

[7] Pedro F. Tavares et al., "The MAX IV storage ring project", in: *Journal of Synchrotron Radiation* (2014), pp. 862–877, DOI: 10.1107/S1600577514011503 (cit. on p. 1).

[8] M. Eriksson et al., "The MAX IV Synchrotron Light Source", in: *Proceedings of IPAC2011* (2011), THPC058, pp. 3026–3028 (cit. on p. 1).

[9] G. Wüstefeld et al., "Simultaneous long and short electron bunches in the BESSY II storage ring", in: *Proceedings of IPAC2011* (2011), THPC014, pp. 2936–2938 (cit. on pp. 1, 6).

[10] A. Jankowiak et al., "The BESSY VSR Project for Short X-Ray Pulse Production", in: *Proceedings of IPAC2016* (2016), WEPOW009, pp. 2833–2836, DOI: 10.18429/JACoW-IPAC2016-WEPOW009 (cit. on pp. 1, 6).

[11] K. Holldack, J. Feikes, and W.B. Peatman, "Source size and emittance monitoring on BESSY II", in: *Nuclear Instruments and Methods in Physics Research Section A: Accelerators, Spectrometers, Detectors and Associated Equipment* 467 - 468, Part 1 (2001), 7th Int.Conf. on Synchrotron Radiation Instrumentation, pp. 235–238, DOI: 10.1016/S0168-9002(01)00555-1 (cit. on pp. 1, 75).

[12] T. Mitsuhashi, "Beam profile and size measurement by SR interferometers", in: *Beam measurement. Proceedings, Joint US-CERN-Japan-Russia School on Particle Accelerators, Montreux and Geneva, Switzerland, May 11-20, 1998*, 1998, pp. 399–427 (cit. on pp. 2, 11, 13, 16, 18).

[13] M. Koopmans et al., “Status of a Double Slit Interferometer for Transverse Beam Size Measurements at BESSY II”, in: *Proceedings of IPAC2017* (2017), MOPAB032, pp. 149–152, DOI: 10.18429/JACoW-IPAC2017-MOPAB032 (cit. on p. 2).

[14] E. Jaeschke et al., “Lattice Design for the 1.7-GeV Light Source BESSY II”, in: *Proceedings of PAC1993* (1993), pp. 1474–1476 (cit. on p. 3).

[15] Martin Ruprecht, “Calculation of Coupled Bunch Effects in the Synchrotron Light Source BESSY VSR”, PhD thesis, Humboldt-Universität zu Berlin, 2016, DOI: 10.18452/17446 (cit. on p. 4).

[16] T. Atkinson et al., “Commissioning of the 50 MeV Preinjector Linac for the BESSY II Facility”, in: *Proceedings of IPAC2011* (2011), THPC108, pp. 3140–3142 (cit. on p. 3).

[17] T. Atkinson et al., “Status and Prospects of the BESSY II Injector System”, in: *Proceedings of IPAC2016* (2016), WEPOW007, pp. 2826–2828, DOI: 10.18429/JACoW-IPAC2016-WEPOW007 (cit. on p. 3).

[18] Felix Kramer, “Study and Optimization of the Transverse Beam Parameters before Injection into the Storage Ring BESSY II”, MA thesis, Humboldt-Universität zu Berlin, 2016 (cit. on p. 3).

[19] Daniel F. Förster et al., “Phase-locked MHz pulse selector for x-ray sources”, in: *Opt. Lett.* 40.10 (May 2015), pp. 2265–2268, DOI: 10.1364/OL.40.002265 (cit. on p. 4).

[20] K. Holldack et al., “Single bunch X-ray pulses on demand from a multi-bunch synchrotron radiation source”, in: *Nature communications* 5 (2014), pp. 2265–2268, DOI: 10.1038/ncomms5010 (cit. on pp. 5, 57).

[21] K. Holldack et al., “Characterization of laser-electron interaction at the BESSY II femtoslicing source”, in: *Phys. Rev. ST Accel. Beams* 8 (4 Apr. 2005), p. 040704, DOI: 10.1103/PhysRevSTAB.8.040704 (cit. on p. 5).

[22] Helmut Wiedemann, “Particle Accelerator Physics; 3rd ed.” Berlin: Springer, 2007, DOI: 10.1007/978-3-540-49045-6 (cit. on pp. 5, 14, 48, 53, 60).

[23] P.H van Cittert, “Die Wahrscheinliche Schwingungsverteilung in Einer von Einer Lichtquelle Direkt Oder Mittels Einer Linse Beleuchteten Ebene”, in: *Physica* 1.1 (1934), pp. 201–210, DOI: 10.1016/S0031-8914(34)90026-4 (cit. on p. 13).

[24] F. Zernike, “The concept of degree of coherence and its application to optical problems”, in: *Physica* 5.8 (1938), pp. 785–795, DOI: 10.1016/S0031-8914(38)80203-2 (cit. on p. 13).

[25] Mark Boland, Jeff Corbett, and Toshiyuki Mitsuhashi, “Measurement of the Incoherent Depth of Field Effect on Horizontal Beam Size Using a Synchrotron Light Interferometer”, in: *Proceedings of IPAC2015* (2015), TUPWA001, pp. 1391–1393 (cit. on pp. 16, 37).

[26] Thorlabs, Compact CCD Spectrometer, Item No. CCS200/M, 2016 (cit. on pp. 19, 20).

[27] Thorlabs, Cosine Correctors for CSS Spectrometers, Item No. CCSA2, 2016 (cit. on p. 19).

[28] Julian Schwinger, "On the Classical Radiation of Accelerated Electrons", in: *Phys. Rev.* 75 (12 June 1949), pp. 1912–1925, DOI: 10.1103/PhysRev.75.1912 (cit. on p. 20).

[29] Thorlabs, N-BK7 Plano-Convex Lens (Uncoated), Item No. LA1779, 2016 (cit. on pp. 25, 26).

[30] Mikhail N. Polyanskiy, "Refractive index database", https://refractiveindex.info, Accessed on 2017-11-07 (cit. on pp. 25, 26).

[31] Thorlabs, Linear Polarizer with N-BK7 Windows, 400-700 nm, Item No. LPVISE200-A, 2016 (cit. on p. 25).

[32] Edmund Optics, Hard Coated OD 4 Bandpass Filters, 2016 (cit. on p. 26).

[33] Allied Vision, Prosilica GT1920, 2016 (cit. on p. 27).

[34] Jeff Corbett et al., "Transverse Beam Profiling and Vertical Emittance Control with a Double-Slit Stellar Interferometer", in: *Proceedings of IBIC2016* (2017), MOPG70, pp. 237–240, DOI: 10.18429/JACoW-IBIC2016-MOPG70 (cit. on p. 62).

[35] G. Trad et al., "Beam Size Measurements Using Interferometry at LHC", in: *Proceedings of IBIC2016* (2017), WEBL02, pp. 584–589, DOI: 10.18429/JACoW-IBIC2016-WEBL02 (cit. on p. 66).

[36] T. Naito and T. Mitsuhashi, "Very small beam-size measurement by a reflective synchrotron radiation interferometer", in: *Phys. Rev. ST Accel. Beams* 9 (12 Dec. 2006), p. 122802, DOI: 10.1103/PhysRevSTAB.9.122802 (cit. on p. 70).

[37] S.T. Wang et al., "Visible-light beam size monitors using synchrotron radiation at CESR", in: *Nuclear Instruments and Methods in Physics Research Section A: Accelerators, Spectrometers, Detectors and Associated Equipment* 703 (2013), pp. 80–90, DOI: 10.1016/j.nima.2012.11.097 (cit. on p. 71).

[38] Kai Tang et al., "Transverse beam size measurement system using visible synchrotron radiation at HLS II", in: *Chin. Phys.* C40.9 (2016), p. 097002, DOI: 10.1088/1674-1137/40/9/097002 (cit. on p. 71).

[39] M.J. Boland et al., "Intensity Imbalance Optical Interferometer Beam Size Monitor", in: *Proceedings of IBIC2012* (2013), WECC03, pp. 566–570 (cit. on p. 71).

[40] J.-G. Hwang, "Bunch resolved beam size monitor for BESSY VSR", DEELS Workshop, 2017 (cit. on p. 72).

[41] Stanford Computer Optics, High speed ICCD framing camera family: XX-RapidFrame, 2017 (cit. on p. 72).

[42] K. Holldack and W.B. Peatman, "A Pinhole-Array X-Ray Electron Beam Monitor", tech. rep., Berlin, Germany: BESSY, 1996 (cit. on p. 75).

[43] W. B. Peatman and K. Holldack, "Diagnostic front end for BESSY II", in: *Journal of Synchrotron Radiation* 5.3 (1998), pp. 639–641, DOI: 10.1107/S0909049597017068 (cit. on p. 75).

[44] Max Born and Emil Wolf, "Principles of Optics", 4th ed., Oxford: Pergamon Press, 1970 (cit. on p. 77).

Statement of Authorship

I hereby declare that I have authored the present master thesis independently, and that I have not used any sources and means other than those specified.

Berlin, 30th November 2017

Marten Koopmans